1977

Surges in storm sewers.

Mostafa Ahmed. Hamam
University of Windsor

Recommended Citation

Hamam, Mostafa Ahmed., "Surges in storm sewers." (1977). *Electronic Theses and Dissertations.* Paper 3681.

National Library of Canada

Cataloguing Branch
Canadian Theses Division

Ottawa, Canada
K1A 0N4

NOTICE

The quality of this microfiche is heavily dependent upon the quality of the original thesis submitted for microfilming. Every effort has been made to ensure the highest quality of reproduction possible.

If pages are missing, contact the university which granted the degree.

Some pages may have indistinct print especially if the original pages were typed with a poor typewriter ribbon or if the university sent us a poor photocopy.

Previously copyrighted materials (journal articles, published tests, etc.) are not filmed.

Reproduction in full or in part of this film is governed by the Canadian Copyright Act, R.S.C. 1970, c. C-30. Please read the authorization forms which accompany this thesis.

THIS DISSERTATION
HAS BEEN MICROFILMED
EXACTLY AS RECEIVED

Bibliothèque nationale du Canada

Direction du catalogage
Division des thèses canadiennes

AVIS

La qualité de cette microfiche dépend grandement de la qualité de la thèse soumise au microfilmage. Nous avons tout fait pour assurer une qualité supérieure de reproduction.

S'il manque des pages, veuillez communiquer avec l'université qui a conféré le grade.

La qualité d'impression de certaines pages peut laisser à désirer, surtout si les pages originales ont été dactylographiées à l'aide d'un ruban usé ou si l'université nous a fait parvenir une photocopie de mauvaise qualité.

Les documents qui font déjà l'objet d'un droit d'auteur (articles de revue, examens publiés, etc.) ne sont pas microfilmés.

La reproduction, même partielle, de ce microfilm est soumise à la Loi canadienne sur le droit d'auteur, SRC 1970, c. C-30. Veuillez prendre connaissance des formules d'autorisation qui accompagnent cette thèse.

LA THÈSE A ÉTÉ
MICROFILMÉE TELLE QUE
NOUS L'AVONS REÇUE

NL-339 (3/77)

SURGES IN STORM SEWERS

by

Mostafa Ahmed Hamam
B. Sc. (Honour)

A Thesis
Submitted to the Faculty of Graduate Studies through
the Department of Civil Engineering in Partial
Fulfillment of the Requirements of the
Degree of Master of Applied Science
at the
University of Windsor

Windsor, Ontario, Canada
1977

To Amal and Marwa

ABSTRACT

This is a study of the hydrodynamics of rapidly unsteady flow in storm sewers.

The unsteady flow phenomena considered occurs in storm sewer systems with pumping. When a pump fails in a pumped-storm sewer system a surge is produced, which travels up the trunk sewer and into the sub-trunks and laterals, possibly causing basement flooding or other flood damage. This phenomenon depends on several factors, such as the flow at the failure, the capacity of the sump, the relative depth of water in the sewer and the slope of the sewer.

This study involves an experimental and theoretical study of the initiation and movement of these surges and the pressures produced in the system.

The movement of flood waves through a storm sewer model was studied experimentally. An overhead tank divided into two compartments was used to produce the inlet hydrographs for the model storm sewer system. Outlet hydrographs were measured using a pressure transducer and a laser anemometer. The results were analyzed to determine the effects of slope and effective storm duration on the hydrograph movement through the sewer.

The experimental work was carried out for three sewer slopes, i.e., subcritical, critical, and supercritical.

ACKNOWLEDGMENTS

The writer is greatly indebted to his advisor, Dr. J. A. McCorquodale, for his sincere, patient guidance throughout this study. His valuable suggestions and helpful comments are sincerely appreciated.

The writer wishes to express his thanks to Dr. J. K. Bewtra for his comments, continuous concern and encouragement.

The aid of Mr. P. Feimer and Mr. G. Michalczuk during the experimental work is highly appreciated.

To my wife, your sharing is grateful. Thank you very much.

The efforts of Doreen Truant in typing the manuscript are greatly appreciated.

Finally, the writer is grateful for the financial support provided by the Civil Engineering Department at the University of Windsor and the National Research Council of Canada through the operating grant of Dr. McCorquodale.

TABLE OF CONTENTS

LIST OF FIGURES

LIST OF PHOTOGRAPHS

LIST OF TABLES

CHAPTER I

INTRODUCTION

1.1 Objectives

The occurrence of surges and pressure waves in storm sewers due to power failure in the pumping stations has long been known. This research work was initiated to study the various controlling parameters when this phenomenon occurs. The effect of the air movement produced by the surges will be considered.

The experimental program includes the study of the inlet and the outlet hydrographs in the storm sewers for different storm durations and sewer slopes.

1.2 Outline of the Study

This research work concentrates on the occurrence of surges in storm sewers with pumping. An investigation is also made of the effect of bed slope on the outlet hydrograph with a known inlet hydrograph.

The equations of flow pertaining to this study are derived from the continuity and momentum principles.

The experimental work was carried out for three slopes, i.e. sub-critical, critical and super-critical slopes.

The inlet hydrographs were obtained by using an overhead tank divided into two compartments by filling up the smaller compartment and transfering the flow, using a flexible hose, into the large compartment for a certain period of time. The outlet hydrographs were obtained by measuring the velocities of the flow using a laser anemometer and the corresponding depths using a pressure transducer and strain indicator. The outlet hydrograph can be derived from the recording of the depths and the corresponding velocities with time on a two channel recorder.

Surge velocities were obtained by dividing the storm sewer length into three foot reaches and measuring surge front transit times using a stop watch. The flow pressures at the end of the storm sewer were measured by a piezometer tube and a pressure transducer.

To the best of the writer's knowledge, no attempt has been made to study the movement of surges in gravity storm sewer networks. The lack of literature on this phenomenon was in fact the essential motivation for the writer's work.

CHAPTER II

LITERATURE REVIEW

2.1 Rapidly Varied Unsteady Flow

2.1.1 Surges in Open Channel Flow

Chow (3) gave an equation for the surge velocity of rapidly varied uniformly progressive flow shown in Figure 2.1; the general form can be written as:

$$V_w = c \pm V_1 \tag{2.1}$$

where,

$$c = \left[\frac{(A_2 \bar{y}_2 - A_1 \bar{y}_1)\, g}{A_1 (1 - A_1/A_2)}\right]^{\frac{1}{2}} \tag{2.2}$$

V_w = surge velocity;

c = the velocity of the wave w.r.t. the velocity of the initial flow (celerity);

$\bar{y}_1$ = distance between the pressure center and the water surface at section 1;

$\bar{y}_2$ = distance between the pressure center and the water surface at section 2;

A_1 = area of flow at section 1;

A_2 = area of flow at section 2; and

V_1 = velocity of flow at section 1 (initial flow).

Figure 2.2 shows four types of rapidly varied uniformly progressive flows. Equations 2.1 and 2.2 can be used to describe a moving hydraulic jump. In Figure 2.2, the initial and the final stages of a passing surge are assumed to be uniform. Such surges occur frequently in channels of small slope. In inclined channels, four types of surges can occur as shown in Figure 2.3.

Positive Surges are described by

$$V_1 - V_2 = \pm \frac{h}{c} \left(\frac{y_1 + y_2}{2y_1}\right) g \qquad (2.3)$$

where,

y_1 and y_2 = flow depths at sections 1 and 2 respectively;

V_1 and V_2 = flow velocities at sections 1 and 2 respectively;

and h = surge height.

When the height of surge is small compared with the depth of flow ($y_1 \approx y_2$), Equation 2.3 may be written

$$V_1 - V_2 = \pm \frac{h\ g}{c} \qquad (2.4)$$

Chow presents several cases of positive surges such as:

(1) surge due to sudden stoppage of flow,

(2) meeting of two surges, and

(3) surge crossing a step.

For Negative Surges of moderate or small height compared with the depth of flow, the equations derived for a positive surge can be applied to approximate the propagation of the negative surge. Analysis of a negative surge with a relatively large height is also given.

Chow presented a brief study of the following:

(1) surge in power canals,

(2) surge in navigation canals,

(3) surge through channel transitions,

(4) surge at channel junctions, and

(5) pulsating flow.

In 1969, Terzidis and Strelkoff (14) found the solution for the supercritical flow resulting from the sudden introduction of a subsequently constant discharge into a rectangular, horizontal, frictionless channel. They used the simple explicit diffusing scheme, shown in Figure 2.4, to solve the following equations:

$$y_k^{j+1} = \frac{1}{2}\left(y_{k-1}^j + y_{k+1}^j\right) + \frac{\lambda}{2}\left(q_{k-1}^j - q_{k+1}^j\right) \tag{2.5}$$

$$q_k^{j+1} = \frac{1}{2}\left(q_{k-1}^j + q_{k+1}^j\right) + \frac{\lambda}{2}\left[\left(\frac{q^2}{y} + \frac{g}{2}y^2\right)_{k-1}^j - \right.$$

$$\left. - \left(\frac{q^2}{y} + \frac{g}{2}y^2\right)_{k+1}^j\right] + \frac{\Delta t}{2}\,\text{[illegible]}_{1} + \phi_{k+1}^j) \tag{2.6}$$

in which,

$$\phi = gy\left(S_o - S_f\right) \tag{2.7}$$

$$\lambda = \frac{\Delta t}{\Delta x} < \frac{1}{\left|\frac{q}{y} \pm \sqrt{gy}\right|} \tag{2.8}$$

$$\Delta t < \frac{2}{\left|\frac{\partial \phi}{\partial q}\right|} \tag{2.9}$$

where,

q = discharge per unit width of the channel,

y = flow depth,

Δt = time increment, and

Δx = length increment. Equations 2.8 and 2.9 must be satisfied at every section at every time. The results of their calculations are shown in Figure 2.5.

They also used Equations 2.5 and 2.6 to solve the unsteady subcritical flow with friction in a horizontal rectangular channel and compared the results of calculations and experiment. Calculated depths of flow were in very satisfactory agreement with experiment.

2.2 Surges in Closed Conduits with Full Pipe Flow

Streeter and Wylie (11) presented a description of the water hammer phenomenon and methods of computations. For example the method of characteristics is recommended for general use in computer solutions. They discussed the different means of surge and water hammer control such as using surge tanks on the long pipelines, or supplying a quick-opening bypass valve.

The water hammer in sewage force mains due to power failure in the sewage pumping station is discussed by Metcalf and Eddy Inc. (8). The velocity of the pressure wave is given by

$$a = \frac{4,720}{1 + (Kd/Ee)} \tag{2.10}$$

where,

a = velocity of pressure wave, fps,

d = pipe diameter, in.,

e = pipe-wall thickness, in.,

E = modulus of elasticity of pipe material, psi, and

K = bulk modulus of water, taken as 300,000 psi.

They state that the values of "a" normally lie in the range from 3500 to 4100 fps, for different types of sewage pipes. Swing check valves with outside lever and weight set to assist closure; are recommended for small and medium-size pumps. Spring loaded check valves may also be used. In large pumping stations, check valves should be positively controlled using cone valves or butterfly valves.

2.3 The Effect of Air on the Surge Movement

Wallis (16) gave the following equation for the motion of the dynamic waves in incompressible two-component flow in a constant area duct

$$U = V_o \pm c \tag{2.11}$$

where,

$$c = \pm \left(\frac{-(v_1 - v_2)^2}{y_1/\rho_2 H + (1 - y_1/H)/\rho_1} - f_{\nabla\alpha}\right)^{\frac{1}{2}} \left(\frac{\rho_1}{1 - y_1/H} + \frac{\rho_2 H}{y_1}\right)^{-\frac{1}{2}} \tag{2.12}$$

$$V_o = \frac{v_1\rho_1/(1 - y_1/H) + v_2\rho_2 H/y_1}{\rho_1/(1 - y_1/H) + \rho_2 H/y_1} \tag{2.13}$$

where,

v_1, v_2 = velocities of components 1 and 2 respectively;

ρ_1, ρ_2 = densities of components 1 and 2 respectively;

y_1/H = volumetric fraction of component 2;

U = wave velocity, and

c = velocity of dynamic wave relative to weighted average velocity.

f represents the net force on the flow produced by a concentration gradient, the subscript $\nabla\alpha$ is equal to $\partial\alpha/\partial Z$. V_o is defined as the weighted mean velocity. Figure 2.6 shows schematic representation for the case of a dynamic wave propagation in two incompressible stratified components in a horizontal duct, in this case;

$$f_{\nabla\alpha} = -(\rho_2 - \rho_1)\, g\, H \tag{2.14}$$

H = the height of the duct.

Then Equation 2.12 becomes:

$$c = \pm \left[\frac{-(v_1 - v_2)^2}{y_1/\rho_2 H + (1 - y_1/H)/\rho_1} + (\rho_2 - \rho_1)\, gH\right]^{\frac{1}{2}} \left(\frac{\rho_1}{1 - y_1/H} + \frac{\rho_2\, H}{y_1}\right)^{-\frac{1}{2}} \tag{2.15}$$

The relative velocity is seen to have a destabilizing effect because it decreases the dynamic wave velocity. For sufficiently high relative velocity, c^2 becomes negative and the flow is unstable. This occurs when:

$$(v_1 - v_2)^2 > (\rho_2 - \rho_1)\, gH \left(\frac{y_1}{\rho_2 H} + \frac{1 - y_1/H}{\rho_1}\right) \tag{2.16}$$

When compressibility effects are important, the propagation of dynamic waves is governed by the gradients of three "concentrations" (the densities of the two components and the volumetric concentration of one of them). In this case compressibility waves moves with velocities:

$$U = V \pm C_{cs} \tag{2.17}$$

where,

$$C_{cs} = \pm \left(\frac{y_1/\rho_1 H + (1 - y_1/H)/\rho_1}{y_1/H\ \rho_2\ c_2^2 + (1 - y_1/H)/\rho_1\ c_1^2}\right)^{\frac{1}{2}} \tag{2.18}$$

assuming that there is no relative velocity.

where c_1^2 and c_2^2 are the velocities of compressibility waves in each component separately. The velocity C_{cs} is the velocity of a compressibility wave in a homogeneous mixture. For truly homogeneous flow there must be sufficient friction between the components to prevent relative motion. If ρ_2 is much less than ρ_1 and c_2^2 is less than c_1^2 then: the compressibility wave velocity in a strictly homogeneous mixture would be:

$$C_{ch} = \left(\frac{c_2^2\ \rho_2}{(\rho_1 y_1/H).(1 - y_1/H)}\right)^{\frac{1}{2}} \tag{2.19}$$

$$(C_{ch})_{min.} = 2\ c_2\ \left(\frac{\rho_2}{\rho_1}\right)^{\frac{1}{2}} \tag{2.20}$$

For air and water at atmospheric pressure, for example

$c_2 = 1100$ fps, $\frac{\rho_2}{\rho_1} = 0.0012$, $(C_{ch})_{min.}$ is then equal to 75 fps.

Streeter and Wylie (12), explained the effects on waterhammer of entrained air in the pipeline. They stated that the existence of gas bubbles can greatly reduce the velocity of the pressure wave in a pipeline. They defined a bulk modulus of elasticity for the mixture (liquid and gas) as:

$$K = \frac{K_{liq}}{1 + (\forall_g/\forall)[(K_{liq}/K_g)-1]} \qquad (2.21)$$

where,

$\forall$ = total volume of the fluid;

$\forall_{liq}$ = volume of the liquid;

$\forall_g$ = volume of the gas;

K_{liq} = bulk modulus of elasticity for the liquid; and

K_g = bulk modulus of elasticity for the gas.

They expressed the mixture density as:

$$\rho = \rho_g \frac{\forall_g}{\forall} + \rho_{liq}(\frac{\forall_{liq}}{\forall}) \qquad (2.22)$$

where,

ρ_g = density of the gas, and

ρ_{liq} = density of the liquid.

If the amount of gas in the pipeline is small, then the effect of pipe-wall elasticity will be insignificant and the wave speed can be obtained from the following equation:

$$a = \sqrt{\frac{K}{\rho}} \qquad (2.23)$$

where K and ρ can be obtained from Equations 2.21 and 2.22. A very good agreement was observed between their theory and experimental results.

In 1972, Metcalf and Eddy, Inc. (8) discussed the importance of ventilation and air relief. They mentioned that the ventilation of sewers is important to prevent the accumulation of sewer gases that may be explosive or corrosive and to prevent the creation of pressures above or below atmospheric. Some of the factors causing the movement of air in sewers are explained, theoretically and practically. The best locations for ventilation openings are stated. Different methods for ventilation and air relief are given in detail.

2.4 Gradually Varied Unsteady Flow

In 1959, Chow (3) gave the continuity equation for unsteady flow in open channels in the following forms:

$$\frac{\partial Q}{\partial x} + T\frac{\partial y}{\partial t} = 0 \tag{2.24}$$

$$\frac{\partial Q}{\partial x} + \frac{\partial A}{\partial t} = 0 \tag{2.25}$$

$$\frac{\partial (VA)}{\partial x} + T\frac{\partial y}{\partial t} = 0 \tag{2.26}$$

$$A\frac{\partial V}{\partial x} + V\frac{\partial A}{\partial x} + T\frac{\partial y}{\partial t} = 0 \tag{2.27}$$

$$D\frac{\partial V}{\partial x} + V\frac{\partial y}{\partial x} + \frac{\partial y}{\partial t} = 0 \tag{2.28}$$

The general dynamic equation for gradually varied unsteady flow is given by Equation 2.29.

$$\frac{\partial y}{\partial x} + \frac{\alpha V}{g}\frac{\partial V}{\partial x} + \frac{1}{g}\frac{\partial V}{\partial t} + \frac{\partial Z}{\partial x} + S_f = 0 \qquad (2.29)$$

For prismatic channels, i.e. for $-\partial Z/\partial x = S_o$, Equation 2.29 may be written

$$\frac{\partial y}{\partial x} + \frac{\alpha V}{g}\frac{\partial V}{\partial x} + \frac{1}{g}\frac{\partial V}{\partial t} = S_o - S_f \qquad (2.30)$$

The velocity of the monoclinal rising wave is given by

$$V_w = \frac{Q_1 - Q_2}{A_1 - A_2} \qquad (2.31)$$

The dynamic equation for uniformly progressive flow in a prismatic channel is given by Equations 2.32 and 2.33.

$$\frac{\partial y}{\partial x} = \frac{S_o - (V_w A - Q_o)^2/K^2}{1 - Q_o^2/g\ A^2\ D} \qquad (2.32)$$

$$\frac{dy}{dx} = \frac{S_o - Q^2/K^2}{1 - (V_w A - Q)^2/g\ A^2\ D} \qquad (2.33)$$

If the velocity is very low, Equation 2.33 becomes:

$$\frac{dy}{dx} = S_o - \frac{Q^2}{K^2} \qquad (2.34)$$

Hence

$$Q = Q_n \sqrt{1 - \frac{1}{S_o}\frac{dy}{dx}} \qquad (2.35)$$

or

$$Q = Q_n \sqrt{1 + \frac{j}{V_w S_o}} \qquad (2.36)$$

where $j = -V_w \frac{dy}{dx}$

Thomas (15) gave the solution of the unsteady-flow equations using the method of finite increments (see Figure 2.7 for notations) as follows:

$$V_4 = \frac{\Delta x \Sigma T (y_1 - y_2 + y_3 - y_4)/4\Delta t + A_1 V_1 + A_2 V_2 - A_3 V_3}{A_4} \qquad (2.37)$$

$$S_o = \frac{(\Sigma V)^2}{4C^2 \Sigma R} - \frac{y_1 + y_2 - y_3 - y_4}{2\ \Delta\ x} - \frac{\alpha \Sigma V (V_1 + V_2 - V_3 - V_4)}{8\ g\ \Delta\ x}$$

$$- \frac{V_1 - V_2 + V_3 - V_4}{2\ g\ \Delta\ t} \qquad (2.38)$$

In practice, the quantities y_1, A_1, V_1, y_2, A_2, V_2, y_3, A_3 and V_3 are known from the initial conditions and from the computations on previous reaches. The unknown quantities y_4 and V_4 can be obtained by solving Equations 2.37 and 2.38 simultaneously. Repeating the computation for subsequent reaches, the complete profile and velocity variation of the flow can be determined.

In 1956, Isaacson, Stoker and Troesch (7) outlined a numberical method of solving unsteady flow problems in rivers. The basic equations governing the flow in a river are:

$$B\ H_t + (AV)_x = q \qquad (2.39)$$

$$V_t + VV_x + g\ H_x = -G\ V|V| - \frac{q}{A}\ V \qquad (2.40)$$

They used the method of finite differences to solve Equations 2.39 and 2.40. The solution yields to Equations 2.41 and 2.42.

$$V_p = \frac{1}{2}\ [V_R + V_L] - \frac{\Delta t}{2\Delta x}\ \{\frac{V_R^2 - V_L^2}{2} + g\ (H_R - H_L)\} -$$

$$- \frac{\Delta t}{2}\ [G_R\ V_R^2 + G_L\ V_L^2] - \frac{\Delta t}{2}\ [\frac{V_R}{A_R} + \frac{V_L}{A_L}]\ q_{RL} \qquad (2.41)$$

$$H_p = \frac{1}{2}\ [H_R + H_L] - \frac{\Delta t}{(B_R + B_L)\Delta x}]\ [A_R\ V_R - A_L\ V_L] +$$

$$+ 2\Delta t\ [\frac{q_{RL}}{B_R + B_L}] \qquad (2.42)$$

where L, R and P are shown on x-t plane in Figure 2.8.

In order to compute values of stage or discharge for net points at boundaries, it is necessary to have a known boundary condition, such as stage or discharge or a relation between stage and discharge (e.g. Rating Curve).

For a boundary point on the upstream side, use the given boundary condition together with Equations 2.43 and 2.44 to determine H_N and V_N in terms of already known quantities.

$$B_L\ [\frac{H_K - H_L}{\Delta t}] + \frac{A_R\ V_R - A_L\ V_L}{2\Delta x} - q_{RL} - \sqrt{\frac{B_L\ A_L}{g}}$$

$$[\frac{V_K - V_L}{\Delta t} + \frac{V_R^2 - V_L^2}{4\Delta x} + g\ (\frac{H_R - H_L}{2\Delta x}) + \frac{q_{RL}\ V_L}{A_L}$$

$$+ G_L\ V_L^2] = 0 \qquad (2.43)$$

$$B_K\ [\frac{H_N - H_K}{\Delta t}] + \frac{A_p\ V_p - A_K\ V_K}{\Delta x} - q_{KP} - \sqrt{\frac{B_K\ A_K}{g}}\ \times$$

$$\times \left[\frac{V_N - V_K}{\Delta t} + \frac{V_P^2 - V_K^2}{2\Delta x} + g.\left(\frac{H_P - H_K}{\Delta x}\right) + \frac{q_{KP}\ V_K}{A_K}\right.$$

$$\left. + G_K\ V_K^2\right] = 0 \qquad (2.44)$$

where L, R, K, P and N are shown on x-t plane in Figure 2.9. At the downstream end a similar pair of equations is set up, i.e..

$$B_R\left[\frac{H_K - H_R}{\Delta t}\right] + \frac{A_R\ V_R - A_L\ V_L}{2\Delta x} - q_{LR} + \sqrt{\frac{B_R\ A_R}{g}}$$

$$\left[\frac{V_K - V_R}{\Delta t} + \frac{V_R^2 - V_L^2}{4\Delta x} + g\left(\frac{H_R - H_L}{2\Delta x}\right) + \frac{q_{LR}\ V_R}{A_R}\right.$$

$$\left. + G_R\ V_R^2\right] = 0 \qquad (2.45)$$

$$B_K\left[\frac{H_N - H_K}{\Delta t}\right] + \frac{A_K\ V_K - A_P\ V_P}{\Delta x} - q_{PK} + \sqrt{\frac{B_K\ A_K}{g}}$$

$$\left[\frac{V_N - V_K}{\Delta t} + \frac{V_K^2 - V_P^2}{2\Delta\ x} + g\left(\frac{H_K - H_P}{\Delta x}\right) + \frac{q_{PK}\ V_K}{A_K}\right.$$

$$\left. + G_K\ V_K^2\right] = 0 \qquad (2.46)$$

where L, R, K, P and N are shown on x-t plane in Figure 2.10.

In 1963, Morgali (9), presented a study of a method for synthesizing overland and channel flow hydrographs for small drainage areas. A mathematical model is substituted for the actual flow situation. Considering an element of fluid of length dx taken from a channel with lateral inflow, as shown in Figure 2.11, he derived the continuity equation

$$\frac{\partial(AV)}{\partial x} + B\,\frac{\partial y}{\partial t} = q \qquad (2.47)$$

A similar element is used in the derivation for the momentum equation (see Figure 2.12); the derived equation is similar to Equation 2.30. In the solution of the flow equations he uses the method of characteristics to define the limits of the increments of Δx and Δt in the x-t plane. A numerical solution of the equations of flow, using the finite difference method is given.

Considering a portion of the x-t plane shown in Figure 2.14, the $\frac{\partial V}{\partial x}$ at station M can be approximated in finite difference terms as

$$\left.\frac{\partial V}{\partial x}\right)_M = \frac{V_R - V_L}{2\Delta x}$$

Similarly

$$\left.\frac{\partial y}{\partial x}\right)_M = \frac{y_P - y_L}{2\Delta x}$$

$$\left.\frac{\partial V}{\partial t}\right)_P = \frac{V_P - V_M}{\Delta t}$$

$$\left.\frac{\partial y}{\partial t}\right)_P = \frac{y_P - y_M}{\Delta t}$$

Substituting these values for the partial differentials in the equation of continuity (Equation 2.47) and solving for y_P (considering a unit width of the channel) results in

$$y_P = y_M + \Delta t\ \left[\frac{y_L\,V_L - y_R V_R}{2\Delta x} + q_{LR}\right] \qquad (2.48)$$

If the values for velocity and depth are known at time = t_o, the only value in Equation 2.48 which is unknown is y_p. This allows one to step forward to a new time $(t_o + \Delta t)$ for the flow depth at the given station. Using the friction slope

$$S_f = \frac{V^2\ n^2}{2.2082\ R^{4/3}} \tag{2.49}$$

and the finite differentials in Equation 2.30 gives

$$\begin{aligned} V_P = & -\frac{2.2082}{2\Delta t n^2 g}\, y_P^{4/3} + [\frac{2.2082}{\Delta t n^2 g}\, y_P^{4/3}\ \{\frac{2.2082}{4\Delta t n^2 g}\, y_P^{4/3} \\ & + V_M[1.0 + \frac{\Delta t}{2\Delta x}\,(V_L - V_R)] + g\Delta t\, S_o \\ & + \frac{g\Delta t}{2\Delta x}\,(y_L - y_R)\}]^{\frac{1}{2}} \end{aligned} \tag{2.50}$$

If all values are known at time, t_o, the only unknown in this equation at time, $(t_o + \Delta t)$, are V_P and y_P. Equation 2.48 has only y_p as an unknown. If Equation 2.48 for y_p is solved first, then the only unknown in Equation 2.50 is V_p and it is possible to step forward an increment in time, Δt, at this station in both velocity and depth of flow. The same procedures are repeated for the subsequent stations and for the next time increments. As a necessary initial condition for the solution, all depths and velocities along the channel network, x, at a given time, t_o, must be known (see Figure 2.13). The required equations for the depth and velocity of flow at the upstream and the downstream boundaries of the channel and at junctions, should be given. Investigation of the hydrograph of overland flow and the effects of parameters, e.g. channel roughness, channel slope, rainfall excess, and size of time and distance increments for overland flow are given. A detailed study of natural channel flow is presented. Figure 2.15 is a typical example of an observed and synthesized hydrograph. Favorable results are obtained in comparisons for two small watersheds.

In 1966, Blatzer and Lai (2), presented three methods for accurately and economically simulating unsteady flows in rivers and estuaries. The theoretical analysis of the flow and the development of computer-oriented simulation techniques are mainly based on the use of continuity equation, and equation of motion. They studied the effect of wind and the channels with overflow portions on the equation of motion. Three computer oriented methods for simulating transient flows in open channels are explained in detail, i.e.,

(1) Power Series Method,

(2) The Method of Characteristics,

(3) An Implicit Method.

Each of these methods is designed for high-speed, digital computer execution. Comparisons of the simulated flows obtained by using each of these methods with numerous field-measured, transient flows indicated generally good agreement. Figure 2.16 is a typical example comparing the computed and the measured discharges.

In 1968, Mozaneny and Song (10) solved the equation of continuity and the equation of motion in the form of four characteristics Equations 2.51, 2.52, 2.53 and 2.54 by using a finite-difference scheme.

$$dt + \zeta_{(\pm)}\, dx = 0 \qquad (2.51)$$

$$-g\,dy + [(V^2 - \frac{gA}{B})\,\zeta_{(\pm)} - V]\,dV + H\,(V\,\zeta_{(\pm)} - 1)\,dx = 0 \qquad (2.52)$$

in which $H = V\frac{Q}{A} - g\,S + \frac{g\,n^2\,v^2}{(1.486)^2 R^{4/3}}$ (2.53)

$$y(o,t) = y_o + \frac{Y}{2}\,[1 - \cos(\frac{2\pi t}{T})],\ T \geq t \geq 0 \qquad (2.54)$$

$$y(o,t) = y_o,\ t \geq T$$

where $\zeta_{(\pm)} = \frac{1}{V \pm \sqrt{\frac{gA}{B}}}$

Figure 2.17 shows a part of the grid system in the x-t plane used in calculations. Using the program written for the purpose of this study, they routed a single sine flood wave of 30 sec. initial duration in a rectangular channel of unit width, the depth of the base flow was taken to be 0.3 ft. A CDC6600 digital computer was used. Figures 2.18 and 2.19 show typical stage and discharge hydrographs. The effect of amplitude on the dimensionless rating curves is shown in Figure 2.20 where

$$y^*(x,t) = \frac{y(x,t) - y_o}{Y} \qquad (2.55)$$

$$Q^*(x,t) = \frac{Q(x,t) - Q_o}{Q_{sm} - Q_o} \qquad (2.56)$$

y* and Q* are dimensionless depth and discharge respectively. They also found the effect of both channel slope and Manning's n on R* as shown in Figures 2.21 and 2.22.

where;

$$R^* = C_1 \, S^{-0.552} \qquad (2.57)$$

$$C_1 = 0.0076 + 3.15n - 22.6n^2 \qquad (2.58)$$

In 1968, Harris (5) presented a paper dealing with a special problem of routing in real time a flood hydrograph down a single circular channel with critical flow at the downstream end. A simple routing method (the progressive average lag routing method) which gives similar results to the method of characteristics with considerably less computer time is presented in detail. This simple method will be useful in the case of complicated series of sewers which require routing of hydrographs in real time. It is necessary to obtain the routing constants by comparing the results of the two methods (the method of characteristics and the progressive average-lag method), for one hydrograph; the same routing constants hold for other hydrographs starting at the same base flow.

In 1969, Strelkoff (13) presented a numerical solution of Saint-Venant Equations. The differential equations of continuity and motion for one dimensional gradually varied, unsteady channel flow are

$$A\frac{\partial V}{\partial x} + VT\frac{\partial y}{\partial x} + T\frac{\partial y}{\partial t} + VA\frac{y}{x} + q = 0 \qquad (2.59)$$

$$\frac{1}{g}\frac{\partial V}{\partial t} + \frac{V}{g}\frac{\partial V}{\partial x} + \frac{\partial y}{\partial x} = S_o - S_f + D_\ell \qquad (2.60)$$

in which

$$S_f = \frac{V|V|}{C^2 R} = \frac{Q|Q|}{K^2} \qquad (2.61)$$

and

$$D_\ell = 0 \text{ (bulk lateral outflow)} \qquad (2.62a)$$

$$D_\ell = \frac{Vq}{2Ag} \text{ (seepage outflow)} \qquad (2.62b)$$

$$D_\ell = \frac{V - u_\ell}{Ag}\, q \text{ (lateral inflow)} \qquad (2.62c)$$

The theoretical basis for the method of characteristics is reviewed and used to solve the previous equations. Finite-difference schemes on a rectangular net in the x-t plane, based on the characteristic forms of the Saint-Venant equations as well as on the direct forms are given and examined for their stability. The von Neumann technique for stability analysis is presented in detail.

Explicit numerical schemes which require small steps in time are contrasted with implicit schemes that permit numerical solution over large time steps but require the solution of large sets of simultaneous algebric equations at each step. The double-sweep or "progonka" method, an exact time-and-space-saving technique for solving these equations is also given in detail.

In 1972, Dorsch Consult of West Germany (4), presented a report dealing with the mathematical modelling of urban hydrologic processes. Conventional methods of storm sewer design are criticized. A package of mathematical models of the hydrologic and hydraulic phenomena, designed to correct the major deficiencies of the conventional analysis is introduced. It is called the Hydrograph-Volume-Method (H-V-M). The theoretical development and practical application of H-V-M are also shown. A computer simulation of storm and combined sewer networks is presented. The new directions for research and development in this field, made available by computer technology, are discussed.

The foundations of the computer simulation of sewer networks are:

(1) Rainfall evaluation,
(2) Surface runoff computation,
(3) Routing the flow in the sewer network.

The hydraulic calculations are performed using the general (St. Venant) partial differential equations of continuity and energy. The continuity equation for surface runoff is written

$$\frac{\partial y}{\partial t} = r(t) - i(t) - \frac{\partial Q}{\partial A_s} \qquad (2.63)$$

or, in difference form

$$\Delta V = \Delta y \cdot A_s = r \cdot \Delta t \cdot A_s - i \cdot \Delta t \cdot A_s - Q_E \cdot \Delta t \qquad (2.64)$$

The runoff "q" is found from the energy equation which is simplified to the Manning's equation

$$q = \frac{K\, y^{5/3}\, j^{1/2}}{L} \qquad (2.65)$$

Both equations are solved iteratively. Figure 2.23 shows the different notations used in the previous equations.

A typical test result is shown in Figure 2.24. It is important to know that the hydrograph for runoff from any such tributary area is constructed from super-imposed hydrographs of the three surface types (asphalt, concrete, and garden plants) based on the relative portions of such surfaces.

The runoff hydrographs obtained simulate runoff to the sewer inlets and serve as input data to the sewer network calculation program of H-V-M. The foundations of this computer model are the two general partial differential equations describing an unsteady, non-uniform, frictional flow regime. Figure 2.25 shows a comparison between their computed hydrograph and the measurements obtained in 1960 in Chicago, Illinois for the Interior Department.

CHAPTER III

THEORY

The intent in this chapter is to derive the basic equations which will be used in subsequent chapters for analysis of positive surges in storm sewers.

3.1 Derivation of the Equations of Motion

3.1.1 The Equations of Motion Neglecting the Air Effect

The Continuity Equation

Imagine that an observer beside the storm sewer model is running after the positive surge of Figure 3.1, in the same direction and at the same velocity V_w as the surge front. He will see a picture of a steady flow like that in Figure 3.2, i.e., the water surface will appear stationary to him, and the flow will show a steady discharge Q_o and a velocity V_w-V at every point along the storm sewer model. Hence;

$$Q_o = (V_1 + V_w)\ A_1 = (V_2 + V_w)\ A_2 \tag{3.1}$$

or

$$V_w = \frac{V_1A_1 - V_2A_2}{A_2 - A_1} \tag{3.2}$$

where,

V_1 = velocity of flow at Section 1;

V_2 = velocity of flow at Section 2;

A_1 = area of flow at Section 1;

A_2 = area of flow at Section 2, and

V_w = surge velocity.

The inflow discharge, Q_i is

$$Q_i = V_1 A_1 \tag{3.3}$$

The Momentum Equation

The hydrostatic pressures on the areas A_1 and A_2 at sections 1 and 2 respectively, are

$$F_1 = \gamma A_1 \bar{y}_1 \tag{3.4}$$

$$F_2 = \gamma \int_{Z}^{Z+H} y\,dA = \gamma A_2 (\bar{y}_2 + Z) \tag{3.5}$$

where,

$\bar{y}_1$ = distance of the centroid of the flow area A_1 below the sewer crown;

$\bar{y}_2$ = distance of the centroid of the flow area A_2 below the sewer crown;

Z = end piezometric head, above the sewer crown;

H = depth of the conduit, and

γ = specific weight of the water.

Using Newton's second law of motion, the unbalanced force required to change the momentum per unit time is the product of the mass and the change in velocity per unit time, or

$$F = \frac{\gamma}{g} (V_w + V_2) A_2 (V_2 - V_1) \tag{3.6}$$

The unbalanced force, F, is equal to the difference between the hydrostatic forces at Sections 1 and 2 or

$$F = F_1 - F_2 \tag{3.7}$$

Substituting from Equations 3.4, 3.5, and 3.6, in Equation 3.7

$$\frac{\gamma}{g} (V_w + V_2) A_2 (V_2 - V_1) = \gamma A_1 \bar{y}_1 - \gamma A_2 (\bar{y}_2 + Z) \tag{3.8}$$

Solving Equation 3.8 for V_w

$$V_w = \frac{g}{A_2 (V_2 - V_1)} [A_1 \bar{y}_1 - A_2 \bar{y}_2 - A_2 Z] - V_2 \tag{3.9}$$

Equating the values of V_w in Equations 3.2 and 3.9

$$\frac{V_1 A_1 - V_2 A_2}{A_2 - A_1} = \frac{g}{A_2 (V_2 - V_1)} [A_1 \bar{y}_1 - A_2 \bar{y}_2 - A_2 Z] - V_2 \tag{3.10}$$

Solving Equation 3.10 for Z

$$Z = \frac{A_1}{A_2} \bar{y}_1 - \bar{y}_2 + \frac{(V_1 - V_2)}{g} [\frac{V_1 A_1 - V_2 A_2}{A_2 - A_1} + V_2] \tag{3.11}$$

Equation 3.11 represents the general equation for the downstream piezometric head.

Equations 3.2 and 3.9 represent the general equations of motion for a positive surge shown in Figure 3.1. Value of V_1 can be found by using Manning's equation if the discharge "Q", the bed slope "S_o", and Manning "n" are known.

The value of V_2 depends on the downstream blockage conditions. For a given value of V_2, the downstream piezometric head can be found using Equation 3.11.

For rectangular cross section pipe, with sudden closure of the downstream end:

$A_1 = By_1;$

$A_2 = By_2;$

$\bar{y}_1 = \frac{1}{2} y_1;$

$\bar{y}_2 = \frac{1}{2} y_2 = \frac{1}{2} H;$

$V_2 = 0;$

and Equation 3.11 after simplifying gives

$$Z = \frac{V_1^2 \, y_1}{g(H - y_1)} + \frac{y_1^2}{2H} - \frac{1}{2} H \qquad (3.12)$$

Equation 3.12 can be written in dimensionless form as

$$\frac{Z}{y_1} = \frac{F_1^2}{(\frac{1}{\Theta} - 1)} + \frac{\Theta}{2} - \frac{1}{2\Theta} \qquad (3.13)$$

where,

$F_1 = \frac{V_1}{\sqrt{g \, y_1}}$ = Froude number;

$\Theta = \frac{y_1}{H}$ dimensionless parameter.

3.1.2 Equations of Motion Considering the Air Effect

If the air pressure inside the storm sewer model is equal to p, see Figure 3.1, then the resulting force, P, due to this pressure can be given by the following equation:

$$P = p \, A_2 \qquad (3.14)$$

Then Equation 3.7 becomes

$$F = F_1 + P - F_2 \tag{3.15}$$

Substituting from Equations 3.4, 3.5, 3.6 and 3.14 into Equation 3.15 and simplifying

$$V_w = \frac{g}{A_2(V_2 - V_1)} [A_1\bar{y}_1 + \frac{p}{\gamma} A_2 - A_2\bar{y}_2 - A_2 Z] - V_2 \tag{3.16}$$

Equating the values of V_w in Equations 3.2 and 3.16 and solving for Z

$$Z = \frac{A_1}{A_2} \bar{y}_1 - \bar{y}_2 + (\frac{V_1 - V_2}{g}) (\frac{V_1A_1 - V_2A_2}{A_2 - A_1} + V_2) + h_p \tag{3.17}$$

where,

$h_p = \frac{p}{\gamma}$ = pressure drop in length L

For complete downstream closure of a rectangular cross-section pipe, Equation 3.17 becomes

$$Z = \frac{V_1^2 \; y_1}{g(H - y_1)} + \frac{y_1^2}{2H} - \frac{H}{2} + h_p \tag{3.18}$$

Equation 3.18 can be written in dimensionless form as

$$\frac{Z}{y_1} = \frac{F_1^2}{(\frac{1}{\Theta}-1)} + \frac{\Theta}{2} - \frac{1}{2\Theta} + \frac{h_p}{y_1} \tag{3.19}$$

Equations 3.2 and 3.16 represent the general equations of motion of the positive surge forming in the storm sewer model shown in Figure 3.1, considering the air effect.

The value of h_p can be computed as follows:

$$h_p = \frac{p}{\gamma} = \frac{\gamma_{air}}{\gamma_{water}} (K_{exit} \cdot \frac{V^2}{2g} + \frac{fL}{D} \frac{V^2}{2g}) \qquad (3.20)$$

Since $D = 4R_h$ Equation 3.20 becomes

$$h_p = \frac{\gamma_{air}}{\gamma_{water}} (\frac{V^2}{2g}) (K_{exit} + \frac{fL}{4R_h}) \qquad (3.21)$$

where,

L = length of pipe;

R_h = hydraulic radius = $\frac{hB}{2h + 2B}$;

$h = H - y_1$;

v = air velocity = surge velocity (V_w);

f = friction factor = $0.316\ R_e^{-0.25}$, and

$R_e = \frac{VR_h}{\nu}$.

The exit coefficient, K_{exit}, in the last equation can be found from the following equation:

$$K_{exit} = \frac{1.0}{0.6} (\frac{A_{op}}{A_{orf}})^2 \qquad (3.22)$$

where,

A_{op} = $(H - y_1) \times B$; and

A_{orf} = area of ventilation orifices at the upstream end of the storm sewer model.

3.2 Flow Regimes

According to Baker's analysis (1), see Figure 3.3: "Flow-regime correlations for adiabatic horizontal two-phase two-component flow." The limits between the stratified and the wavy flow regimes can be determined for the storm sewer model, for a range of slope between 0.001 and 0.008, which includes the subcritical, the critical, and the supercritical slope of the experimental work. The pipe was assumed to be horizontal for Baker's analysis.

The ranges of stratified and wavy flow regimes in the storm sewer model are shown in Figure 3.4, a similar result is obtained for a prototype concrete section of 10:1 scale (see Figure 3.5).

3.3 Fluid Motion After the Bubble Formation

Applying Newton's second law of motion on the water mass inside the pipe (see Figure 3.6 for notations) just after the formation of the bubble, the unbalanced force required to change the momentum per unit time is the product of the mass and the change in velocity per unit time (acceleration), or

$$F = ma \tag{3.23}$$

$$-A\ [(p_i - p_{at}) + \gamma h] - h_f\ \gamma A = A\ \frac{\ell'}{g}\ \gamma\ \frac{d^2S}{dt^2} \tag{3.24}$$

where,

A = area of flow;

P_{at} = atmospheric pressure;

p_i = pressure of air inside the bubble during the compression of the bubble;

ℓ' = distance of the bubble from the upstream end of the pipe;

h = height of the bubble;

h_f = pressure drop due to the friction, and

S = distance measured in the bed direction.

Substituting with:

$$h_f = \frac{f\ell'}{8gR_h} \left(\frac{ds}{dt}\right) \left|\frac{dS}{dt}\right| ;$$

$$h = S\left(\frac{A}{A_b}\right), \text{ and}$$

$$p_i = p_o \frac{\forall_o}{\forall_i} = \frac{p_o}{1 - S\frac{A}{\forall_o}} \quad \text{(assuming isothermal conditions);}$$

in Equation 3.24 and simplifying

$$\frac{d^2S}{dt^2} + \frac{f}{8R_h} \left(\frac{dS}{dt}\right) \left|\frac{ds}{dt}\right| + \frac{Ag}{A_b\ell'} S - \frac{p_{at}g}{\gamma\ell'} + \frac{p_og}{\gamma\ell'} \frac{1}{1 - \frac{A}{\forall_o} S} = 0 \qquad (3.25)$$

where,

$\forall_o$ = volume of trapped air when the bubble formed;

p_o = initial absolute air pressure when the bubble formed;

$\forall_i$ = volume of bubble during the compression, and

A_b = contact area between the bubble and the water.

Neglecting the friction, Equation 3.25 can be written

$$\frac{d^2S}{dt^2} + B_1 S + B_2 + \frac{B_3}{1 - B_4 S} = 0 \qquad (3.26)$$

where,

$$B_1 = \frac{gA}{A_b \ell'} \quad ;$$

$$B_2 = \frac{-p_{at} g}{\gamma \ell'} \quad ;$$

$$B_3 = \frac{p_o g}{\gamma \ell'} \quad , \text{ and}$$

$$B_4 = \frac{A}{\forall_o} \; .$$

Equation 3.26 can be approximated to

$$\frac{d^2 S}{dt^2} + B_1 S + B_2 + B_3 (1 + B_4 S) = 0 \tag{3.27}$$

or

$$\frac{d^2 S}{dt^2} + \overline{C}_1 S + \overline{C}_2 = 0 \tag{3.28}$$

where,

$\overline{C}_1 = B_1 + B_3 B_4$, and

$\overline{C}_2 = B_2 + B_3$.

Assume $u = \overline{C}_1 S + \overline{C}_2$, then Equation 3.28 becomes

$$\frac{d^2 u}{dt^2} + \overline{C}_1 u = 0 \tag{3.29}$$

The solution of Equation 3.29 is

$$u = D_1 \cos at + D_2 \sin at \tag{3.30}$$

where $a = \sqrt{\overline{C}_1}$

at $t = 0$

$$\frac{ds}{dt} = V_o \text{ and } S = S_o$$

$$\therefore D_1 = \bar{C}_1 S_o + \bar{C}_2, \text{ and}$$

$$D_2 = \sqrt{\bar{C}_1}\ V_o$$

Substituting the values of u, D_1 and D_2 in Equation 3.30

$$S = (S_o + \frac{\bar{C}_2}{\bar{C}_1}) \cos \sqrt{\bar{C}_1}\ t + \frac{V_o}{\sqrt{\bar{C}_1}} \sin \sqrt{\bar{C}_1}\ t - \frac{\bar{C}_2}{\bar{C}_1} \qquad (3.31)$$

Equation 3.31 represents the general solution for the flow movement after bubble formations with the time. Variation in piezometric pressure is given by

$$\Delta Z = \frac{p_i - p_{at}}{\gamma} = \frac{p_o}{\gamma(1 - S\frac{A}{\forall_o})} - \frac{p_{at}}{\gamma} \qquad (3.32)$$

In the previous analysis, it was assumed that the bed slope (S_o) was negligibly small. If the bed slope is significant, the downstream piezometric head (Z), Equations 3.11, 3.12, 3.13, 3.17, 3.18, and 3.19, will be increased by the amount (ℓS_o), where ℓ is the travelled length of the surge.

CHAPTER IV

EXPERIMENTAL STUDY

4.1 Introduction

In this chapter the following subjects will be described:

A. The Test Equipment, including the model and the laboratory facilities.

B. The Measurement Equipment, including a laser anemometer, a video recorder, a flow meter, a pressure transducer, a strain indicator, and a piezometric tube.

C. Experimental Procedures containing:

(i) The experimental determination of Manning's coefficient, n, for the plexiglass material used to construct the conduit.

(ii) Slope adjustment of the pipe.

(iii) Preparation of measurement equipment for experimental tests.

(iv) Calibration of the measurement equipment.

(v) Dye velocity measurement through the pipe for different discharges.

(vi) Measurement of surge characteristics (surge velocity and piezometric pressure).

(vii) Measurement of the effect of ventilation on the downstream piezometric pressures.

(viii) Switching of the discharge between the overhead tank compartments and its effect on the flow meter readings.

(ix) Closing the downstream end of the pipe for surge generation.

(x) The experimental reproduction of the inlet hydrographs.

(xi) The measurement of the outlet hydrographs.

D. Experimental Results.

4.2 The Test Equipment

The general layout of the experimental equipment is illustrated in Figure 4.1.

The Model

The model (Figures 4.2 and 4.3) was a 43 ft. (13.1 m.) plexiglass pipe with a square cross-section, 5.50 in. by 5.50 in. (14.00 cm. x 14.00 cm.) internal dimensions, connected at the upstream end to a vertical steel inflow chamber provided with four screens of 9 mm. square openings placed as shown in Figure 4.2. Two ventilation vents of 16 mm. diameter are provided at the upstream end of the pipe, at 4 cm. and 96 cm. from the steel inflow chamber. The upstream end of the pipe connected to the steel inflow chamber is shown in Photo 4.1.

The pipe is connected at the downstream end to a steel end tank, at 1.50 ft. (0.46 m.) above the tank bottom (see Photos 4.2 and 4.3). The end tank is 2 ft. (0.61 m.)

wide, 3 ft. (0.91 m.) long, and 4 ft. (1.22 m.) high. A vertical opening of 18 in. (46.cm.) high by 2.50 in. (6.4 cm.) wide with a movable gate is placed as shown in Figure 4.3, leading to a vertical steel outflow pipe leading to the laboratory sump. The vertical outflow pipe has a square cross-section of 5 in. by 5 in. (12.7 cm. x 12.7 cm.).

A steel overhead tank (shown in Figure 4.2 and Photo 4.1) is 4 ft. (1.22 m.) long, 4 ft. (1.22 m.) wide and 2.50 ft. (0.76 m.) high. The tank is divided into two compartments as shown; the small one is 4 ft. (1.22 m.) long and 1.50 ft (0.46 m.) wide and is provided with an overflow pipe of 3 in. (7.6 cm.) diameter at 2 ft. (0.61 m.) from the bottom. A 2 in. (5.1 cm.) diameter opening is placed at the bottom for the outflow discharge. The large compartment is 4 ft. (1.22 m.) long, 2.50 ft. (0.76 m.) wide and 2.50 ft. (0.76 m.) high and is provided with a square opening, 5 in. by 5 in. (12.7 cm. by 12.7 cm.) at the bottom for the outflow. A common chamber of 2.58 ft. (0.79 m.) long and a square cross-section of 7 in. by 7 in. (18 cm. by 18 cm.) is placed to collect the outflow from the two compartments. This chamber is provided with a vertical pipe having a square cross-section of 5 in. by 5 in. (12.7 cm. by 12.7 cm.) leading to the inflow chamber illustrated in Figure 4.2 and Photo 4.1. The flow is delivered by a centrifugal pump to the overhead tank by means of a 4 in. (10.2 cm.) diameter pipe line, ending with a flexible hose of the same size.

The end of the plexiglass pipe can be closed manually using a movable wooden arm (shown in Figure 4.4) connected with a wooden plate covered by 1/8 in. (3.2 mm.) rubber gasket to prevent leakage at the closure.

Photo 4.1 shows the upstream end of the storm sewer model, the pipe carrying the flow from the pump to the overhead tank, and the overhead tank with the overflow pipe. Photo 4.4 shows the plexiglass pipe. Photo 4.5 shows the downstream end of the model and the centrifugal pump. Photo 4.6 shows the downstream end of the storm sewer model (looking downstream).

The plexiglass pipe was constructed of 6 equal sections of 6.17 ft. (1.88 m.) long, and a shorter section of 5.83 ft. (1.78 m.) long. The sections were joined together with slightly flexible joints using 1/8 in. (3.2 mm.) rubber gaskets shown in Figure 4.5. A wooden structure was built to carry the plexiglass pipe and the steel tanks. The end tank was supported with a platform as illustrated in Figure 4.6. The upstream overhead tank was supported by another platform shown in Figure 4.7. The plexiglass pipe rested on the flange of a 47.50 ft. (14.47 m.) long continuous T-section beam. The details of the continuous T-section beam with the required splices are given in Figure 4.8. The beam is supported at points A, B, C, D, E, F, G, and H (see Figure 4.9); the details of these supports are given in Figure 4.10.

A stand was built (see Figure 4.11), adjacent to the end tank, for the manual closing of the pipe end.

Laboratory Facilities

A centrifugal pump, having maximum and minimum speeds of 1450 R.P.M. and 1100 R.P.M. respectively, a maximum head of 22 ft. (6.71 m.) and a maximum discharge of 3500 U.S.G.P.M. (0.2267 m^3/s) was used. Water is delivered to the overhead tank by means of a 4 in. (10.2 cm.) diameter pipe line.

A magnetic flowmeter calibrated in U.S.G.P.M. was used for flow measurement. The flowmeter reads the steady discharge entering the overhead tank, with 50 U.S.G.P.M. (0.00315 m^3/s) divisions and a possible error of 15 U.S.G.P.M. (0.000945 m^3/s).

4.3 Measurement Equipment

A. A (TSI) laser anemometer (see Photos 4.3, 4.7, and 4.8) was used to measure the flow velocity at the downstream end of the storm sewer model.

The laser anemometer was composed of three main parts:

(i) A spectra physics exciter (model 256), to produce a red Helium-Neon laser beam with wave length of 632.8 x 10^{-9} m.

(ii) A laser doppler velocimeter (LDV) optics (system 900) and 14.32° beam focusing lens.

(iii) A laser doppler anemometer signal processor (model 1090) with 3 selectable ranges; from 2 KHz to 50 MHz, for velocity changes of 200:1.

B. A (Data Sensors, Inc.) strain gage type pressure transducers with digital strain indicators, model P-350 (see

Photo 4.7) were used to measure the flow depths at the downstream end of the storm sewer model.

C. A two channel (Hewlett-Packard) strip chart recorder, model 7100B, was used to record the depths and velocities of flow versus the time for the hydrograph calculations (see Photo 4.7).

D. A piezometric tube (Photo 4.3), was used to measure the end piezometric pressure, Z, at closure of the downstream end of the storm sewer model.

E. A Sony video recording system was used to record the surge movement for subcritical, critical, and supercritical slopes.

4.4 Experimental Procedures

4.4.1 Experimental Determination of Manning's "n"

Different flow rates (Q) corresponding to different flow depths (Y), covering the whole range of (Y) for the pipe, and for a specified slope (S) were recorded.

The flow rate (Q) was measured by means of a magnetic flow meter. The flow depth (Y) was read on side scales with 2 mm. divisions placed at intervals of 3 ft. (0.91 m.) along the pipe. The depth of flow (Y) was taken as the average reading along the downstream 18 ft. (5.49 m.) reach of the pipe, neglecting the reading at the downstream end of the pipe, i.e., the critical depth section.

4.4.2 Slope Adjustment of the Pipe

The following steps were followed to adjust the pipe slope:

(i) The pipe was placed first on the flange of the continuous T-section beam which is nearly horizontal.

(ii) The pipe was divided into 3 ft. (0.91 m.) reaches, starting from the downstream end, and at the limits of each reach 2 mm. division scales were fixed at a side of the pipe.

(iii) The level of the downstream tank was adjusted by means of 4 screws supported on 4 steel plates (Figure 4.12), resting on the wooden platform designed to carry the tank.

(iv) The closing arm shown in Figure 4.4 was used to close the downstream end of the pipe, and the pipe was partially filled with water to produce an accurate horizontal reference plane for the slope adjustment.

(v) The slope of the first downstream section of the pipe was adjusted with the help of the mechanism illustrated in Figure 4.13, which was fixed just on the upstream side of the first joint of the pipe. For a certain slope, the difference between the bottom levels at the ends of the first section was calculated, and the upstream end of this section was elevated to have the exact slope by subtracting the depth of water at the upstream end from that at the downstream end, and comparing that difference with that desired. Then the first joint was shimmed to this level.

(vi) This procedure was repeated with the rest of the sections, and the difference between the bottom levels of the pipe at the end tank and the end of each section was checked, to obtain the most accurate measurement of the slope for the whole pipe.

(vii) The same procedures were repeated to change the slope for each series of tests.

4.4.3 Preparation of the Measurement Equipment

The pump was started for a few minutes to stabilize the flow meter, and then the flow was stopped to determine the zero reading, which may be different from that reading before starting the pump. The zero reading was subtracted from the subsequent flow meter readings to get the proper discharges.

The laser anemometer was adjusted to give the best signal for the velocity at point II (see Figure 4.14). The measurement point II was photographed during one of the tests (see Photo 4.8). The laser anemometer was connected to one channel of the two channel recorder, and the pump was operated to have a full pipe flow with approximately the maximum possible velocity at the measurement point, then a suitable range was selected according to the available space on the recording chart paper.

Two strain indicators, denoted (A) and (B), each connected with a pressure transducer, were used to measure the flow depth (Y), (see Figure 4.14). The strain indicator (A) connected to the transducer placed at point I, was adjusted to have a zero reading when there was no flow in the pipe, i.e. the strain indicator (A) was measuring the atmospheric pressure. The strain indicator (B) connected to another transducer, used to measure the atmospheric pressure, was adjusted also to have a zero reading (at the atmospheric pressure). The two strain indicators (A) and (B) were connected to the electronic subtraction unit which is connected to the recorder (see Figure 4.14). The subtractor gives the pressure of water at point I compared to the atmospheric pressure, i.e. the difference of reading between (A) and (B). The suitable range for the depth recording was chosen at full pipe flow (maximum possible depth).

4.4.4 Calibration of the Measurement Equipment

Flow Meter

The magnetic flow meter used in the experimental work was calibrated for two slopes (critical and supercritical slopes). Red dye was injected in the upstream portion of the pipe and the dye velocity was measured for different depths and flow meter readings. The discharge was computed from the following equation:

$$Q = B\ Y\ V_d \tag{4.1}$$

where,

B = width of the pipe;

Y = measured average depth along the downstream 18 ft. of the pipe; the depths were recorded at 3 ft. intervals along this distance using the side scales; V_d = measured dye velocity, as the average of three measurements, within the downstream 18 ft. of the pipe.

Figure 4.15 shows the calculated discharges using equation 4.1, against the flow meter readings for the critical slope of 0.0033 used in the experimental study.

The laser velocity at point II (see Figure 4.14) was recorded for different flow meter readings, and then corrected to obtain the average velocity through the section, using the curve given in Figure 4.16. The flow depth was recorded by means of two transducers along with two strain indicators following the procedures outlined in article 4.4.3. Then the discharge was calculated using the following equation:

$$Q = B\ Y_t\ V_\ell \qquad (4.2)$$

where,

B = pipe width;

Y_t = flow depth measured as mentioned above;

V_ℓ = average velocity over the pipe flow section

using the corrected laser anemometer reading. Figure 4.17 shows the discharges calculated from Equation 4.2, versus the flow meter discharges, for the supercritical slope of 0.0061, used in the experimentation.

Figures 4.15 and 4.17 show a very good agreement among the discharges obtained by dye and laser measurements and the magnetic flowmeter discharges.

Pressure Transducers and Strain Indicators

The flow depth at point I (see Figure 4.14) was measured following the procedures explained in article 4.4.3, for different discharges and a recording range of 0.5 volts. The readings from the subtraction unit (in volts) were plotted for various flow depths in Figure 4.18. This represents the calibration curve of the difference in readings between the two strain indicators (pressure difference) used to record the flow depth.

Laser Anemometer

The flow velocity at point II was measured by the laser anemometer (see Figure 4.14), and recorded for different discharges. Figure 4.19 shows a straight line relationship between the laser anemometer voltages and the corresponding velocities.

4.4.5 Dye Velocity Measurement

The velocity of flow through the pipe was measured using a red dye, following the procedures explained in Article 4.4.4, to check the flow meter readings and Manning's velocities.

4.4.6 Measurement of Surge Characteristics

A. Surge Velocity (V_w)

The pipe was divided into 3 ft. (0.91 m.) reaches, which were marked with small wood stands placed on the top of the pipe at the edge of the measuring side.

The end of the pipe was closed suddenly and the surge velocity, V_w, was obtained by using a stop watch to measure the transit time of the surges, over three different lengths (18 ft., 15 ft., and 12 ft.) from the end tank.

The surge velocity, V_w, was considered as the average value of three velocities of three surges at each discharge along the three lengths mentioned above.

B. Downstream Piezometric Head (Z)

The piezometric head (Z) at the downstream end of the pipe, caused by sudden pipe closure was measured by a piezometer tube placed at the end of the pipe, as shown in Photo 4.3.

4.4.7 Determination of the Effect of Ventilation on the Downstream Piezometric Head (Z)

Two air vents each of 16 mm. diameter were provided at the upstream end of the pipe at 4 cm. and 96 cm. from the steel inflow chamber (see Figure 4.2). The effect of these two vents on the piezometric head (Z) at the downstream end of the pipe was measured for three different discharges with 76 mm., 83 mm., and 102 mm. initial flow depths.

4.4.8 Manual Switching of the Flow Between the Two Compartments of the Overhead Tank

In order to synthesize the inlet hydrographs the small compartment of the overhead tank was filled and then the pump flow was suddenly switched to the large compartment for a certain duration, after which the delivery valve on the pump was rapidly closed.

The flow was switched manually during the hydrograph tests. The galvanized pipe carrying the flow from the pump to the overhead tank had a flexible hose that could feed either the large compartment or the small compartment. During switching the hose was handled manually and slightly buckled thus causing a contraction and a temporary decrease in the rate of flow. The flow rate increased when the switching to the large compartment was completed. Figure 4.20 shows the discharges before and after switching the flow to the large compartment of the overhead tank.

4.4.9 Closing the Downstream End of the Pipe

The end pipe was closed manually using the gate attached to the wooden arm as shown in detail in Figure 4.4; this produced a surge travelling upstream in the pipe. This case represents the pump failure in the storm sewer network. The gate closure mechanics are illustrated in Figure 4.21.

A significant leakage was noticed at higher discharges if the gate closure was imperfect. The test was repeated if imperfect closure was observed.

4.4.10 Experimental Synthesizing of the Inlet Hydrographs

The pump was started to fill the small compartment of the overhead tank (see Figure 4.2) at a steady discharge, and as soon as this compartment was full the flow was suddenly transferred to the large compartment for a certain duration to produce the rising part of the hydrograph; at the end of that duration the flow was suddenly stopped to yield the recession part of the hydrograph. Different durations of inflow to the large compartment were used to represent inlet hydrographs of different storm durations. Hydrographs were developed for the three slopes (subcritical, critical, and supercritical) used in the experimental study. The restricted flow from the small compartment represented the baseflow portion of the hydrograph.

Routing the Inlet Hydrograph

Discharge-stage curves were developed (see Figure 4.22) for both the small and the large compartments of the overhead tank. Discharge was read by the magnetic flow meter, and stage was read by piezometer tubes placed at the sides of the two compartments. These curves will be used in Chapter V to route the pump discharge through the tank storage to obtain the inlet hydrograph for the pipe.

4.4.11 Measurement of the Outlet Hydrographs

An outlet hydrograph was produced at the downstream end of the pipe from the synthesized inlet hydrograph explained in Article 4.4.10.

The flow depth was measured at point I as explained in Article 4.4.3. The flow velocity at point II (see Figure 4.14) was measured using the laser anemometer; the depth and the velocity of flow during the hydrograph tests were recorded against the time by means of the two channel recorder shown in Photo 4.7.

4.5 Experimental Results

4.5.1 Critical Slope Results

A 0.0033 critical bed slope, determined as explained in Appendix A, was used in the following tests:

A. Surge Characteristics

The experimental surge velocities (V_w) with both air vents open are plotted for different discharges in Figure 4.23.

The measured surge heights (h) for free surges for various discharges are given in Figure 4.24.

The experimental piezometric heads (Z) relative to the sewer crown at the outfall end of the sewer are illustrated in Figure 4.25, for different discharges.

B. Hydrographs

Figure 4.26 shows a sample of the recorded data tracings required to draw the outlet hydrograph. The average velocity through the section can be obtained from the recorded velocity at point II and the correction curve given in Figure 4.16. The discharges during the hydrograph test can be calculated from the experimental results using the following equation:

$$Q_t = B\ Y_t\ C\ (V_\ell)_t \tag{4.3}$$

where,

Q_t = discharge at time (t);

Y_t = depth of flow at time (t);

$(V_\ell)_t$ = velocity measured by laser anemometer at time (t).

C = velocity correction factor given in Figure 4.16.

The resulting discharges from the previous equation were plotted against the corresponding times to get the outlet hydrograph.

The experimentally synthesized inlet hydrographs and the measured outlet hydrographs are demonstrated in Figures 4.27, 4.28, and 4.29 for different storm durations; 20 sec., 30 sec., and 60 sec. respectively. The derivation of these curves will be considered in more detail in Chapter V.

C. Effect of Ventilation Vents

Figures 4.30 and 4.31 show the effect of the ventilation vents for three chosen discharges.

D. Dye Velocity Measurement

The dye velocity was measured as explained in Article 4.4.4, for different discharges (see Figures 4.15 and 4.32).

4.5.2 Subcritical Slope Results

A 0.00109 subcritical bed slope, chosen as explained in Appendix A, was used to obtain the experimental results. The flow in this case was observed to be gradually varied.

A. Gradually Varied Flow Profiles

Figure 4.33 shows the experimental results for the flow profiles along the pipe for different discharges. Figure 4.34 shows the flow profiles for different discharges when a 2.54 cm. high sill was installed at the downstream end of the pipe.

B. Surge Characteristics

The experimental surge velocities (V_w) with both air vents open are plotted for different discharges in Figure 4.35. The surge velocity (V_w) was measured for different discharges when the end sill was used; the form of the surge front is also recorded (see Figure 4.36).

The experimental downstream end piezometric heads (Z) with both air vents open are illustrated in Figure 4.37 for different discharges.

C. Hydrographs

The synthesized inlet hydrograph and the measured outlet hydrograph are plotted in Figures 4.38, 4.39, and 4.40 for storm durations of 20 sec., 30 sec., and 60 sec. respectively.

4.5.3 Supercritical Slope Results

A 0.0061 supercritical bed slope, chosen as explained in Appendix A, was used for the following tests.

The discharges calculated by Manning's equation for this slope were checked experimentally by means of a laser anemometer to measure the flow velocity and two pressure transducers to measure the flow depth following the procedures explained in Article 4.4.3. The results are given in Figure 4.41.

A. Surge Characteristics

The experimental surge velocity (V_w) with both air vents open for different discharges are given in Figure 4.42.

The downstream piezometric heads (Z) measured experimentally with both air vents open for different discharges are shown in Figure 4.43.

B. Hydrographs

The synthesized inlet hydrographs and the measured outlet hydrographs are plotted in Figures 4.44, 4.45, and

4.46 for storm durations of 22 sec., 30 sec., and 65 sec. respectively.

C. Dye Velocity Measurement

The dye velocity was measured as explained in Article 4.4.4, for different discharges (see Figure 4.47).

Water Temperature

The average observed water temperature during the experimental work was 70°F (21.1°C).

CHAPTER V

ANALYSIS AND DISCUSSION OF RESULTS

This chapter compares the experimental surge characteristics (surge velocity, V_w, height of surge, h, and the downstream piezometric head, Z) with the corresponding theoretical values. Also the inlet hydrographs are compared with the outlet hydrographs for different storm durations. The effects of bed slope on the outlet hydrographs and the surge characteristics are discussed. The effects of ventilation and trapped air on the downstream piezometric head are also considered. The chapter analyzes the experimental data for the determination of Manning's "n", and the dye velocity measurements, which are used in the surge analysis and the estimation of errors.

Experimental errors are discussed in relation to the comparisons of the theoretical and experimental results.

Finally a discussion on the surge characteristics and hydrograph measurements is presented.

5.1 Experimental Manning's "n"

According to Manning's formula, n was computed as follows:

$$n = \sum \left(\frac{1.49}{Q} By \left(\frac{By}{B + 2y}\right)^{2/3} \sqrt{S_o}\right) / N \qquad (5.1)$$

where,

N = the number of readings.

The measurements of the flow rate (Q) and the flow depth (y) for a specific slope (S_o) used in Equation.5.1 are explained in Article 4.4.1.

For the critical slope ($S_o = 0.0033$) used in the experimental work, Equation 5.1 gave a Manning's "n" of 0.0078 for the plexiglass material used to construct the conduit. Using Manning's velocity (n = 0.0078), kinematic viscosity (ν) of 1.059×10^{-5} ft^2/sec. at the average temperature of 70^{o}F recorded during the experimental work, and the above critical slope, the Froude number (F_r) will vary between 0.817 and 1.036, and Reynolds' number (R) will vary between 3×10^3 and 1.35×10^5 for a corresponding range of flow depth between 10 mm and 140 mm (full pipe flow).

A Manning's "n" of 0.0078 was obtained also, using Equation 5.1, for the supercritical slope ($S_o = 0.0061$) used in the experimentation. The Froude number (F_r) for this case, varied from 1.100 to 1.358, and Reynolds' number (R) varied from 4.4×10^3 to 1.8×10^5.

It was noticed that the subcritical slope (S_o = 0.00109) used in the experimental study gives a gradually varied flow through the pipe. It was found by trial, that the values, $\alpha = 1.2$ and $n = 0.0086$ gave the best fitting for predicted discharges compared with the flow meter readings (See Figure 5.1). For a variation in the flow depth (y) between 10 mm and 140 mm, using a Manning's "n" of 0.0086, and assuming longitudinal average depths. The Froude number (F_r) for this slope ($S_o = 0.00109$), varied from 0.43 to 0.50, and Reynolds' number changed from 1.6×10^3 to 7.1×10^4.

The preceding values of Manning's "n" can be compared with the following values; recommended by Chow (3) for design of glass conduits flowing partly full:

Minimum "n" = 0.009 ;
Normal "n" = 0.010, and
Maximum "n" = 0.013.

5.2 Dye Velocity Measurements

The study of the discharges computed from the dye measurements (Equation 4.1) shows that there is an average error of +0.6 U.S.G.P.M. (0.00004 m^3/s), compared with 15 U.S.G.P.M. (0.000945 m^3/s) possible error in reading the flow meter. Thus there is an excellent agreement between the flow meter readings and the discharges computed by Equation 4.1 using the dye measurements. Figure 4.15 compares the discharges of the flow meter and the discharges computed from the dye measurements for a critical slope of 0.0033. Figures 4.32 and 4.47 show the dye velocity measurements compared to Manning's velocities ($n = 0.0078$) for the critical and the supercritical slopes respectively, used in the experimentation.

The study of the dye velocity measurements compared to Manning's velocities ($n = 0.0078$) shows an average difference (ε) of +0.04 ft/sec. for the critical slope ($S_o = 0.0033$). The standard deviation (σ) for the dye velocity measurements (compared to the experimental mean curve) in this case is 0.05 ft/sec.

The average difference (ε) for the supercritical slope ($S_o = 0.0061$) is +0.11 ft/sec., and the standard deviation (σ) of the dye velocity measurements is 0.09 ft/sec.

5.3 Surge Characteristics

5.3.1 Surge Velocity (V_w)

The theoretical curves based on Equation 3.2 and experimental values of the surge velocity (V_w) for different discharges are given in Figures 4.23, 4.35, and 4.42 for critical, subcritical, and supercritical slopes respectively.

Figure 4.23 shows an average difference (ε) of −0.22 ft/sec. between the experimental mean curve and the theoretical curve (Equation 3.2) for the critical slope of 0.0033, the standard deviation (σ) of the experimental results (compared to the experimental mean curve) is 0.52 ft/sec.

Figure 4.35 shows an average difference (ε) of +0.13 ft/sec. between the experimental mean curve and the theoretical curve (Equation 3.2), for the subcritical slope (S_o = 0.00109), the standard deviation (σ) of the experimental results from the experimental mean curve is 0.14 ft/sec.

Figure 4.42 shows an average difference (ε) of +0.07 ft/sec. between the experimental mean curve and the theoretical curve (Equation 3.2), for the supercritical slope (S_o = 0.0061), the standard deviation (σ) of the experimental results from the experimental mean curve is 0.38 ft/sec.

Figure 5.2 shows the effect of bed slope (S_o) on the surge velocity (V_w). Both the theory (Equation 3.2) and the experiments show an increase in the surge velocity (V_w) with the increasing of bed slope (S_o); this occurs because the initial flow velocity v_1, used in Equation 3.2 to calculate the surge velocity (V_w), increases when the bed slope (S_o) increases.

The surge velocity (V_w) was measured for different discharges, using a 1.0 in. end sill. The form of the surge front was also recorded as shown in Figure 4.36. The use of the end sill was recommended when the flow was observed to be gradually varied, for the subcritical slope (S_o = 0.00109). The sill produced a more uniform flow for intermediate depth as Figure 4.34 indicates.

5.3.2 Downstream Piezometric Head (Z)

The theoretical curves based on Equation 3.17 and experimental results of the downstream piezometric head (Z) relative to the sewer crown due to a sudden closure of the downstream end of the pipe, are given in Figures 4.25, 4.37, and 4.43 for critical, subcritical, and supercritical slopes respectively.

Figure 4.25 shows an average difference (ε) of +1.83 cm between the experimental mean curve and the theoretical curve (Equation 3.17), for critical bed slope of 0.0033, the standard deviation (σ) of the experimental results from the experimental mean curve is 2.07 cm.

Figure 4.37 shows an average difference (ε) of +10.3 cm between the experimental mean curve and the theoretical curve (Equation 3.17), for subcritical slope (S_o = 0.00109), the standard deviation (σ) of the experimental results from the experimental mean curve is 2.65 cm. As mentioned before, the flow was observed to be gradually varied at this slope.

Figure 4.43 shows an average difference (ε) of +1.0 cm between the experimental mean curve and the theoretical curve (Equation 3.17), for the supercritical slope (S_o = 0.0061), the standard deviation (σ) of the experimental results from the experimental mean curve is 1.8 cm.

Figure 5.3 shows the effect of bed slope (S_o) on the downstream piezometric head (Z) relative to the sewer crown. Both the theory (Equation 3.17) and experiments show that an increase in the bed slope causes an increase in the end piezometric head (Z).

5.3.3 Height of Free Surges

The theoretical and observed surge heights (h) were recorded for different initial flow depths, are shown in Figure 4.24 for critical slope of 0.0033.

Figure 4.24 shows an average difference (ε) of -1.5 cm between the experimental mean curve and the theoretical curve (Equations 3.2 and 3.9), the standard deviation (σ) of the experimental results from the experimental mean curve is 0.89 cm.

5.4 Hydrographs

5.4.1 Routing the Inlet Hydrograph

Discharge-storage curves (Figure 5.4) were prepared using the known surface areas for the two compartments of the overhead tank, and the discharge-stage curves given in Figure 4.22. The following equation was used for the hydrograph routing:

$$\left(\frac{S}{\Delta t} + \frac{O}{2}\right)_2 = \left(\frac{S}{\Delta t} + \frac{O}{2}\right)_1 + \frac{1}{2}\,(I_1 + I_2) - O_1 \qquad (5.2)$$

An additional routing curve $(S/\Delta t + O/2)$ vs O was computed for a selected routing period Δt of 2.0 sec. (Figure 5.5). Using the initial conditions, i.e., the base flow O_1, and the given input hydrograph, all the values on the right hand side of Equation 5.2 are known and hence the left hand side of the equation can be computed. After obtaining

$(\frac{S}{\Delta t} + \frac{O}{2})_2$, the outflow O_2 can be read from the graph (Figure 5.5); the procedure is then repeated for subsequent time steps.

The outlet hydrographs from the two compartments were added to get the final inlet hydrograph entering the pipe.

5.4.2 Time Lag Between the Inlet and Outlet Hydrographs

From the inlet and outlet hydrographs' results, Figures 4.27, 4.28, 4.29, 4.38, 4.39, 4.40, 4.44, 4.45, and 4.46, for critical, subcritical, and supercritical slopes used in the experimentation dimensionless lag time curves, for both the rising and recession limbs, can be prepared for different dimensionless storm durations for each of the slopes. Figures 5.6, 5.7, and 5.8 show the prepared curves for subcritical, critical, and supercritical slopes respectively. The lag time $(\overline{\Delta})$ represents the average lag time between the rising or recession limbs of the inlet and outlet hydrographs, and t_{kw} is the time required for the kinematic wave to reach the test section at 41.5 ft from the upstream end of the pipe. The value of t_{kw} can be computed from the following equation:

$$t_{kw} = \frac{\ell}{V_{kw}} = \frac{\ell(A_{peak} - A_{base})}{(Q_{peak} - Q_{base})} \qquad (5.3)$$

where,

ℓ = distance travelled by the kinematic wave from the upstream end of the pipe to the measurement point of measurement of the outlet hydrograph (ℓ = 41.5 ft).

V_{kw} = velocity of the kinematic wave (ft/sec.).

Q_{base} = base discharge (cfs)

Q_{peak} = peak discharge of the inlet hydrograph (cfs)

A_{base} = area of flow of the base discharge (ft^2)

A_{peak} = area of flow of the peak discharge of the inlet hydrograph (ft^2).

Figure 5.6 shows an average dimensionless lag time of 0.83, and standard deviation of 0.29 for the subcritical slope (S_o = 0.00109).

Figure 5.7 shows an average dimensionless lag time of 0.6, and standard deviation of 0.17 for the critical slope (S_o = 0.0033).

Figure 5.8 shows an average dimensionless lag time of 0.75, and standard deviation of 0.29 for the supercritical slope (S_o = 0.0061).

Table 5.1 shows the average lag time ($\overline{\Delta T}$), between the outlet and the inlet hydrographs for different storm durations and different slopes. ΔT represents the distance between the two centroids of the outlet and the inlet hydrographs. The value of time centroid was calculated by

$$\overline{X} = \frac{\sum(\overline{x}\ A_s)}{\sum A_s} \qquad (5.4)$$

where,

A_s = area of strip (vertical strip, 4 seconds wide), and

$\overline{x}$ = distance of the centroid of the area of strip from y-axis (discharge axis).

Table 5.1

Average Lag Time for Different Slopes

Bed Slope (S_o)	Average lag time ($\overline{\Delta T}$) sec.
Subcritical (0.00109)	13.7
Critical (0.0033)	3.9
Supercritical (0.0061)	9.8

5.4.3 The Effect of the Storm Duration (t_d)

The hydrograph results show that the dimensionless difference in the peak discharges of the inlet and outlet hydrographs ($\frac{\Delta Q}{Q_{max.}}$) decreases when the storm duration (t_d) increases, ΔQ and $Q_{max.}$ were defined before (Article 5.4.3).

Figure 5.9 shows the effect of storm duration (t_d) on ($\frac{\Delta Q}{Q_{max.}}$), for different bed slopes, Figure 5.10 shows this effect for dimensionless storm duration ($\frac{t_d}{t_{kw}}$).

Figure 5.11 shows that the dimensionless hydrograph width ($W_{o_{50}}/W_{i_{50}}$) increases with the increasing of storm duration up to about 30 sec. and then decreases with the increasing of storm duration (t_d); $W_{o_{50}}$ represents the outlet hydrograph width at 50% of the maximum discharge, and $W_{i_{50}}$ is the inlet hydrograph width at 50% of the maximum discharge. Figure 5.12 shows the dimensionless hydrograph width ($W_{o_{50}}/W_{i_{50}}$) against the dimensionless storm duration ($\frac{t_d}{t_{kw}}$).

5.4.4 The Effect of the Bed Slope (S_o)

The hydrograph results show that the dimensionless difference in the peak discharges of the inlet and outlet hydrographs ($\frac{\Delta Q}{Q_{max.}}$) decreases when the bed slope (S_o) increases; where ΔQ represents the difference between the peak discharges of the inlet and the outlet hydrographs, and $Q_{max.}$ is the peak discharge of the inlet hydrograph. Figure 5.13 shows the effect of bed slope on ($\frac{\overline{\Delta Q}}{Q_{max.}}$).

Table 5.4 shows that the average dimensionless hydrograph width ($\frac{\overline{W_{o_{50}}}}{W_{i_{50}}}$) decreases with the increasing bed slope (S_o), where $W_{o_{50}}$ and $W_{i_{50}}$ are defined in Article 5.4.3.

Table 5.2

Average Dimensionless Hydrograph Width for Different Bed Slopes

Bed Slope (S_o)	$\left(\frac{\overline{W_{o_{50}}}}{W_{i_{50}}}\right)$
Subcritical (0.00109)	1.40
Critical (0.0033)	1.39
Supercritical (0.0061)	1.31

Table 5.5 shows an average error of about +7.7% between the computed areas under the outlet and the inlet hydrographs.

Table 5.3

The Average Error Between the Areas Under the Hydrographs for Different Slopes

Bed Slope (S_o)	$\left(\frac{A_{oh} - A_{ih}}{A_{oh}}\right) \times 100$
Subcritical (0.00109)	+9%
Critical (0.0033)	+8%
Supercritical (0.0061)	+6%

where,

A_{oh} = area under the outlet hydrograph, and

A_{ih} = area under the inlet hydrograph.

The computed values in Table 5.3 represent the average values for different storm durations at each slope.

5.5 Effect of Ventilation

The effect of the air vents (shown in Figure 4.2) on the piezometric head (Z) at the downstream end of the pipe, for different initial flow depths, is shown in Figures 4.30 and 4.31.

Table 5.4 shows an average decrease in (Z) of 23.1%, when both vents were open, and an average decrease of 11.8%, when only one vent was open. The effect of air is considered for all the theoretical values of (Z) computed in this study.

Table 5.4

The Effect of Air Vents on the Downstream Piezometric Head

Z (cm) Both Vents Open	Z (cm) One Vent Open	Z (cm) Both Vents Closed
13.5	16.0	18.5
16.5	19.0	21.0
19.0	21.0	24.0

Figure 5.14 indicates the variation in the exit loss coefficient, K_{exit}, for the two air vents, used for the pressure drop calculations (Equation 3.21), for different flow depths.

5.6 Effect of Trapped Air

The movement of surges for initial relative flow depth ($\frac{y_1}{H}$) higher than 0.8 was observed to be accompanied by the formation of a bubble due to the instability at the upstream end of the pipe (see Figure 3.4). The bubble that is formed is compressed by the inflow discharge and the surge front. This compression yields an increase in the pressure inside the storm sewer model. The downstream piezometric head (Z) will be increased by (ΔZ) according to Equation 3.32, which can be approximated in the same way as in the analysis of fluid motion after the bubble formation (Article 3.3), then

$$(\Delta Z) = \frac{p_o}{\gamma}\left(1 + S\,\frac{A}{\forall_o}\right) - \frac{p_{at}}{\gamma} \qquad (5.5)$$

Table 5.5 shows typical values of (ΔZ) calculated according to Equations 3.32 and 5.5 for $\ell' = 40$ ft, $\ell_{b_1} = 36$ ft, $h_2 = 0.29$ ft, $S_o = 0$, $p_o = (p_{at} + 1.0)$ ft, using Manning's formula for V_o, and the maximum value of S of Equation 3.31.

A typical (S-t) curve representing Equation 3.31, for the above conditions and for a relative initial flow depth ($\frac{y_1}{H}$) of 0.93, is shown in Figure 5.15.

Table 5.5

The Effect of Initial Relative Flow Depth on (ΔZ)

Initial Relative Flow Depth ($\frac{y_1}{H}$)	ΔZ Eq. 3.32 (ft)	ΔZ Eq. 5.5 (ft)	Error (%)
0.80	12.053	9.40	-22%
0.86	16.669	11.823	-29%
0.93	30.576	17.045	-44%

The initial bubble length (ℓ_{b_1}) has no significant effect on the results of Equation 5.5, but it affects the time period (t) required to complete one cycle of the compression and expansion of the bubble given by Equation 3.31.

Table 5.6 shows the effect of the initial bubble length (ℓ_{b_1}) on the time period (t) for two cases of initial relative depth of flow ($\frac{y_1}{H}$). The Table shows an average increase of 174% in the time period for a corresponding increase of 200% in the initial bubble length.

Table 5.6

The Effect of Initial Bubble Length on (t)

Initial Relative Flow Depth ($\frac{y_1}{H}$)	Time (t) For ℓ_{b_1} = 12 ft (sec.)	Time (t) For ℓ_{b_1} = 36 ft (sec.)
0.80	0.69	1.89
0.93	1.20	3.29

The approximation given by Equation 5.5 is inaccurate for initial relative depth of flow $(\frac{Y_1}{H})$ more than 0.80 (see Table 5.5).

This analysis explains one reason for the deviation of the experimental downstream piezometric heads (Z) from the theoretical values based on Equation 3.17 at a relative initial flow depth $(\frac{Y_1}{H})$ higher than 0.8.

5.7 Experimental Errors

The experimental errors in this study may be summarized as follows:

A. The error that might occur in each measurement of the [illegible]rge transit time is estimated to be ± 0.3 sec. For an average travelled length of the surge of 15 ft with an average velocity of 5 ft/sec., the standard error in each measurement of V_w will be about 10%. The standard error in the mean of three readings would be about 5.8%.

B. The error that might occur in the measurement of the downstream piezometric head (Z), using a piezometric tube, is estimated to be 10%, due to the fluctuation of Z between its maximum and minimum values for each surge.

C. The error that might occur in the measurement of the height of the free surge (h) is estimated to be 2 mm (one division of the side scale used for the measurements), for an average height of 4 cm for the surges, this error will be about 5%.

D. The errors that might occur in the measurement of the inflow discharge (I) into the overhead tank are estimated to be:

(i) A possible error of the flow meter precision is of 15 U.S.G.P.M. (0.000945 m^3/s).

(ii) The error of evaluation of flow meter reading is estimated to be 1 mm on the flow meter scale, which represents 12.5 U.S.G.P.M. (0.000788 m^3/s).

E. The error that might occur in the measurement of initial flow depth (y_1) for the surge measurements is estimated to be 4%.

F. The errors that might occur in the measurement of the depth of flow during the hydrograph tests are estimated to be:

(i) A possible error of ± 0.5% was assumed for the pressure transducers used to measure the flow depth.

(ii) A calibration error of ± 1% for estimating the flow depth from the pressure transducer recordings.

(iii) A maximum error of approximately -0.50 mm due to the location of the pressure transducer at about one foot downstream of the test section for the laser anemometer velocity measurements (see Figure 4.14). This error is about 1% at the average depth.

(iv) An instrument error of about 0.5% was assumed for the recorder used to record the flow depth during the hydrograph tests.

The net standard error from the above sources, for the flow depth measurements will be 0.8%.

G. The errors that might occur in the measurement of the velocity of flow during the hydrograph tests are estimated to be:

(i) A 1% calibration error is assumed for the recorded laser anemometer velocity readings.

(ii) A 1% error is assumed for using the correction factor (Figure 4.16) which was used to find the average velocity of flow through the test section.

(iii) An instrument error of about 0.5% was assumed for the recorder used to record the velocity of flow during the hydrograph tests.

H. The errors that might occur in the measurement of the storm duration (t_d) is assumed to be:

(i) A possible error of one second is assumed due to the sudden transfer for the flow from the small compartment of the overhead tank to the big one.

(ii) A possible error of one second is assumed for closing the delivery valve on the pump.

I. An increase in the discharge of about 50% for about 2 seconds is expected due to the surge effect in the large compartment when the flow was switched from the small compartment.

5.8 Discussion

5.8.1 Surge Analysis

The study of the experimental surge velocity (V_w) for different slopes is in good agreement with the theory based on Equation 3.2. Table 5.7 shows that the theory (Equation 3.2) gives surge velocities (V_w) within the standard error of the experimental results.

Table 5.7

The Agreement Between the Experimental Surge Velocities (V_w) and the Theory (Equation 3.2) for Different Slopes

Bed Slope (S_o)	$(\frac{\varepsilon}{\sigma})$	Degree of Agreement
Subcritical Slope (0.00109)	+0.93	Good
Critical Slope (0.0033)	−0.42	Very Good
Supercritical Slope (0.0061)	+0.18	Excellent

In Table 5.7, ε represents the average difference between the experimental mean curve and the theoretical curve based on Equation 3.2; σ represents the standard deviation of the experimental results from the experimental mean curve; and the degree of agreement is based on the following assumptions:

For $(\frac{\varepsilon}{\sigma}) = 0 \rightarrow 0.30$ Excellent agreement;

For $(\frac{\varepsilon}{\sigma}) = 0.30 \rightarrow 0.60$ Very Good agreement;

For $(\frac{\varepsilon}{\sigma}) = 0.60 \rightarrow 1.00$ Good agreement;

For $(\frac{\varepsilon}{\sigma}) = 1.0 \rightarrow 2.00$ Fair agreement, and

For $(\frac{\varepsilon}{\sigma}) > 2.00$ poor agreement.

The theory (Equation 3.2) and experiments (Figure 5.2) show that V_w increases when the bed slope increases.

The theory (Equation 3.17) and experiments (Figure 5.3) show that the downstream piezometric head (Z) increases when the bed slope (S_o) increases, which is expected because of the accompanying increase in the initial velocity.

Table 5.8 shows that the theory (Equation 3.17) gives downstream piezometric heads (Z) within the standard error of the experimental results for the critical and the supercritical slopes.

Table 5.8

The Agreement Between the Experimental Downstream Piezometric Heads (Z) and the Theory (Equation 3.17) for Different Slopes

Bed Slope (S_o)	$(\frac{\varepsilon}{\sigma})$	Degree of Agreement
Subcritical slope (0.00109)	+3.89	Poor
Critical slope (0.0033)	+0.88	Good
Supercritical slope (0.0061)	+0.56	Very Good

The experimental results for the subcritical slope show a poor agreement with the theory (Equation 3.17). The experimental results are consistently higher than the theory. A possible reason for this difference is the blockage of the air vents at the upstream end of the pipe due to the gradually varied flow which was observed at this slope. It was previously observed that the blockage of the air vents can cause in increase of about 23% in the value of (Z) as calculated by Equation 3.17.

The agreement indicated in Table 5.8 applied up to $(\frac{y_1}{H}) \simeq 0.8$.

The experimental readings of (Z) were out of the range of the scale of the downstream piezometric tube, i.e., greater than 150 cm, when the initial relative depth of flow $(\frac{y_1}{H})$ exceeded 0.8 for all the slopes. A possible explanation for this rapid increase in Z is the effect of trapped air in the pipe which resulted from the instability at the upstream end of the pipe (see article 5.6). As a result of this instability a bubble (or bubbles) was trapped in the pipe. The theory introduced in article 3.3 and approximated by Equation 5.5 confirms that a large increase in Z would occur due to bubble formation.

The measured heights of free surges (h) are in fair agreement with the theoretical values based on Equations 3.2 and 3.9. For critical slope ($S_o = 0.0033$), the value of $(\frac{\varepsilon}{\sigma})$ is -1.69.

5.8.2 Hydrograph measurements

The analysis of the hydrograph measurements shows that the area under the outlet hydrograph is +7.7% on the average larger than the area under the inlet hydrograph. The possible reasons for this can be summarized as follows:

A. An error in the estimation of the inflow (I) into the overhead tank (using the flow meter), which is used for the inlet hydrograph routing (approximately 2%).

B. The errors that might occur by using the routing curves (Figures 5.4 and 5.5) for the routing of the inlet hydrograph (approximately 1%).

C. The errors that might occur in the measurement of the storm duration (t_d), (approximately 3%).

D. The surge in large compartment that followed the transfer of flow from the small compartment, could have caused an increase in ~~the total~~ volume of the inlet hydrograph as shown in Figure 5.16. This error could be as high as 10%.

E. The errors in the outlet hydrograph measurements (approximately 2.2%).

The error due to items A, B, and C is about 3.7%, and the error due to item E is about 2.2%. Since these errors cannot account for the 7.7% observed difference, therefore the disagreement between the inlet and outlet hydrograph volumes must be primarily due to the initial surge that occurs on transfer of the flow from the small compartment to the large compartment.

The dimensionless difference in the peak discharges of the outlet and inlet hydrographs (Figure 5.10) decreases when the dimensionless storm duration ($\frac{t_d}{t_{kw}}$) increases. This was expected because of the equilibrium between the outlet and inlet hydrograph peaks that takes place after a limited time.

The dimensionless hydrograph width ($\frac{W_{o_{50}}}{W_{i_{50}}}$) remains fairly constant when the dimensionless storm duration ($\frac{t_d}{t_{kw}}$) increases until about a dimensionless storm duration of 3, and then decreases as the dimensionless storm duration decreases (see Figure 5.12), because of the equilibrium between the outlet and inlet hydrograph peaks that takes place after a limited time.

When the bed slope (S_o) increases the dimensionless difference in the peak discharges of the outlet and inlet hydrographs ($\frac{\Delta Q}{Q_{max}}$) decreases, because the residence time decreases with increasing slope, thus permitting less spreading of the flood wave.

Recommendations

As a result of this study the following modifications in the storm sewer model are suggested:

(i) A mechanical system is recommended to transfer the flow between the two compartments of the overhead tank to prevent the surge that was produced in the large compartment.

(ii) An improved mechanism for closing the downstream end of the pipe is recommended to prevent the leakage at higher discharges.

(iii) It is recommended that the measurement point for the flow depths be located at the channel bottom of the velocity measurement section.

(iv) . A longer downstream piezometric tube is recommended to record the high piezometric heads (Z) produced from the surges with initial relative depths $(\frac{Y_1}{H})$ higher than 0.8. The pressure transducer could also be used for this purpose. Circular pipes should be included in future study.

CHAPTER VI

CONCLUSIONS

The conclusions of this study are considered in two parts:

A. Those relating to the surge analysis,

B. Those relating to the hydrograph measurements.

6.1 Surge Analysis

The experimental analysis shows a good agreement between the measured surge velocities (V_w), and the theoretical surge velocities (Equation 3.2), up to a certain limit of $(\frac{y_1}{H})$ as indicated in Figure 3.5. The flow regime will change from stratified flow to wave flow at a certain depth (Figure 3.5) and the theory can not be applied. Also for high $\frac{y_1}{H}$ the time measurements are difficult and subjected to large errors because of the high velocity of the moving surges.

The experimental analysis of the downstream piezometric heads (Z) shows a good agreement between the measurements and the theory based on Equation 3.17, for critical and supercritical slopes up to about $\frac{y_1}{H} \approx 0.8$. The poor agreement between the theory and experiment for subcritical slope for

$\frac{Y_1}{H} > 0.7$ is explained (see Article 5.8) by the effect of entrapped air.

The analysis of trapped air in the pipe (due to the instability at the upstream end) explains the increase in the downstream piezometric head (Z) as shown in Table 5.5.

6.2 Hydrograph Measurements

The analysis of the hydrograph results shows that the dimensionless difference in the peak discharges of the outlet and inlet hydrographs decreases when the bed slope increases and when the dimensionless storm duration $(\frac{t_d}{t_{kw}})$ increases.

Figure 5.17 shows that the average lag time $(\overline{\Delta T/t_{kw}})$ can be calculated with sufficient accuracy from the kinematic wave theory.

The coupling of the laser anemometer with a pressure transducer, used in the experimental study, has proved to be useful in measuring outlet hydrographs with high accuracy.

APPENDIX (A)

DETERMINATION OF THE LIMIT SLOPE OF THE PIPE

The limit slope (the smallest critical slope) can be determined graphically from a curve of the critical slope plotted against the depth of flow (y_1). For the determination of a critical slope for a rectangular section, the following two conditions should be satisfied:

$$(1) \qquad Q = \frac{1.49}{n} AR^{2/3} \sqrt{S_c} = \frac{1.49}{n} By_1 \left(\frac{By_1}{B + 2y_1}\right)^{2/3} \sqrt{S_c} \qquad (A.1)$$

$$(2) \qquad Q = Z_c \sqrt{g} = B\sqrt{g}\, y_1^{1.5} \qquad (A.2)$$

Equating Equation A.1 to Equation A.2 yield S_c as a function of y_1. Following this procedure, the relation between y_1 and S_c was computed and plotted as shown in Figure A.1. The plotted curve indicates a minimum value of $S_c = 0.003$.

According to the limit slope obtained, and for practical considerations, the subcritical, critical, and supercritical slopes were chosen as: 0.00109, 0.0033, and 0.0061 respectively (see Figure A.1).

FIGURES

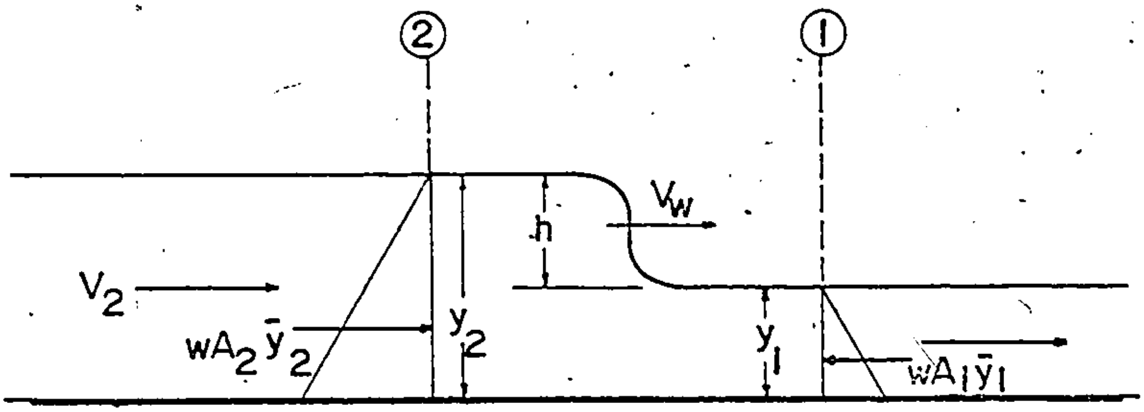

Fig. 2.1 Rapidly Varied Uniformly Progressive Flow after Chow (3)

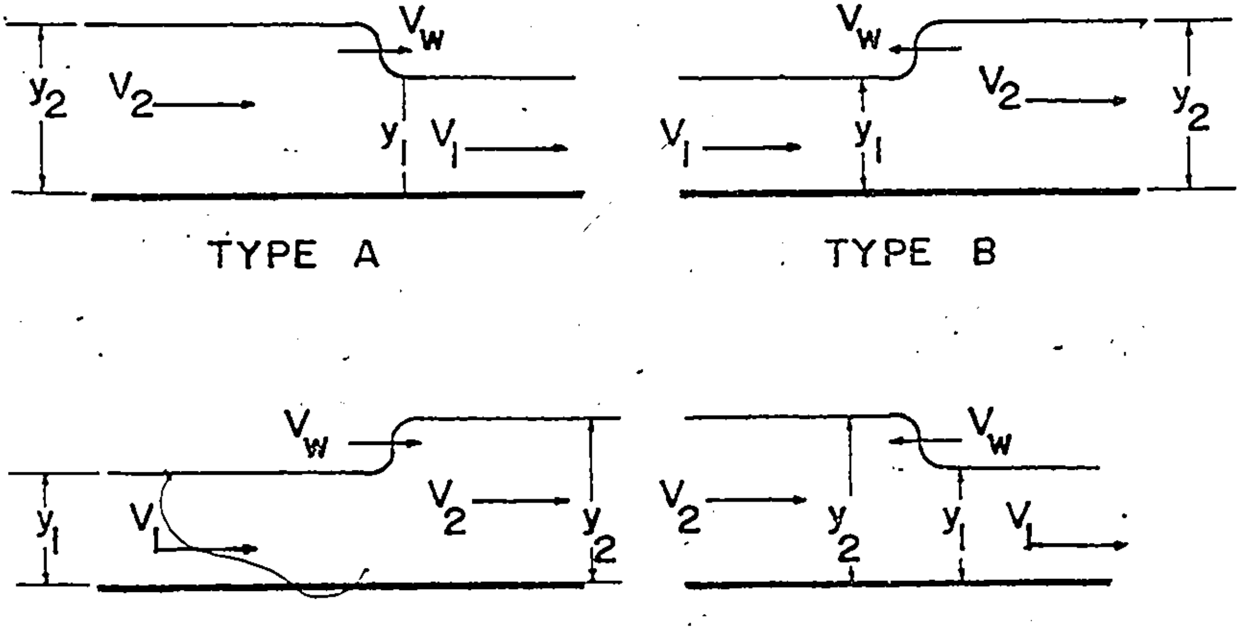

TYPE A

TYPE B

TYPE C

TYPE D

Fig. 2.2 Four Types of Rapidly Varied Uniformly Progressive Flow after Chow (3)

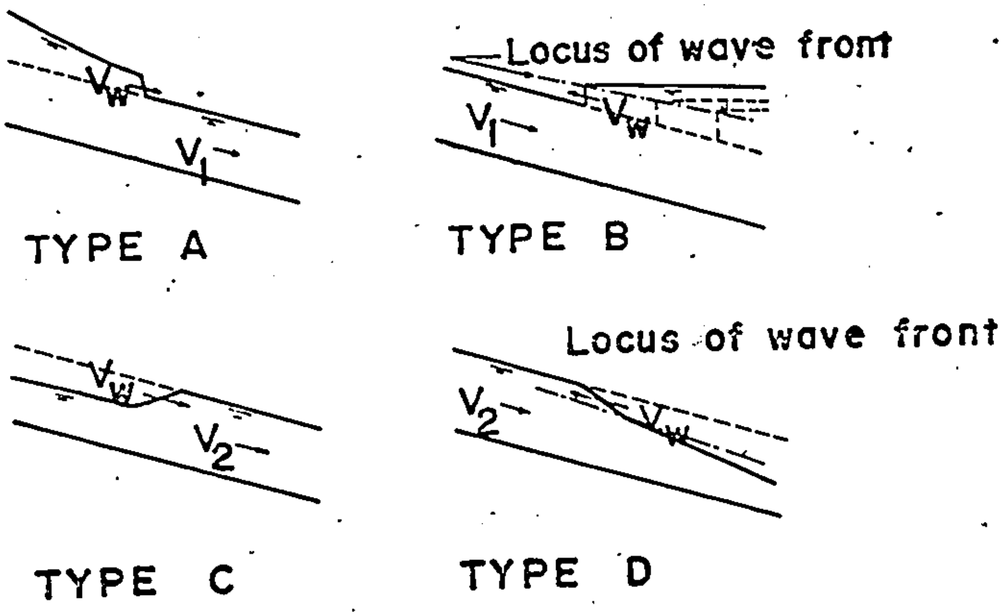

Fig. 2.3 Rapidly Varied Flow in Inclined Channels after Chow (3)

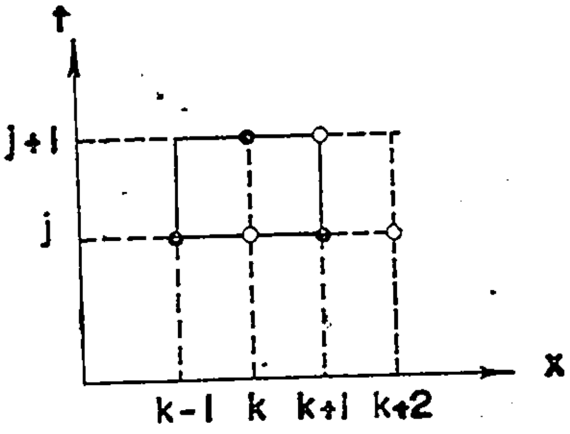

Fig. 2.4 Simple Explicit Diffusing Scheme after Terzidis and Strelkoff (14)

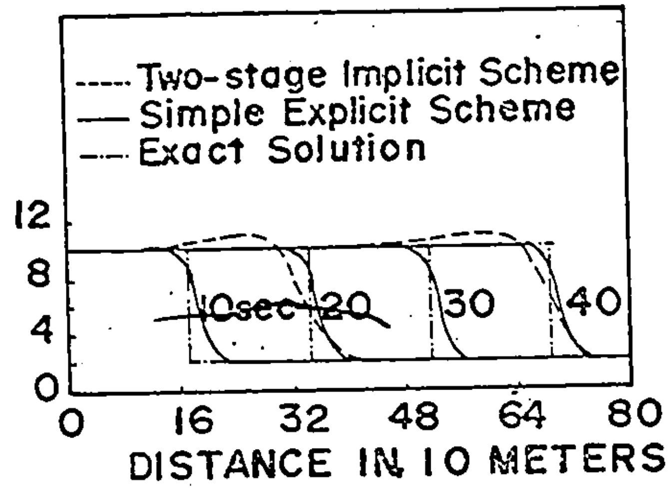

Fig. 2.5 Uniform Motion of a Discontinuity (Frictionless) after Terzidis and Strelkoff (14)

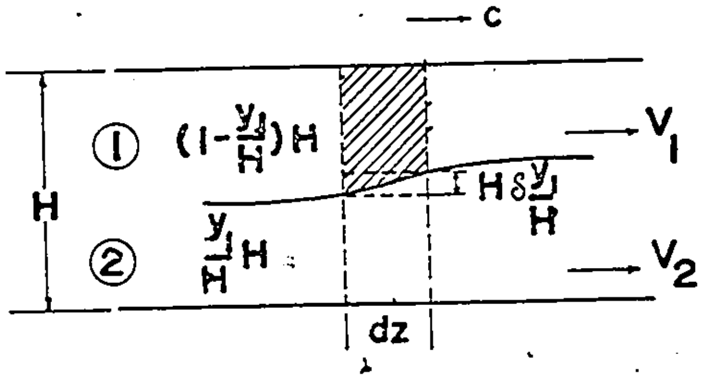

Fig. 2.6 Dynamic Wave Propagation in Two Incompressible Stratified Components in a Horizontal Duct after Wallis (16)

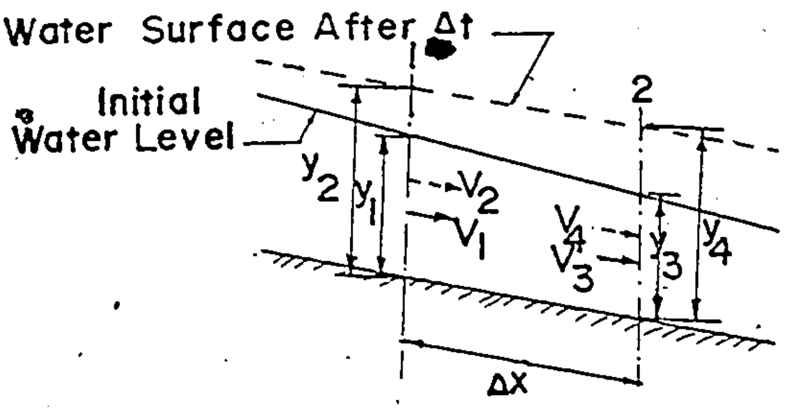

Fig. 2.7 Definition Sketch for the Method of Finite Increments after Thomas (15)

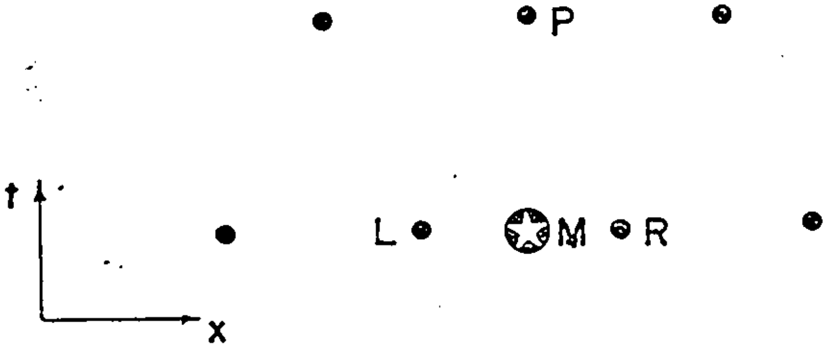

Fig. 2.8 Staggered Net Point Lattice in Interior after Isaacson, Stoker and Troesch (7)

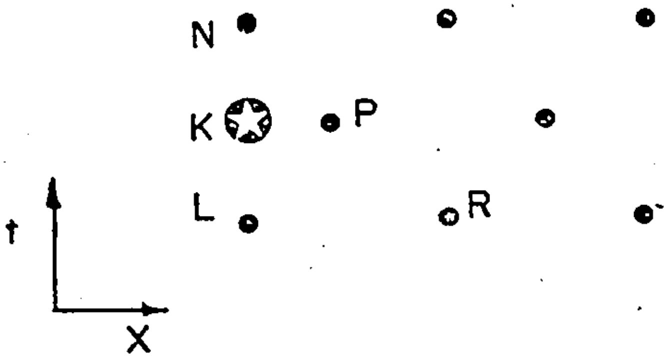

Fig. 2.9 Net Point Scheme at Left Boundary after Isaacson, Stoker and Troesch (7)

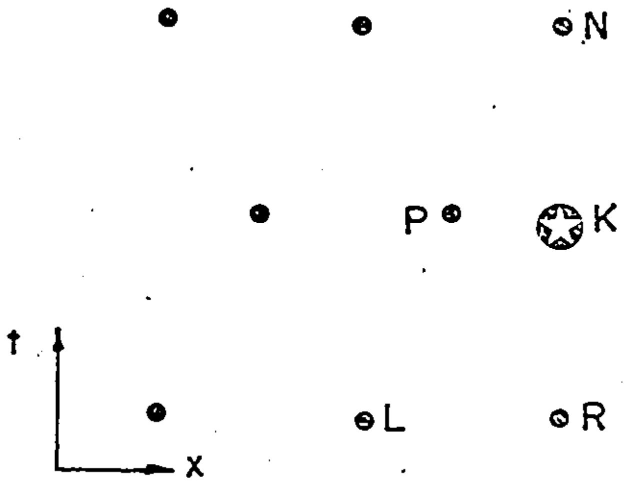

Fig. 2.10 Net Point Scheme at Right Boundary after Isaacson, Stoker and Troesch (7)

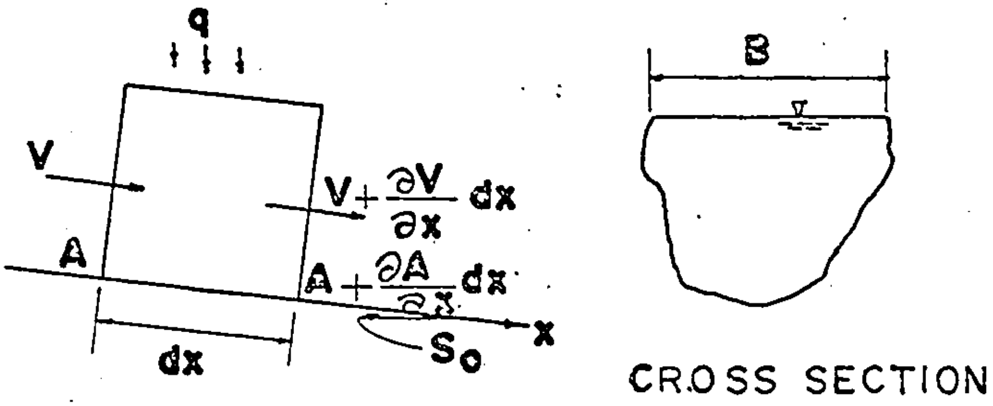

Fig. 2.11 Flow Increment for the Continuity Equation after Morgali (9)

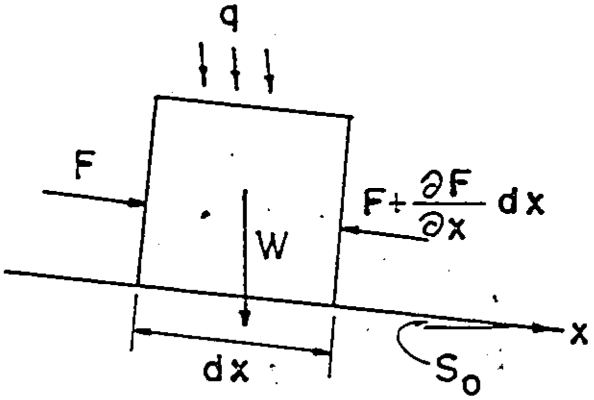

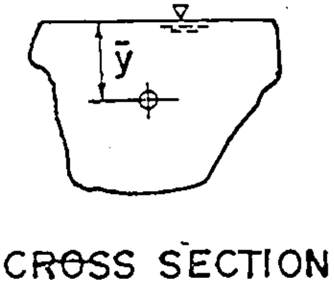

Fig. 2.12 Flow Increment for the Momentum Equation after Morgali (9)

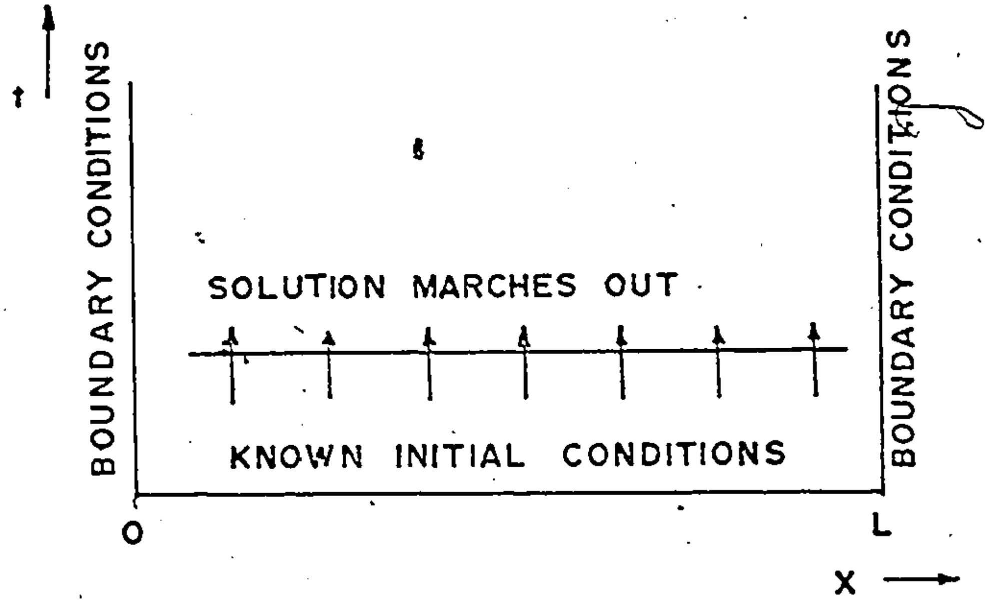

Fig. 2.13 Boundary Value Flow Picture after Morgali (9)

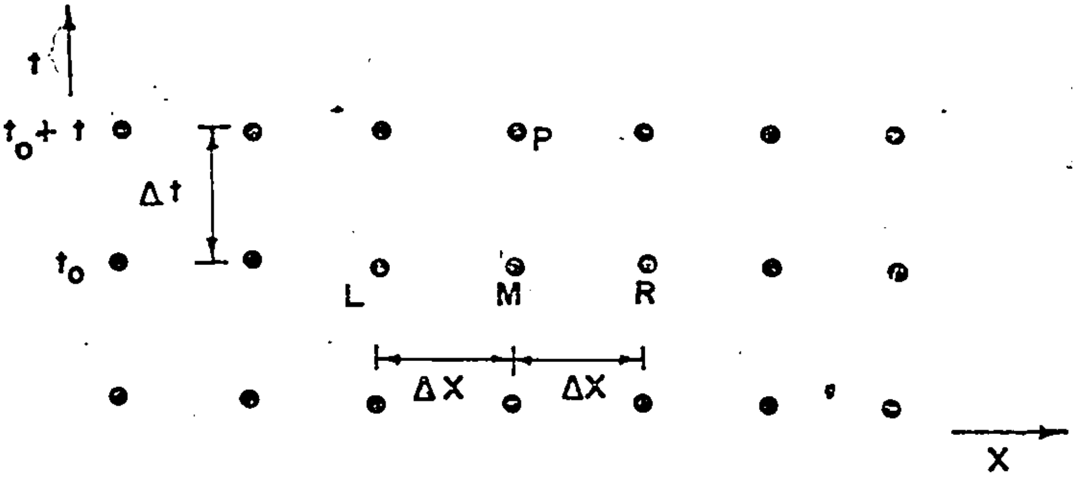

Fig. 2.14 Point Network Showing Finite Differences after Morgali (9)

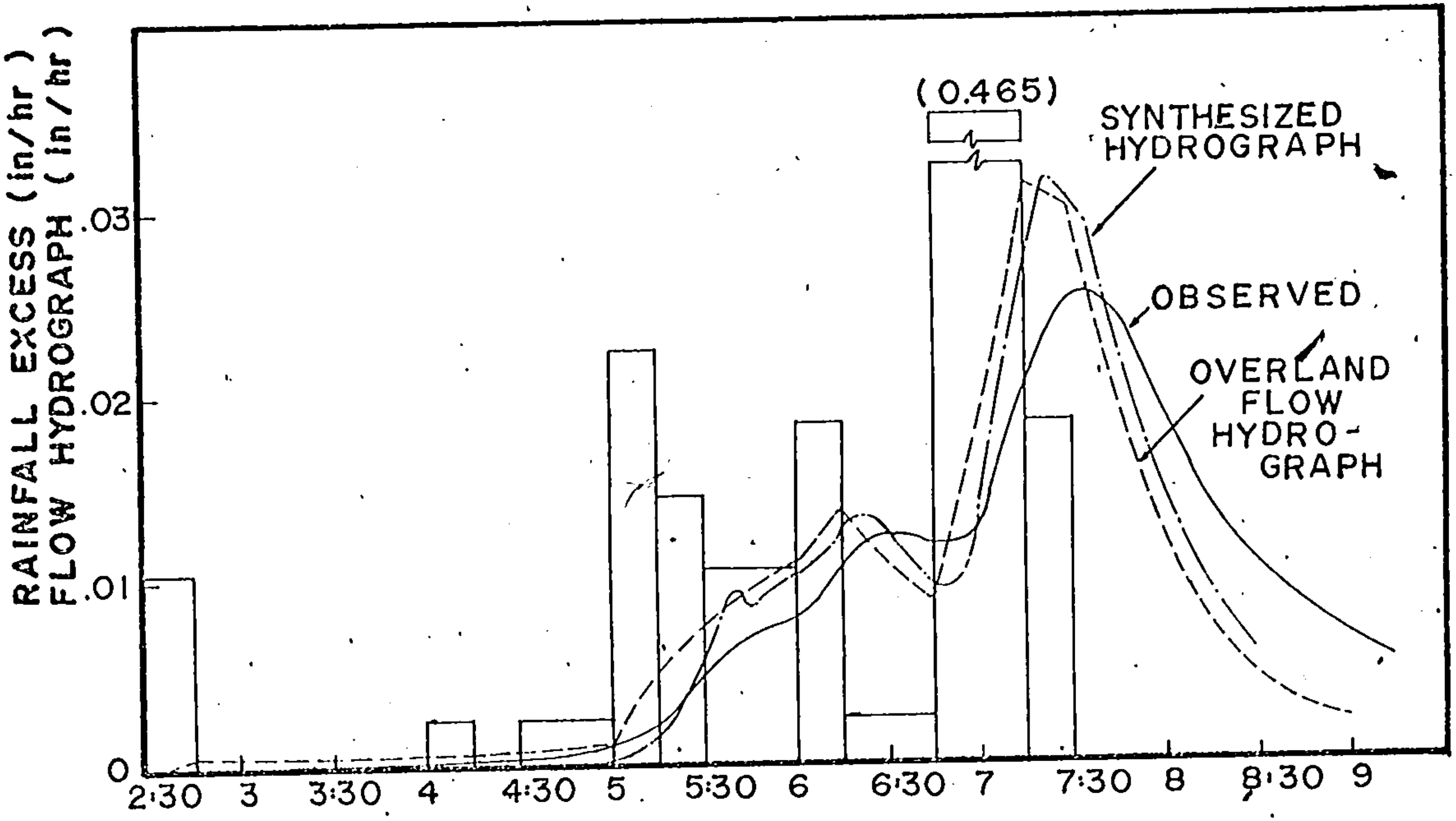

Fig. 2.15 San Francisquito Creek Basin-Overland Flow and Outflow Hydrographs after Morgali (9).

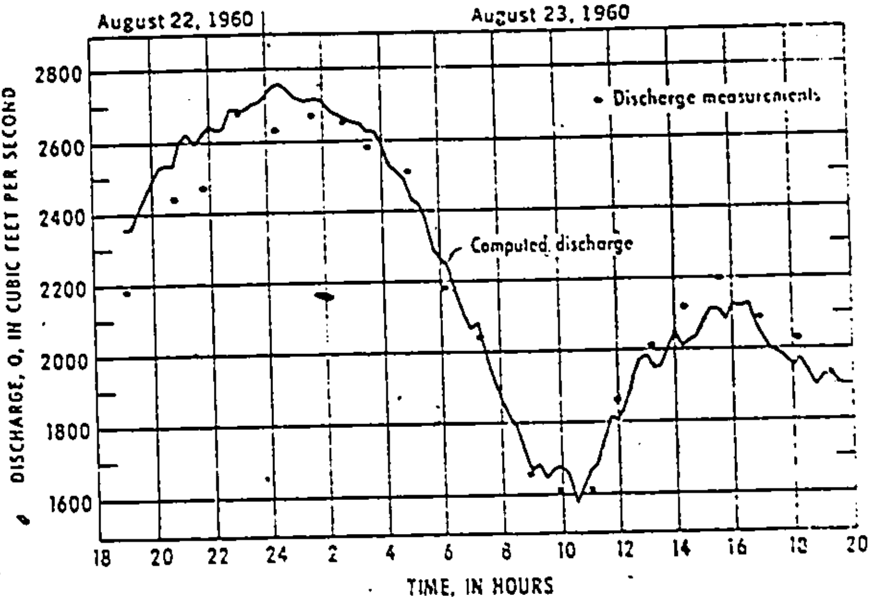

Fig. 2.16 Computed and Measured Discharge, for Vermilion River at Perry, L.A., During Portions of August 22-23, 1960 after Blatzer and Lai (2)

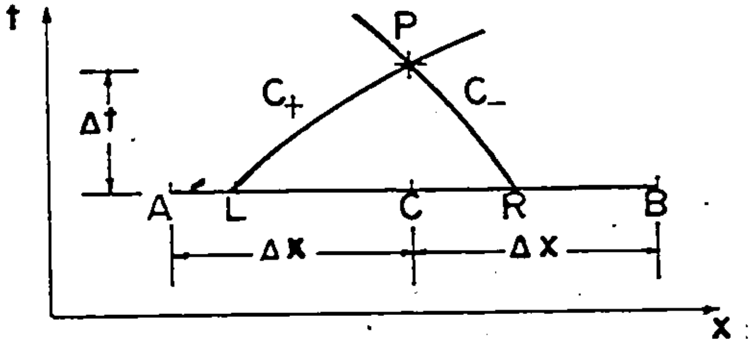

Fig. 2.17 Characteristics Triangle after Mozaneny and Song (10)

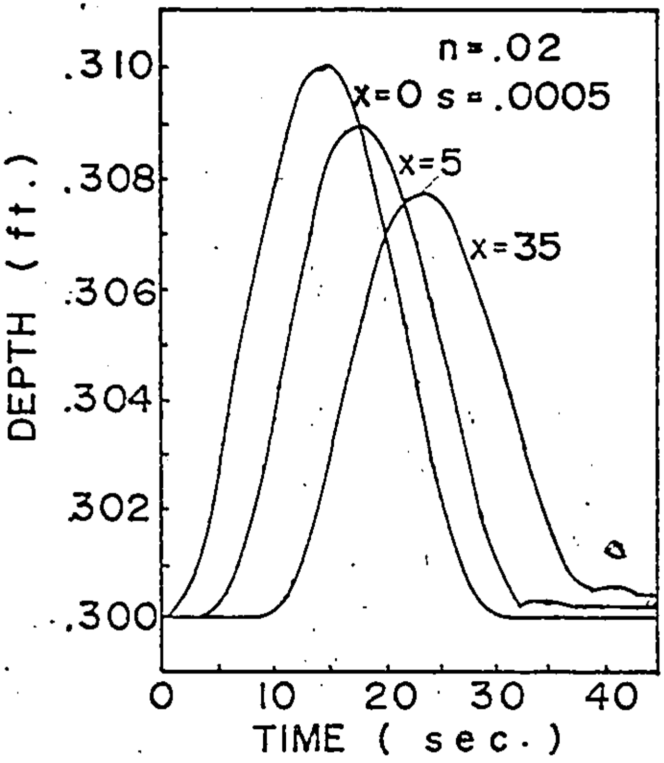

Fig. 2.18 Typical Stage Hydrographs
after Mozaneny and Song (10)

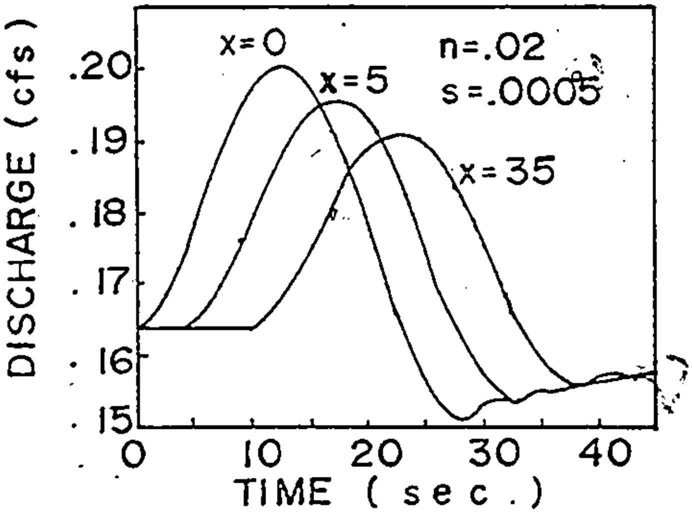

Fig. 2.19 Typical Discharge Hydrographs
after Mozaneny and Song (10)

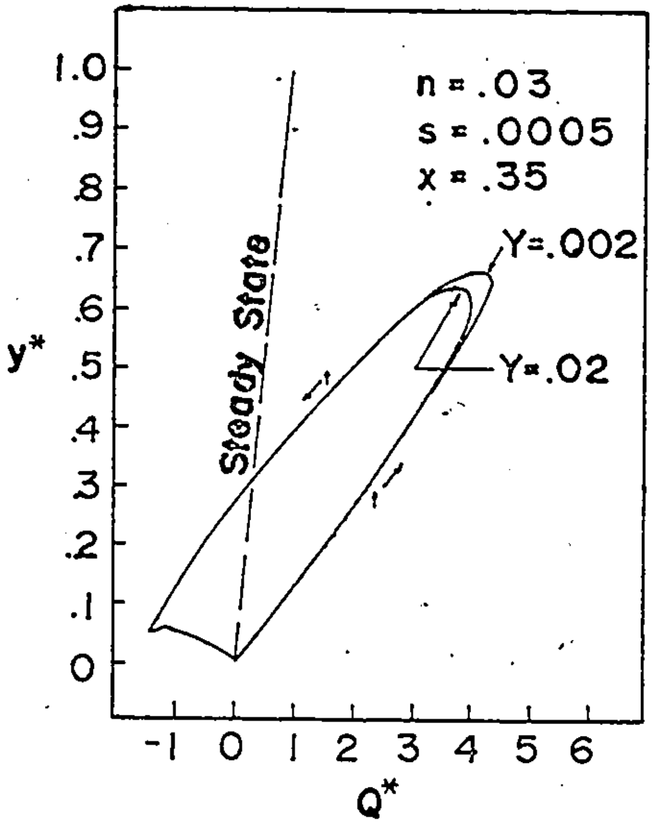

Fig. 2.20 Typical Dimensionless Rating Curves Showing Effect of Amplitude after Mozaneny and Song (10)

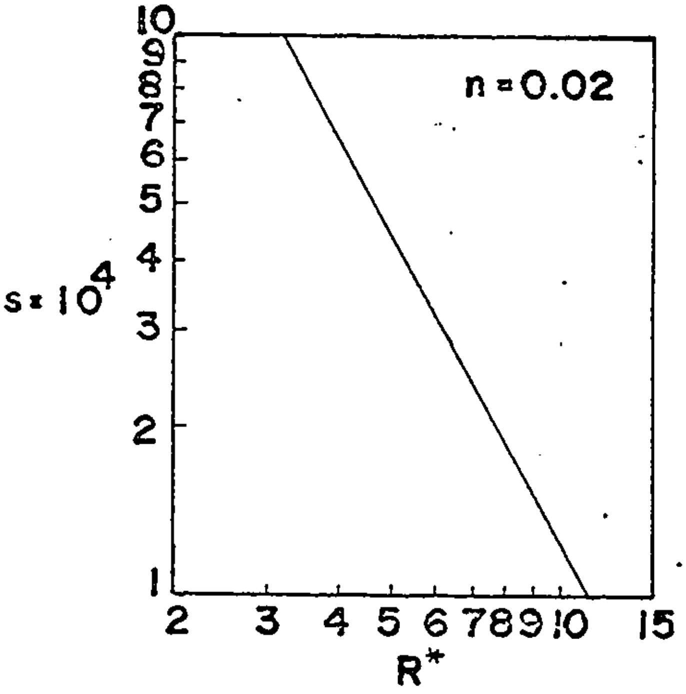

Fig. 2.21 Effect of Channel Slope on R* after Mozaneny and Song (10)

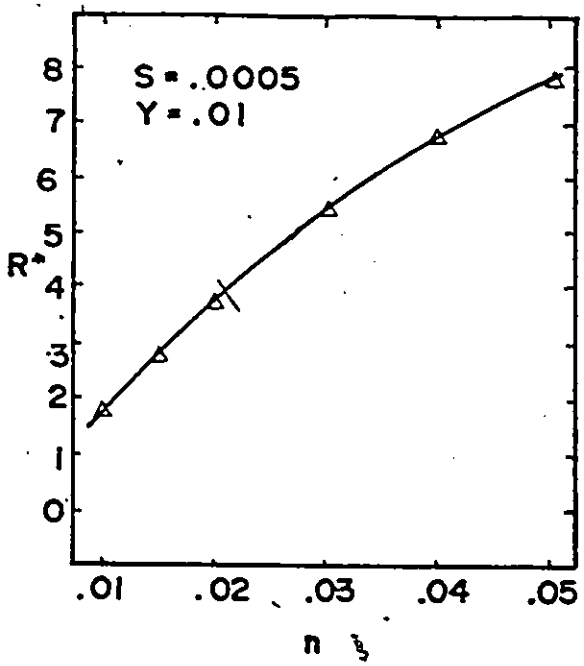

Fig. 2.22 Effect of Manning's Friction Coefficient on R* after Mozaneny and Song (10)

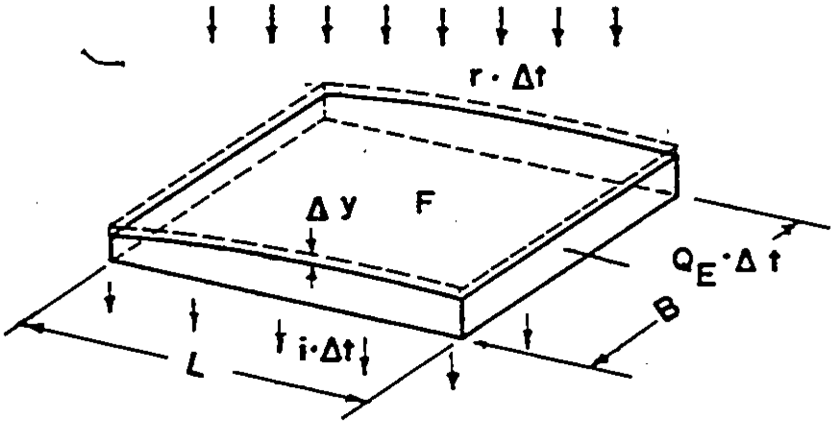

Fig. 2.23 Different Notations Used in the Continuity Equation for Surface Runoff after Dorsch (4)

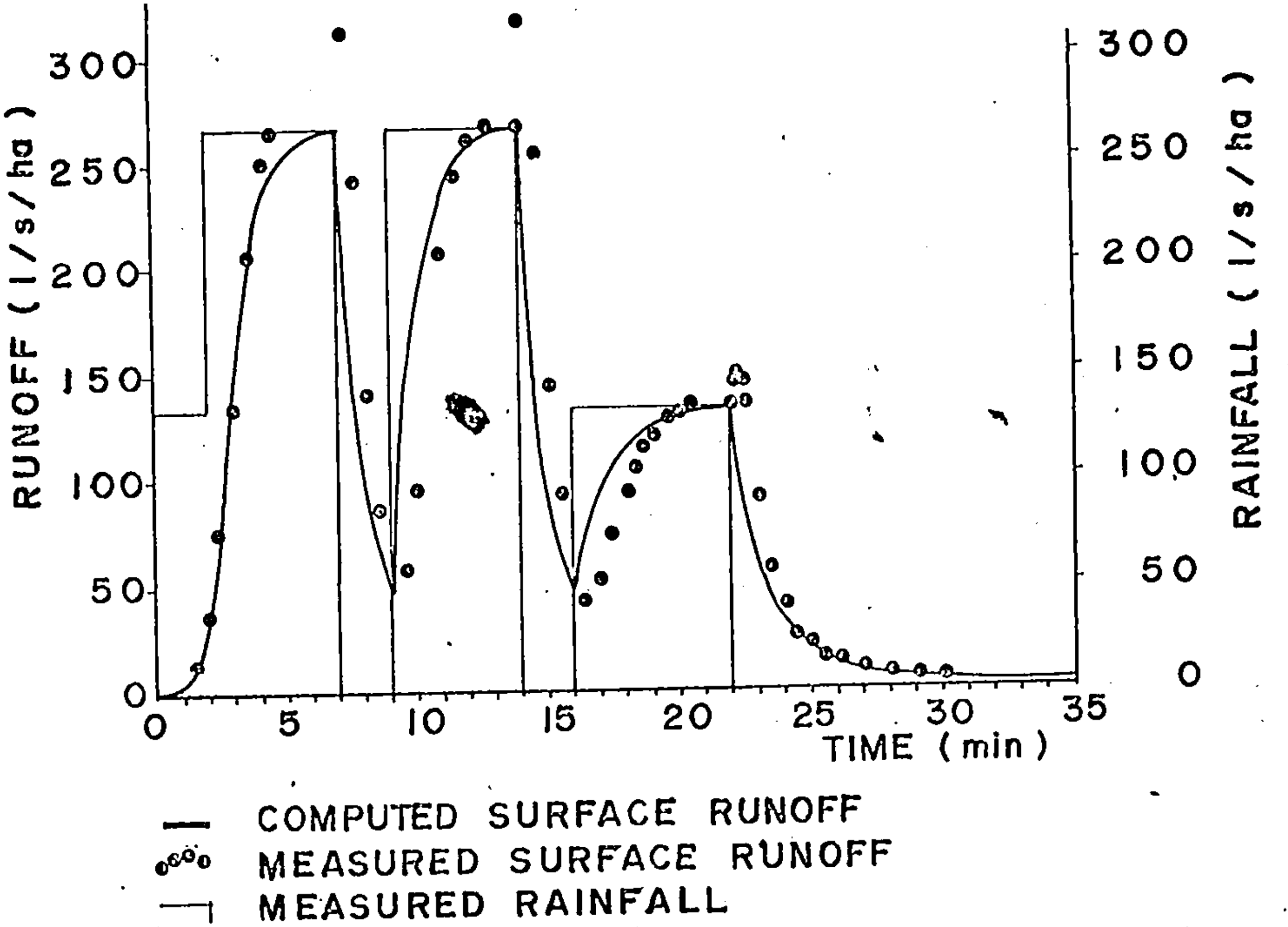

Fig. 2.24 Measurements from Izzard (1942) on an Asphalt Surface
Length: 22m, Slope: 0.005
after Dorsch (4)

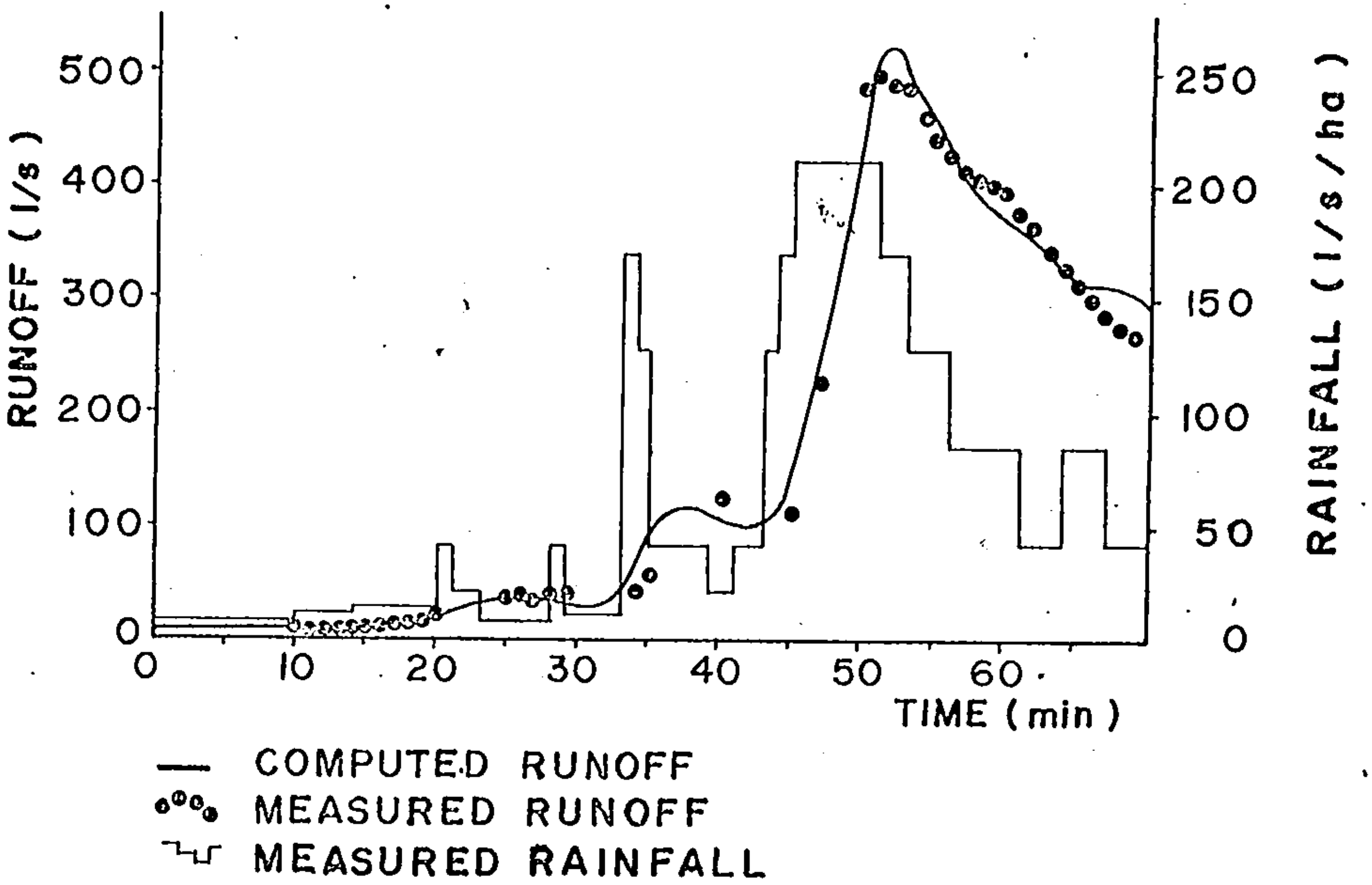

Fig. 2.25 Comparison Between the Calculation Method and the Measurements Obtained in Chicago, Illinois, Storm of 2.7.1966, Area: 5.228 ha after Dorsch (4)

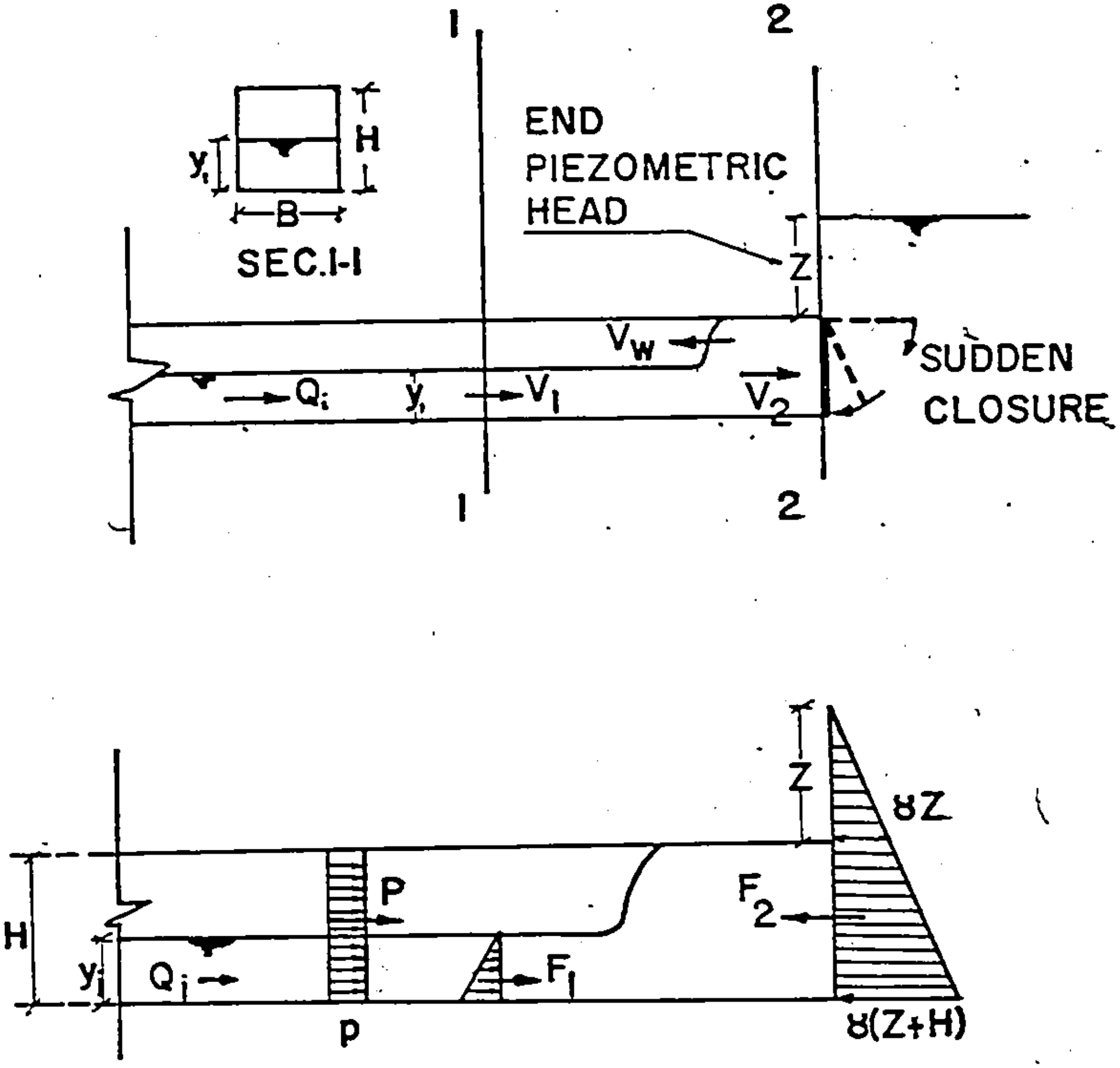

Fig. 3.1 A Positive Surge in the Storm Sewer Model

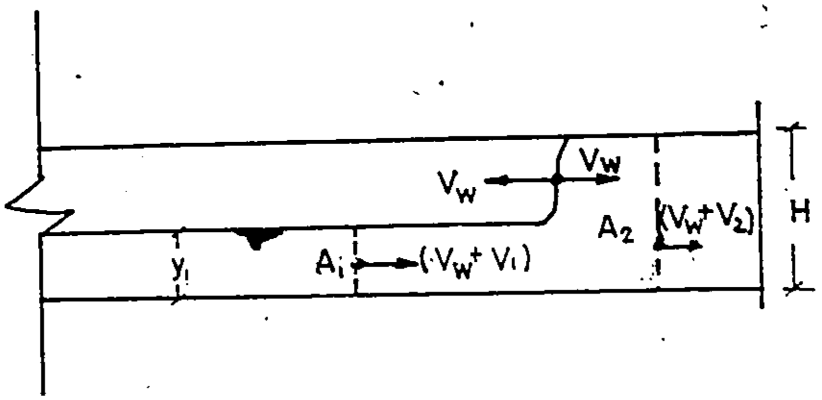

Fig. 3.2 View Appearing to the Observer Who Follows the Wavefront of the Positive Surge Forming in Storm Sewer Model

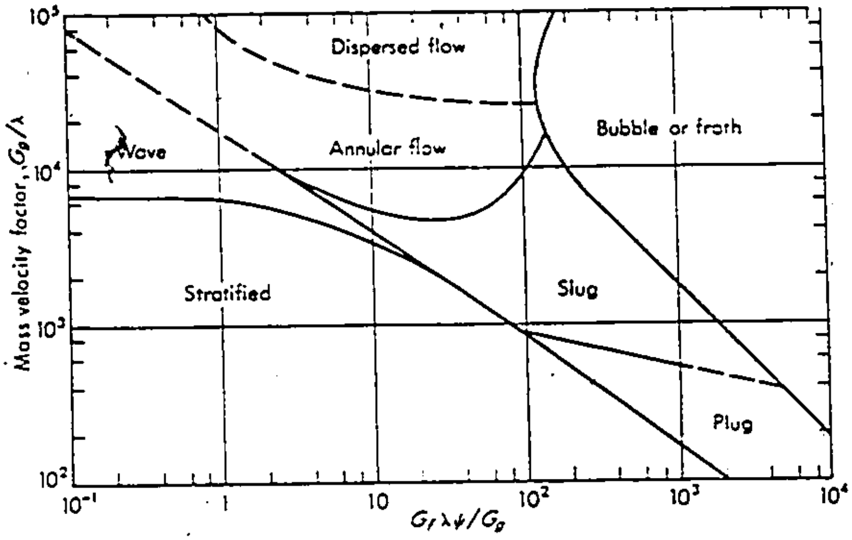

Fig. 3.3 Flow-Regime Correlations for Adiabatic Horizontal Two-Phase Two-Component Flow by Baker (1) (ρ_g and ρ_f in pounds per cubic feet, G_f and G_g in pounds per hour per square foot, σ in dynes/cm). $\lambda = [(\rho_g/0.075)(\rho_f/62.3)]^{1/2}$; $\psi = [(73/\sigma)]\ [\mu_f\ (62.3/\rho_f)^2]^{1/3}$.

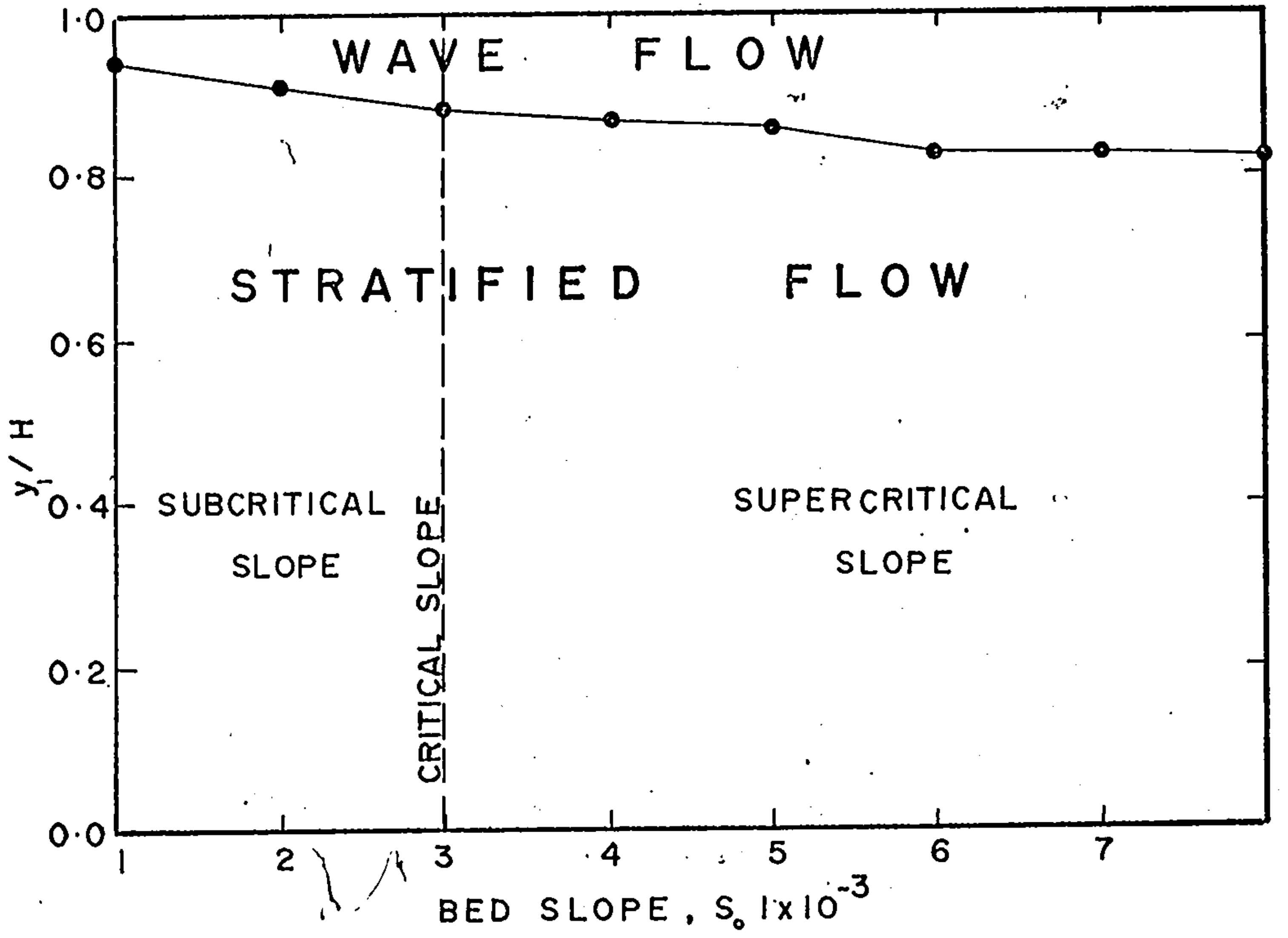

Fig. 3.4 Flow-Regime in the Storm Sewer Model According to Baker's Classification (1)

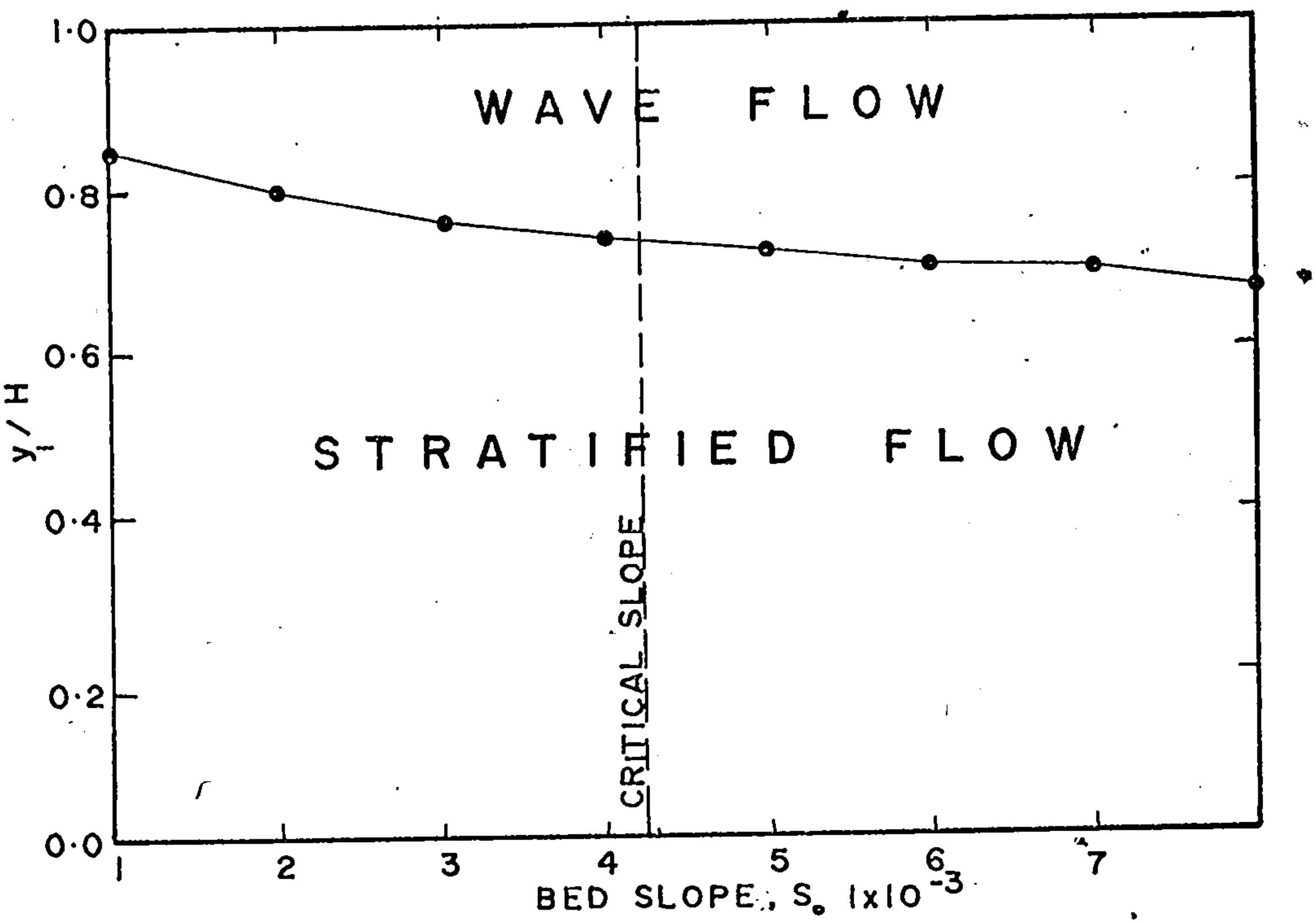

Fig. 3.5 Flow-Regime in A 10:1 Prototype Storm Sewer According to Baker's Classification (1)

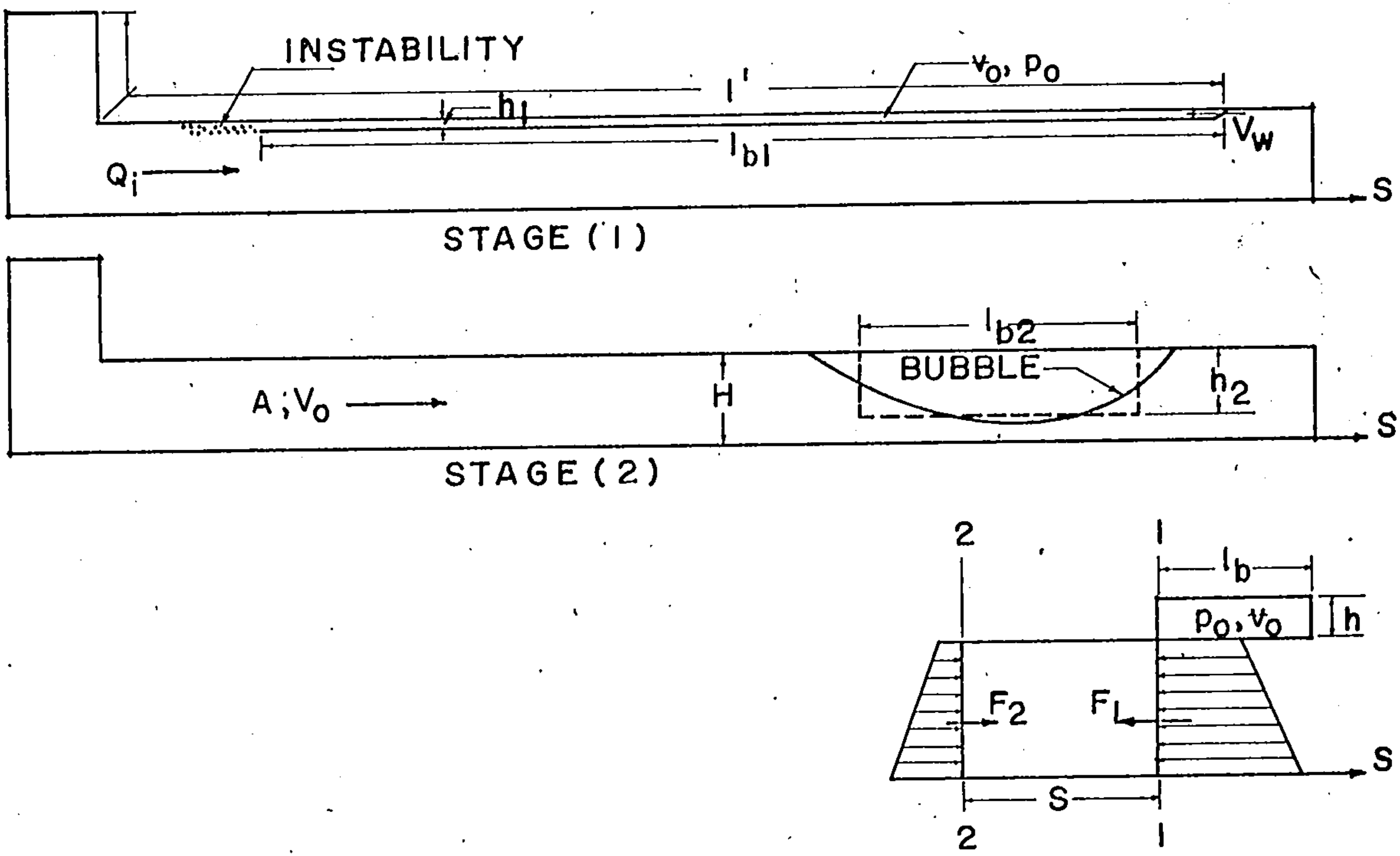

Fig. 3.6 Schematic Representation of Bubble Formation

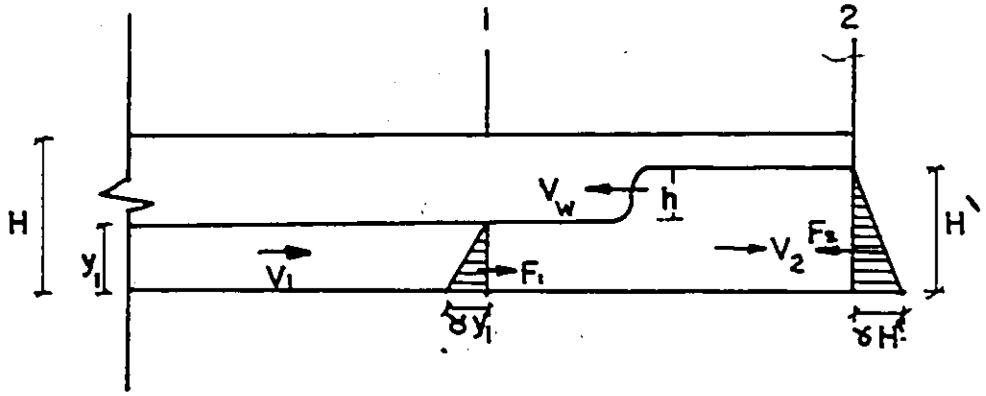

Fig. 3.7 Free Positive Surge in the Storm Sewer Model

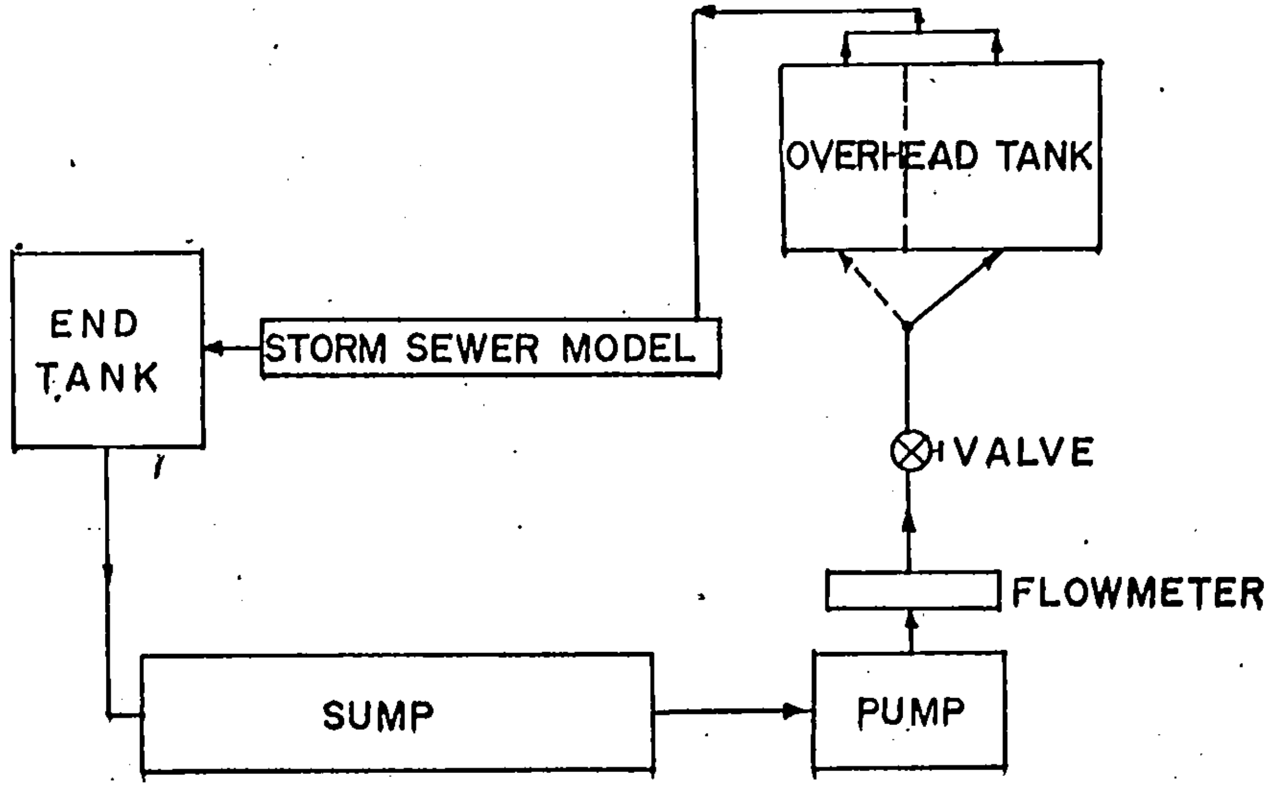

Fig. 4.1 General Layout of the Experimental Equipment

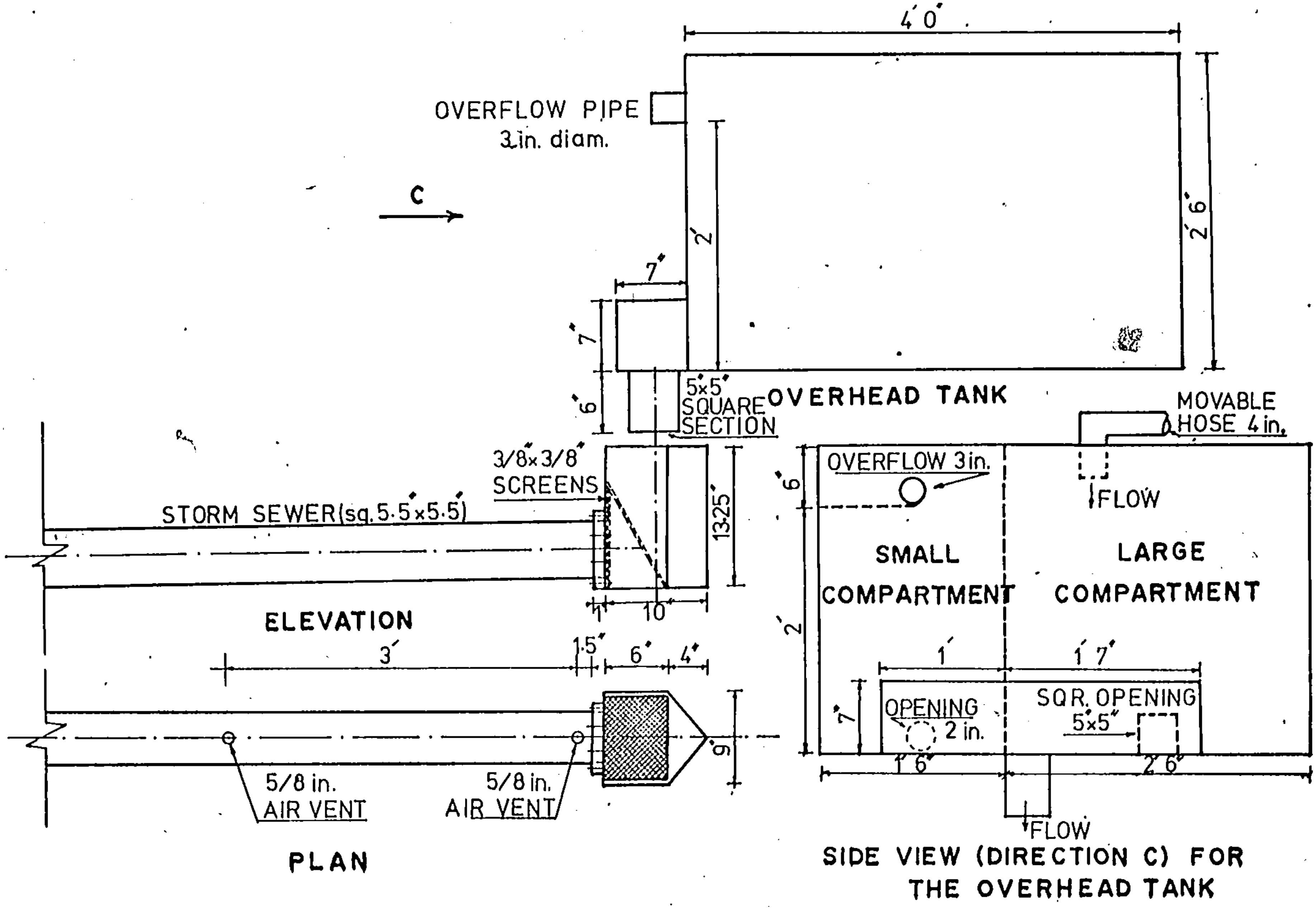

Fig. 4.2 Details of Overhead Tank with the Upstream End of the Storm Sewer Model

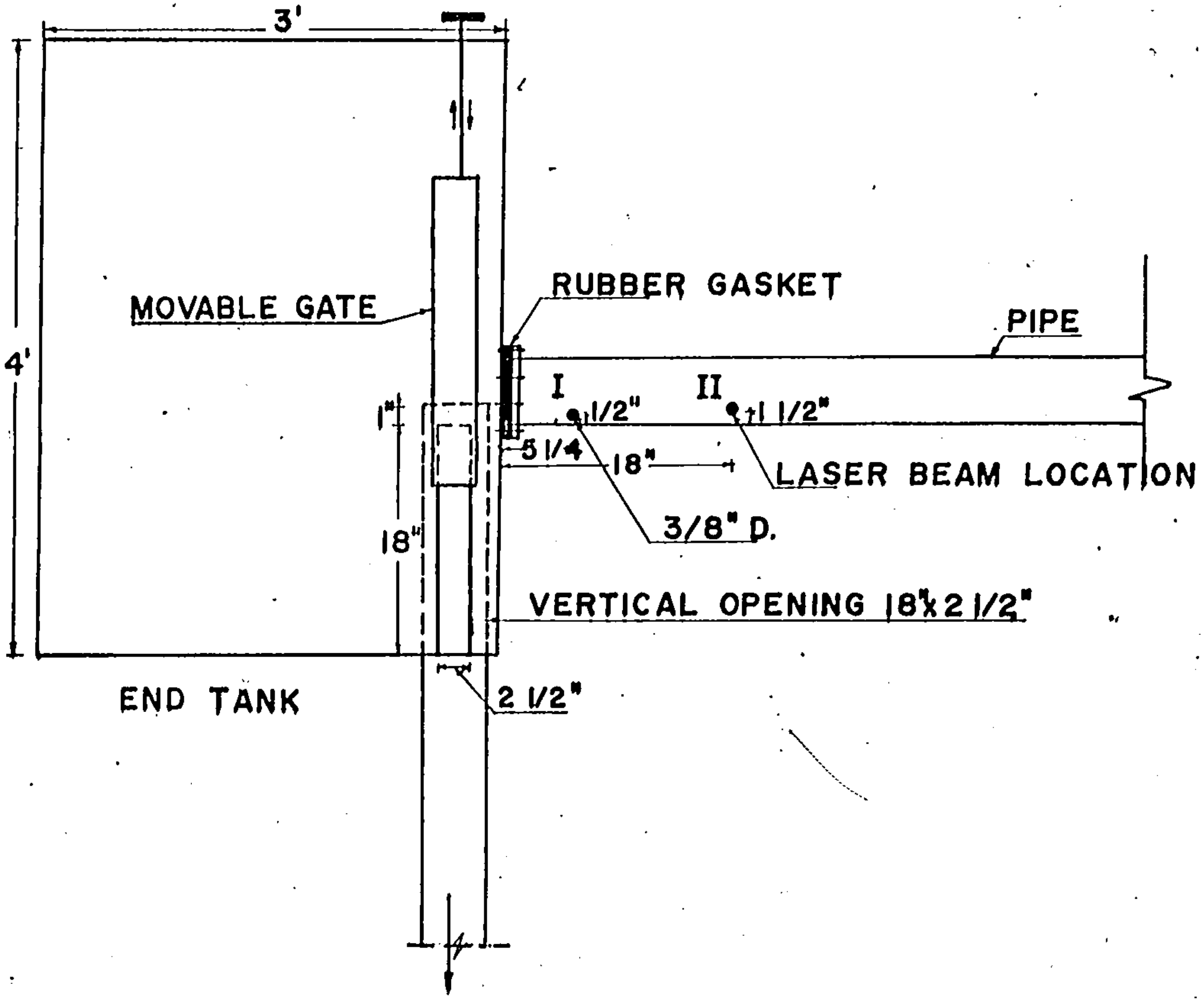

Fig. 4.3 Details of End Tank with Downstream End of Storm Sewer Model

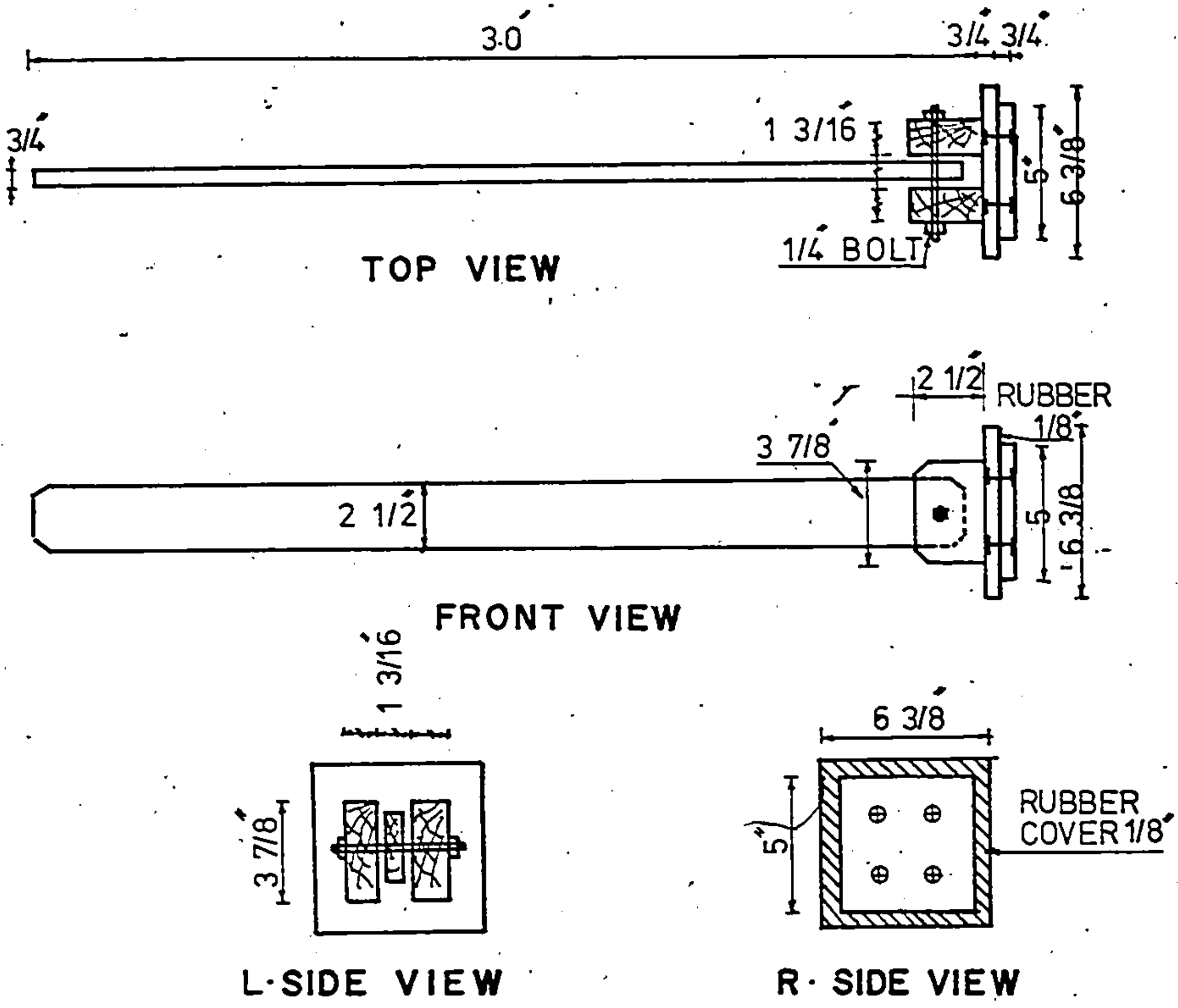

Fig. 4.4 Details of Manual Closure Arm

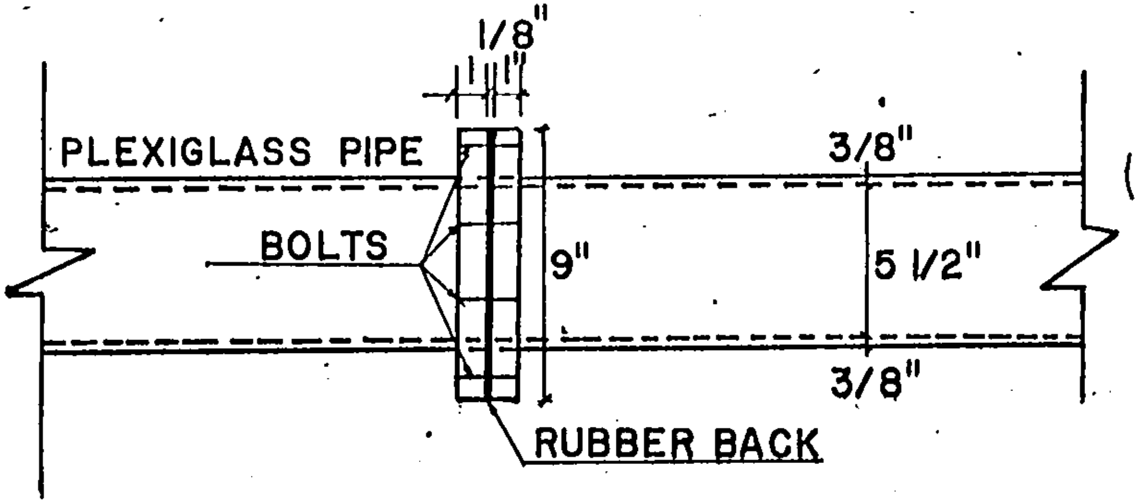

Fig. 4.5 Detail of Joints Between Pipe Sections

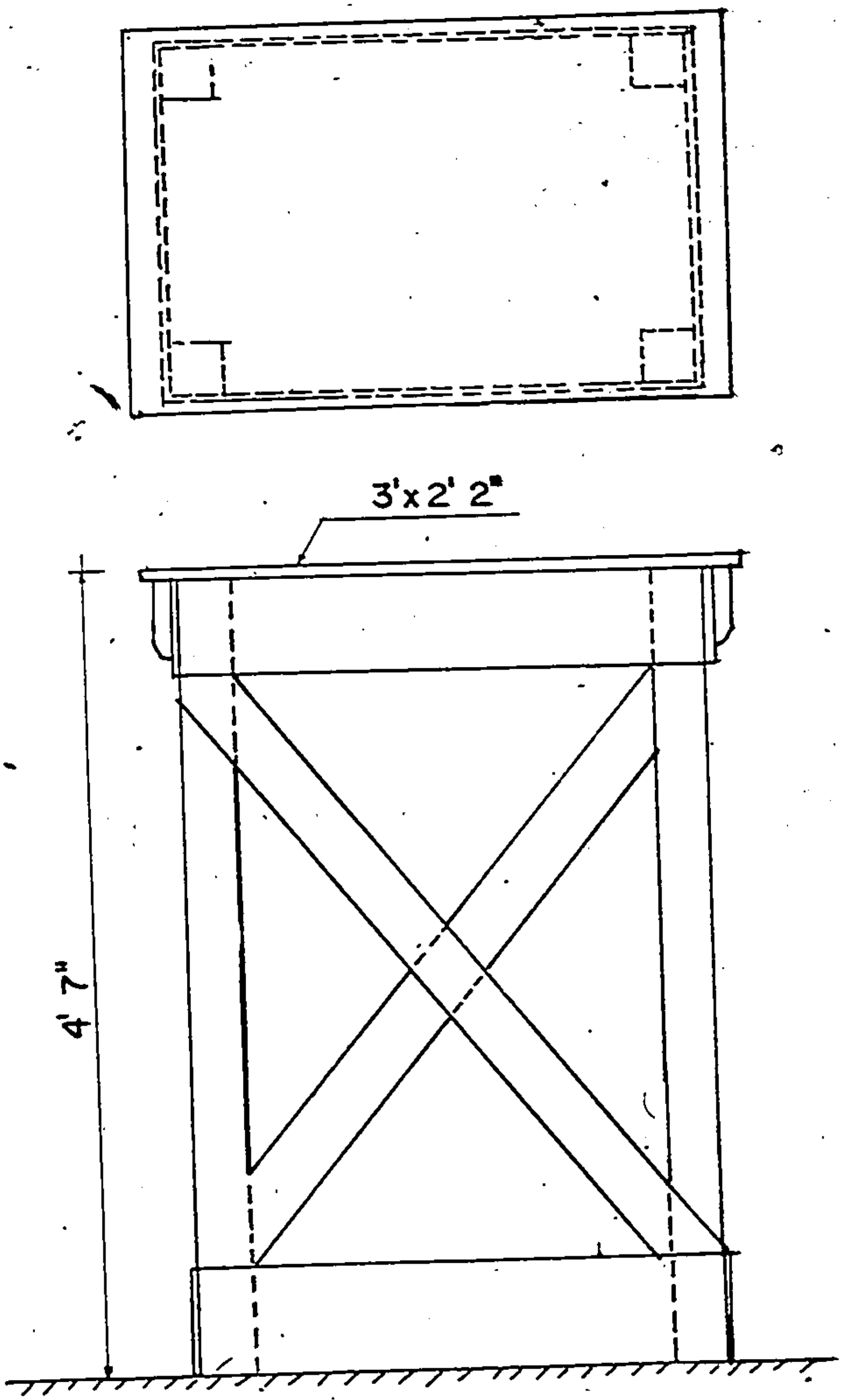

Fig. 4.6 Downstream Tank Support

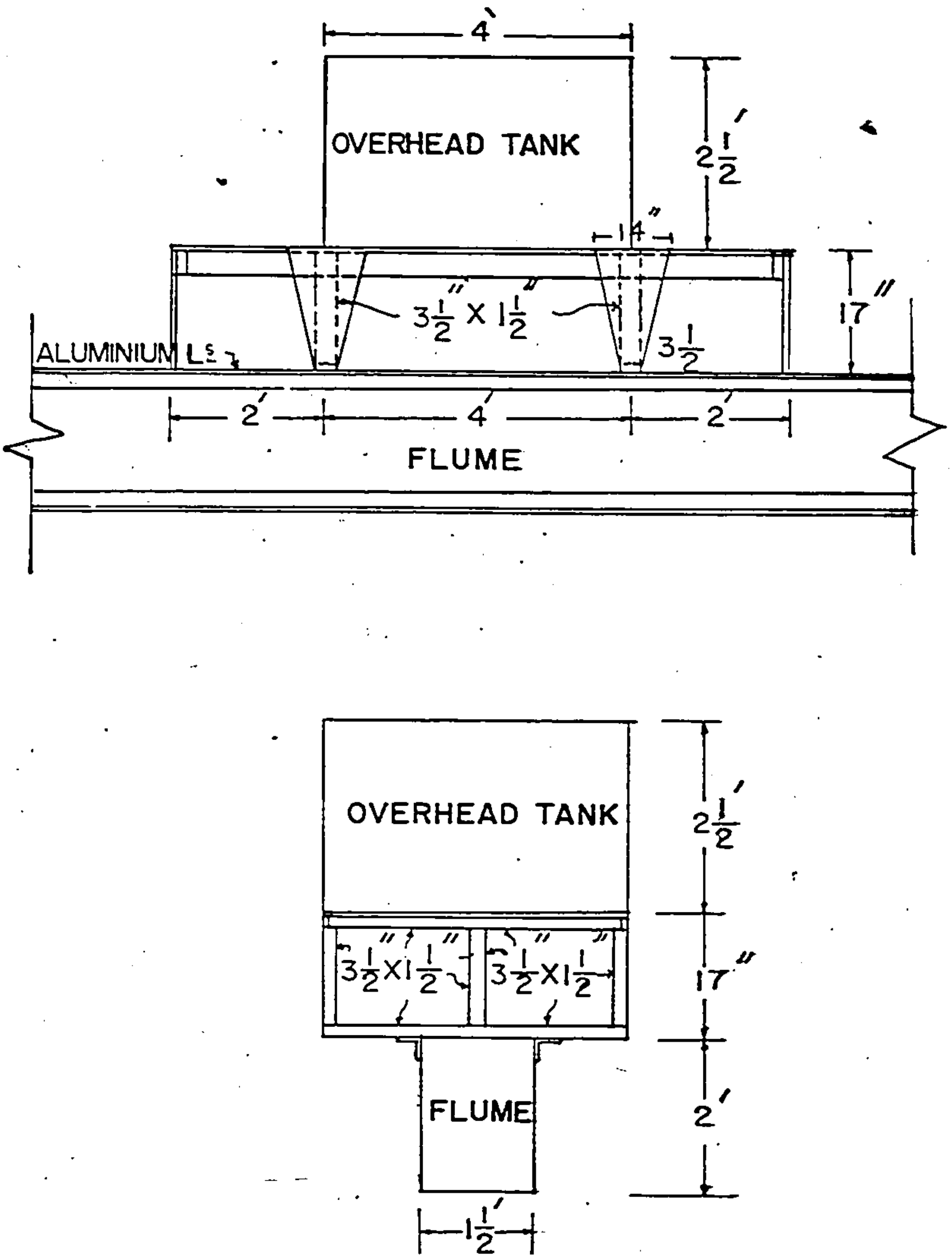

Fig. 4.7 Details of Platform Supporting the Overhead Tank

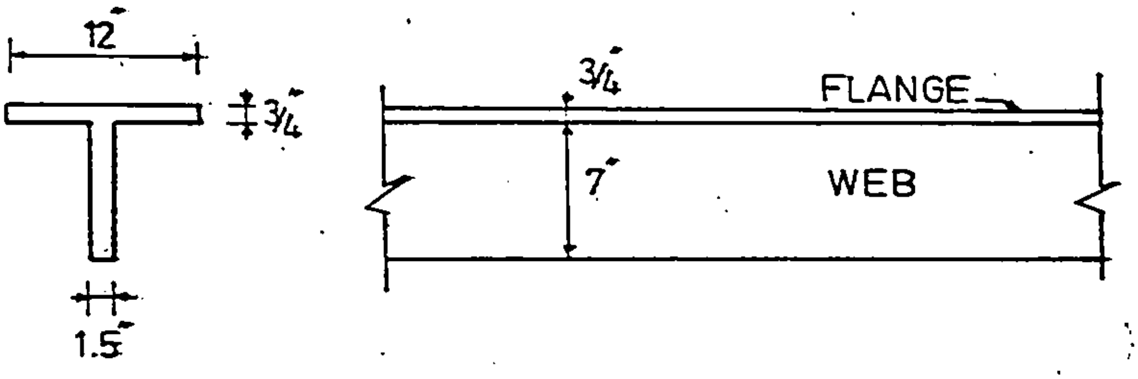

CROSS-SECTION

T-SECTION BEAM

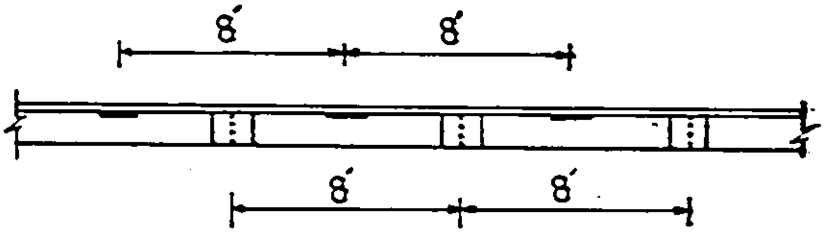

GENERAL ARRANGEMENT OF SPLICES

Fig. 4.8 Details for the Continuous T-Section Beam Carrying the Plexiglass Pipe

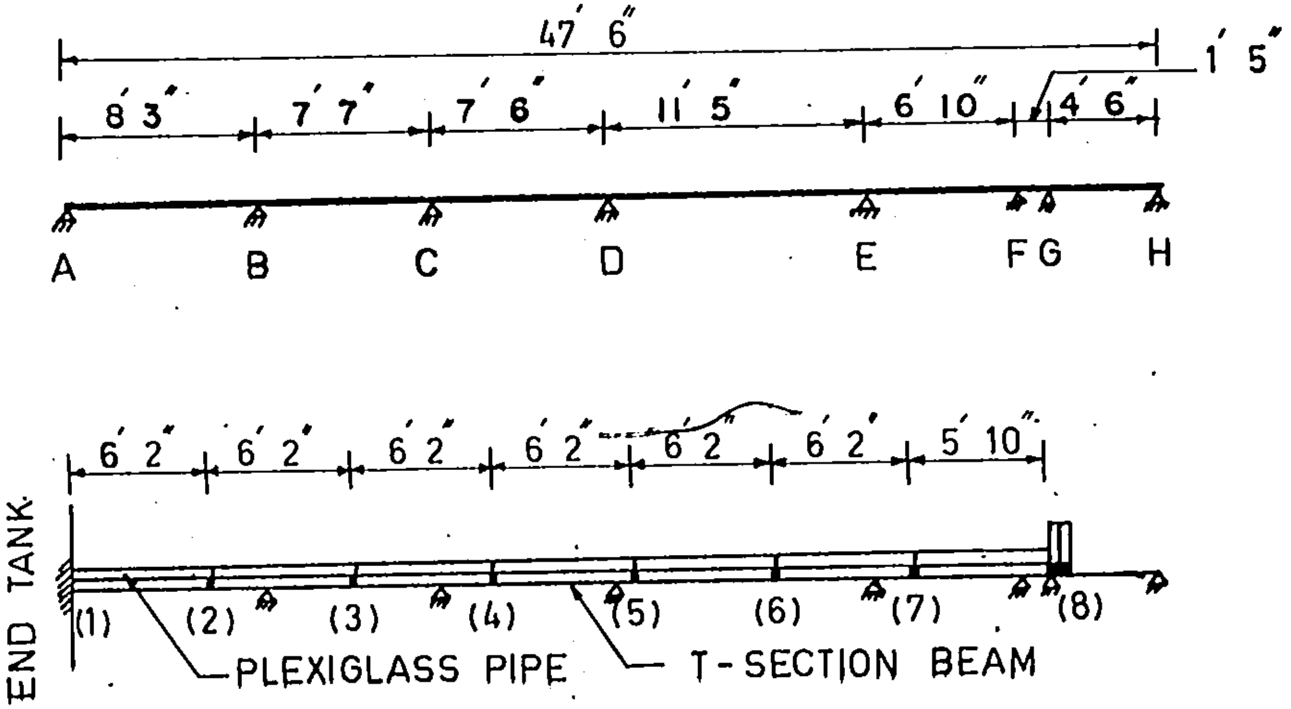

Fig. 4.9 Points of Support of the Pipe

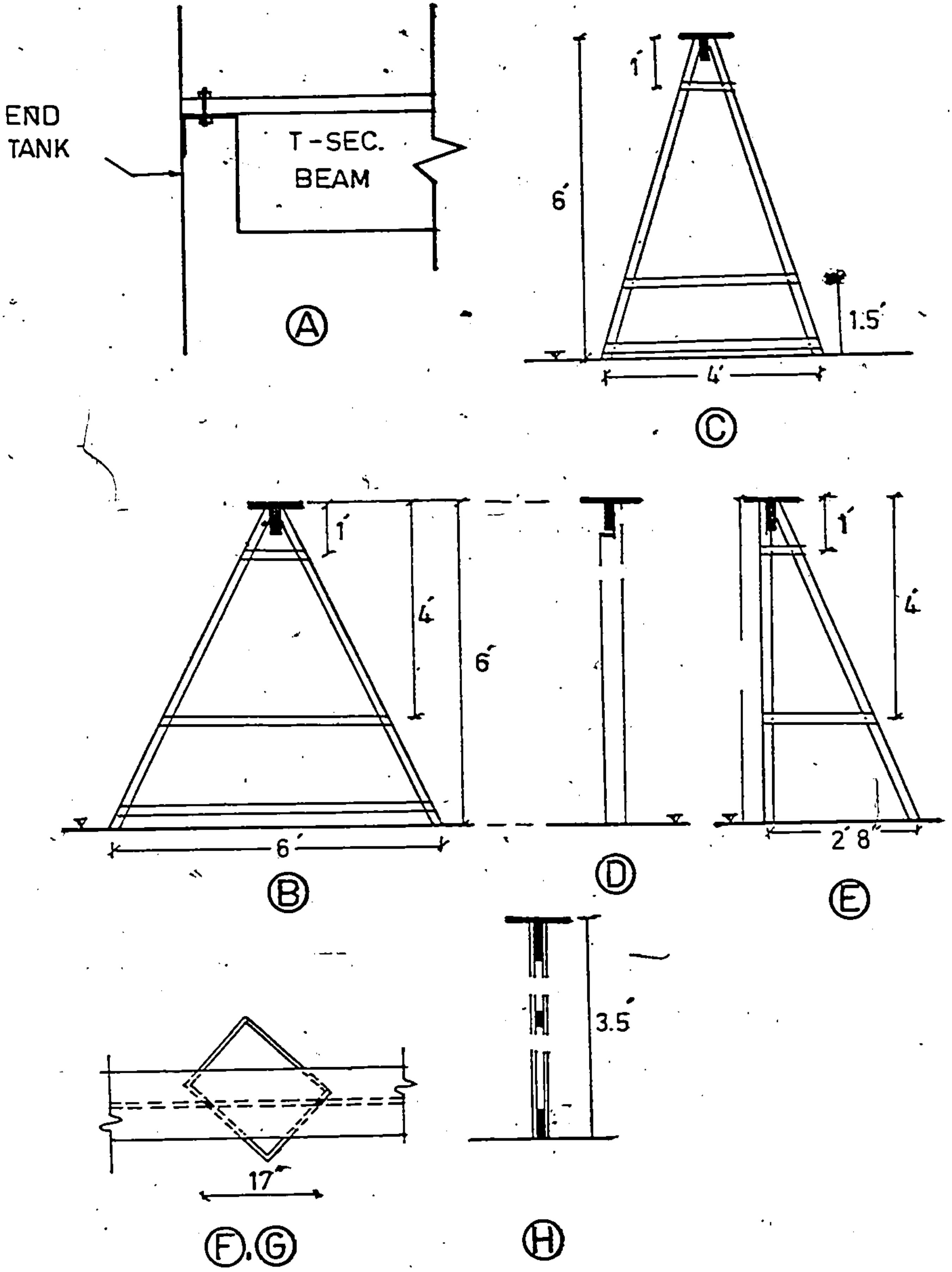

Fig. 4.10 Details for T-Section Supports

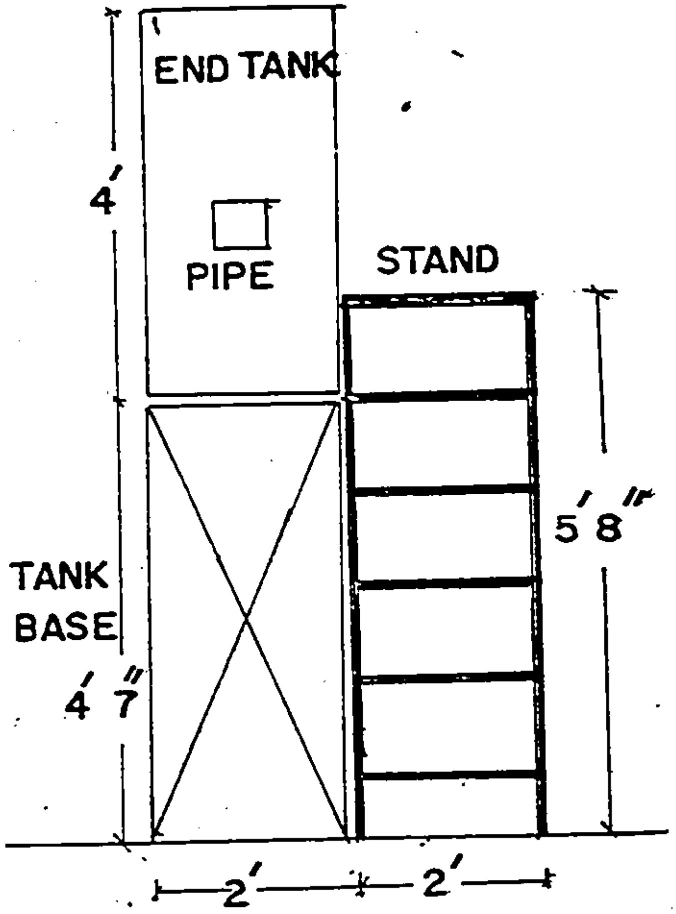

Fig. 4.11 Stand for Manual Closure

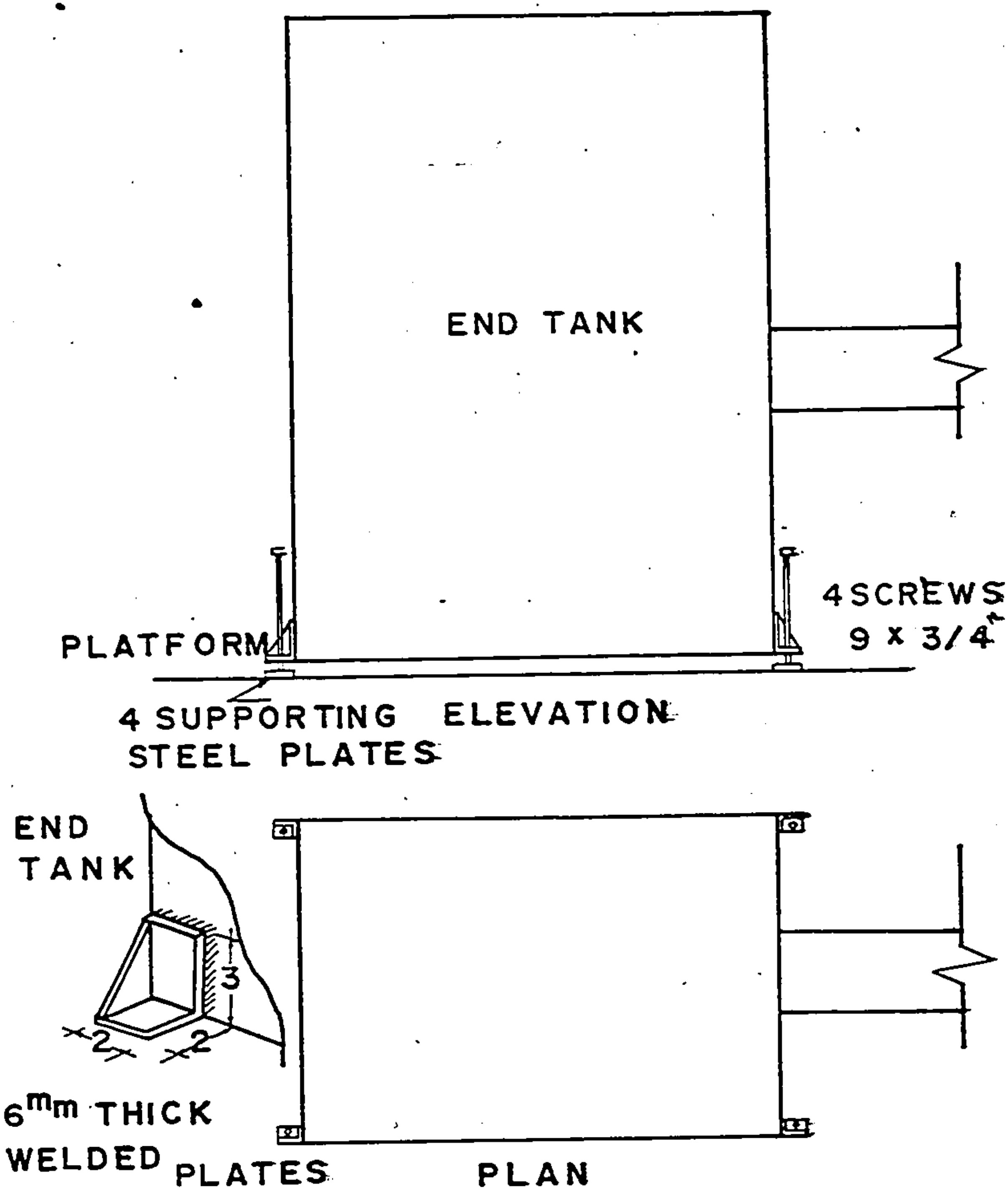

Fig. 4.12 Mechanism Used for Elevation Adjustment for End Tank

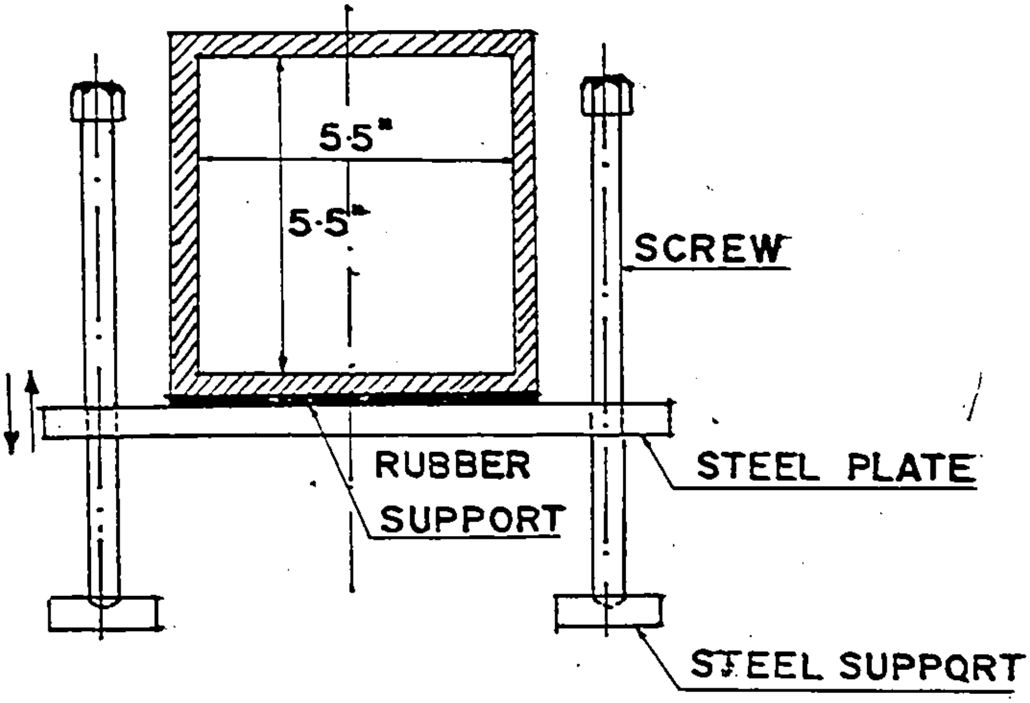

Fig. 4.13 Mechanism Used for Slope Adjustment

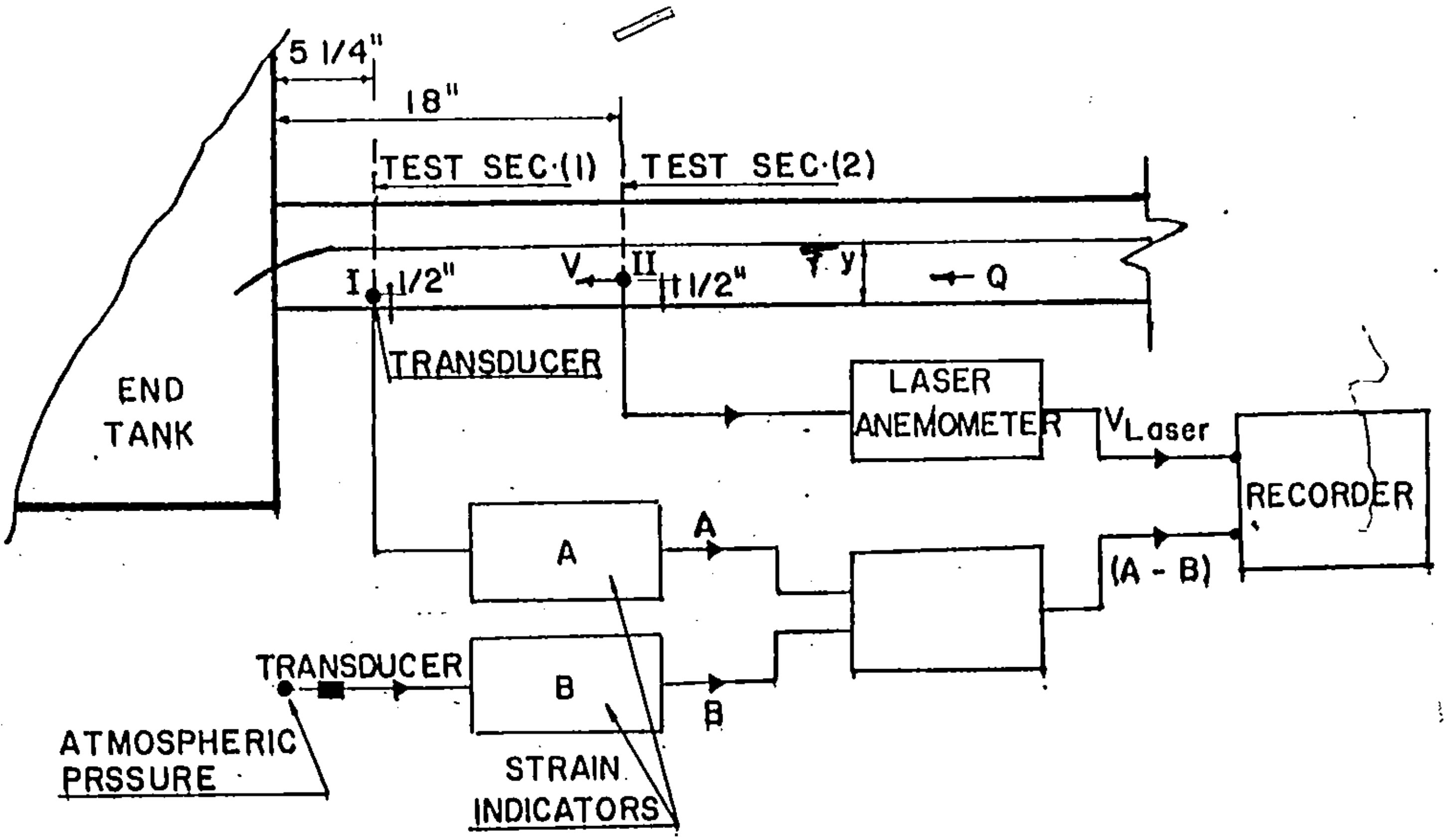

Fig. 4.14 Recording the Velocity and the Depth of Flow

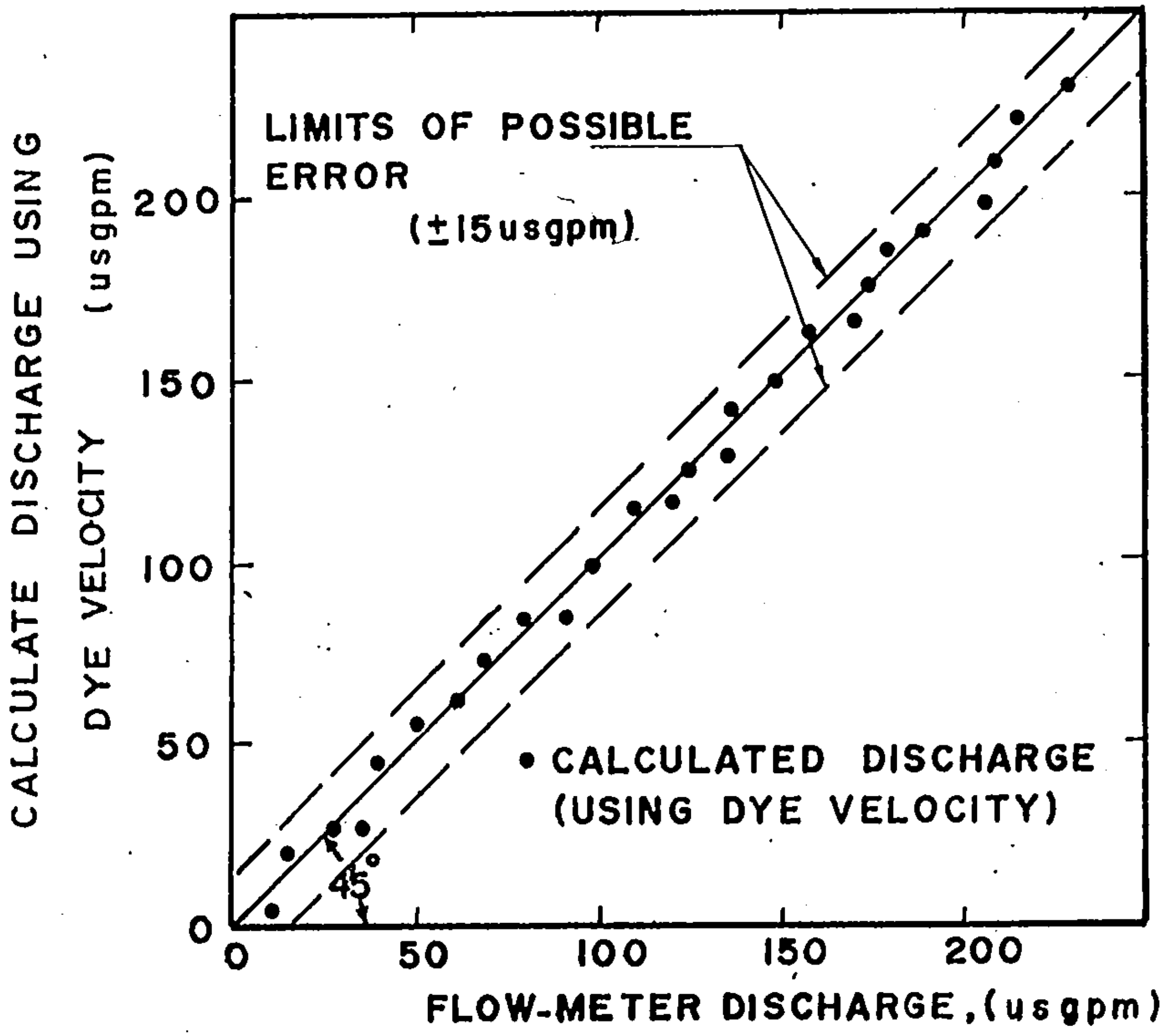

Fig. 4.15 Calibration of Flow Meter (for Critical Slope S_o = 0.0033)

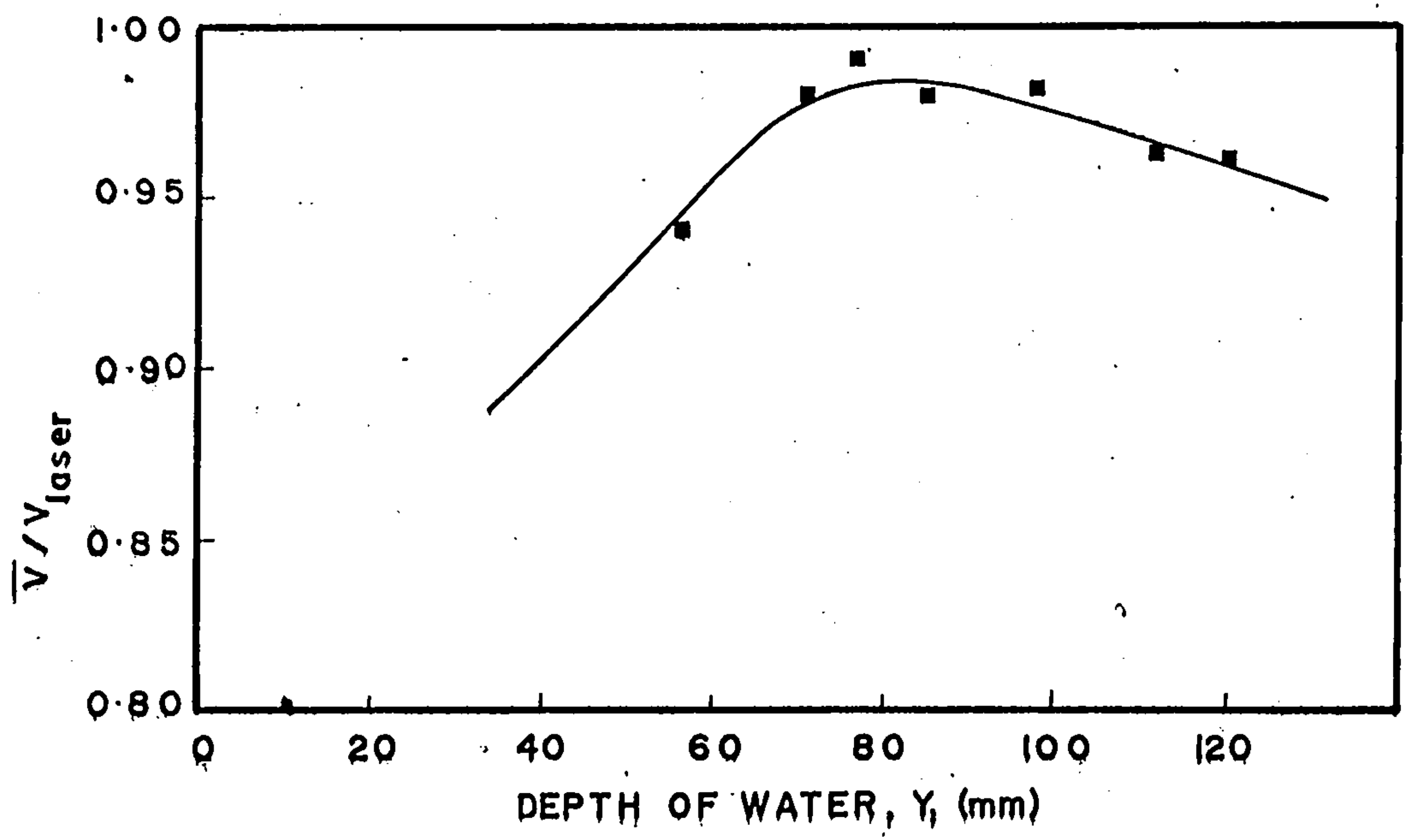

Fig. 4.16 Laser Velocity Correction Factor for Different Flow Depths

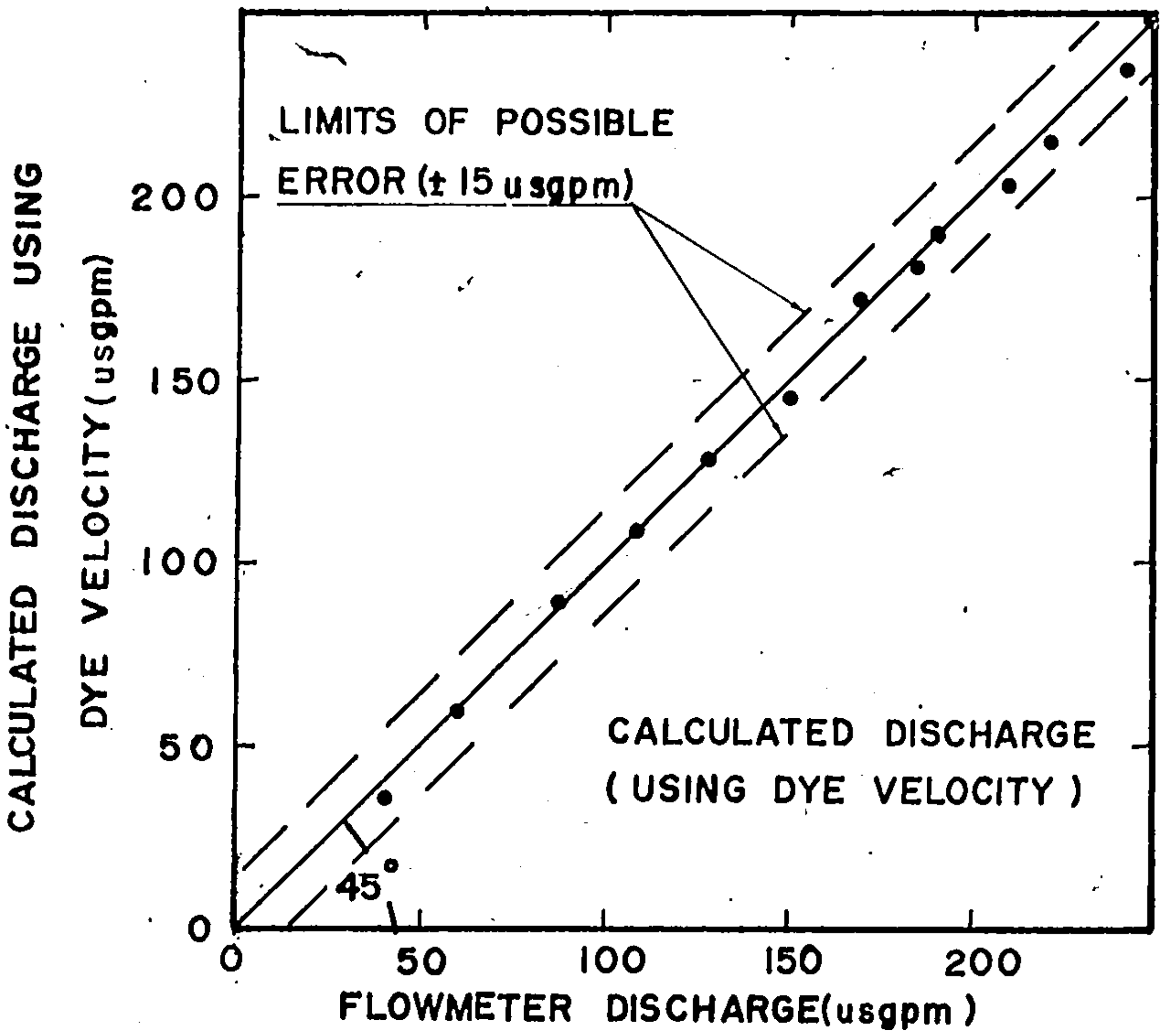

Fig. 4.17 Calibration of Flow Meter (for Supercritical Slope $S_o = 0.0061$)

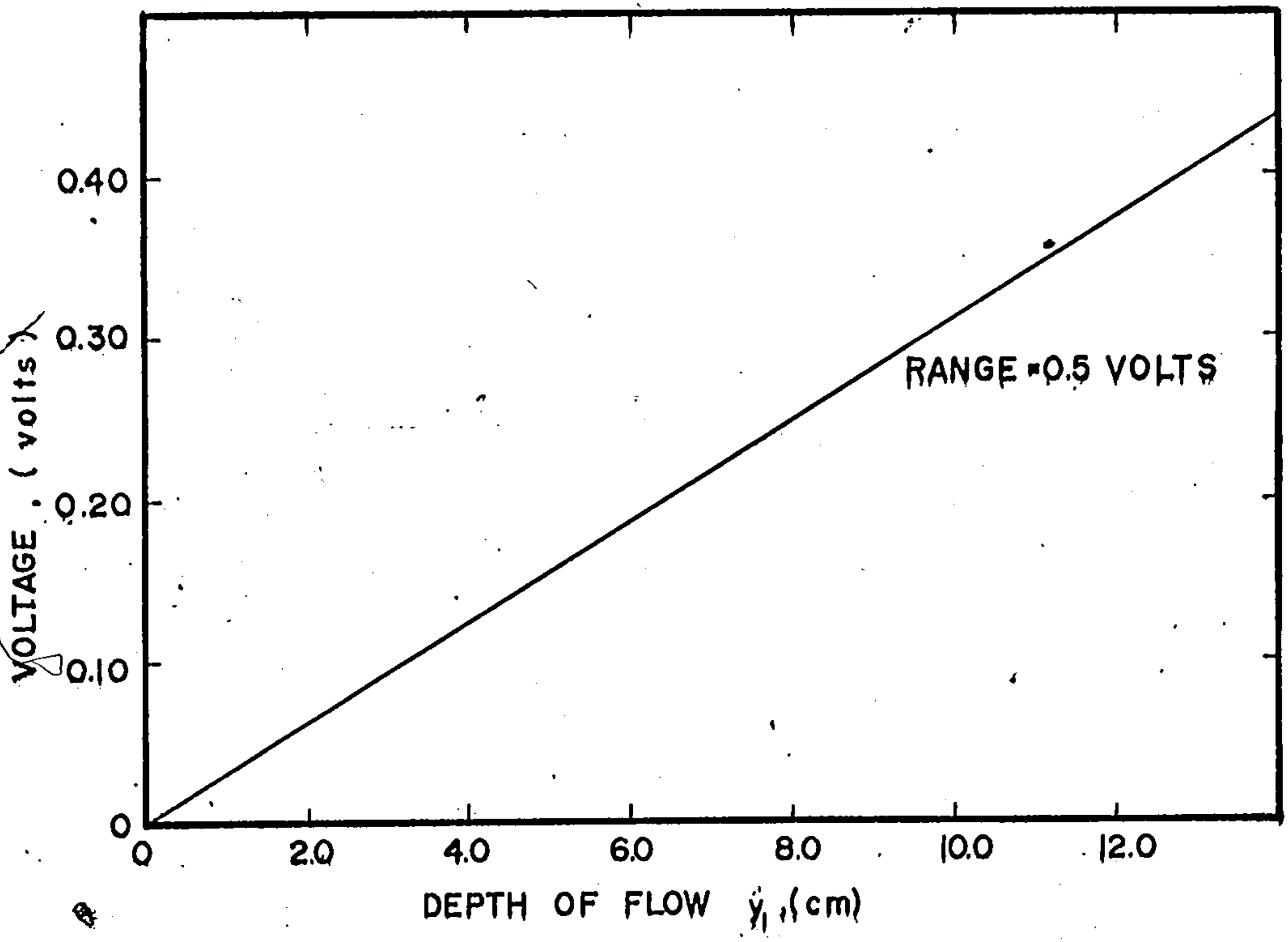

Fig, 4.18 Calibration of Strain Indicator Readings

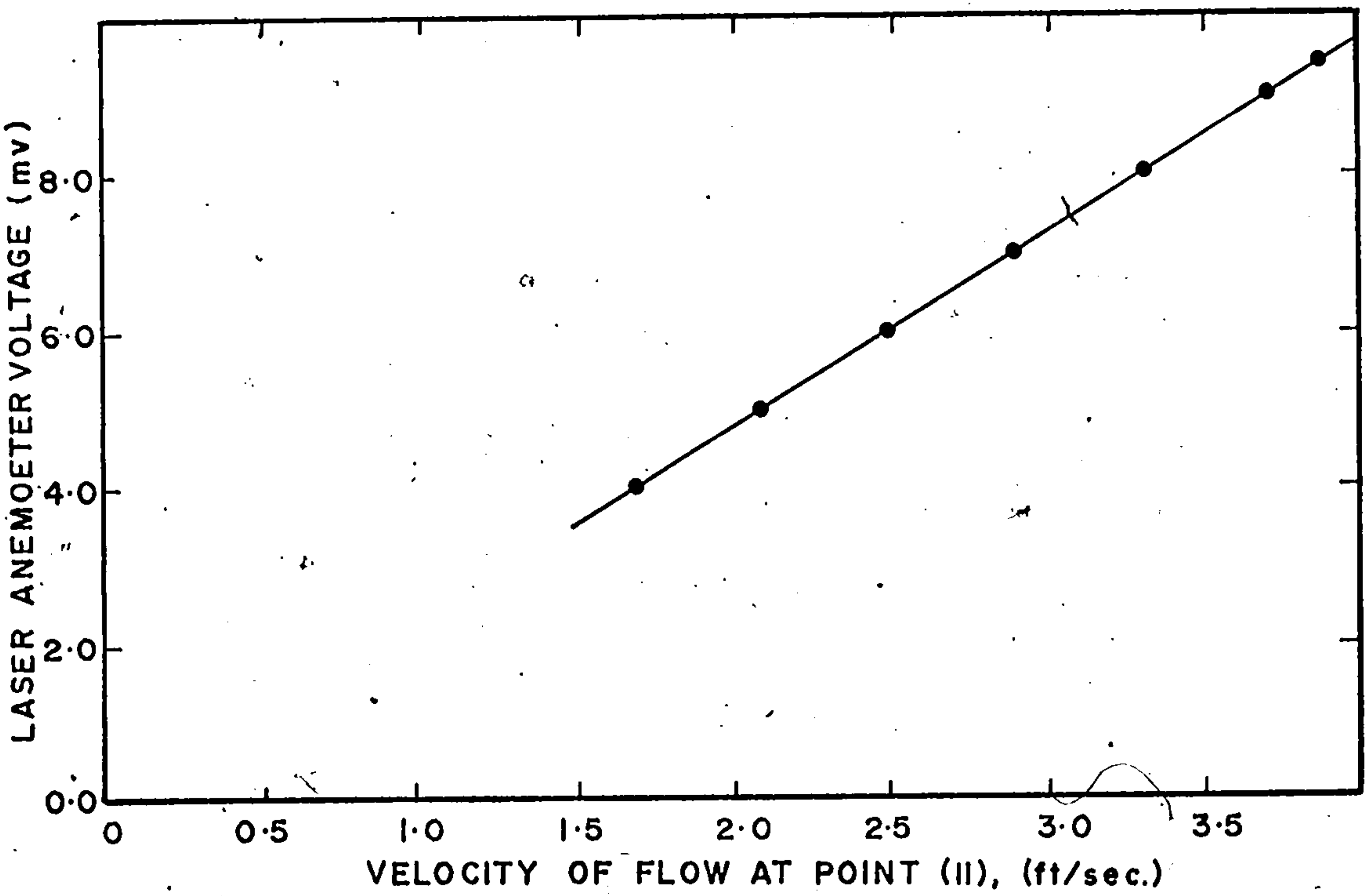

Fig. 4.19 Calibration of Laser Anemometer Readings

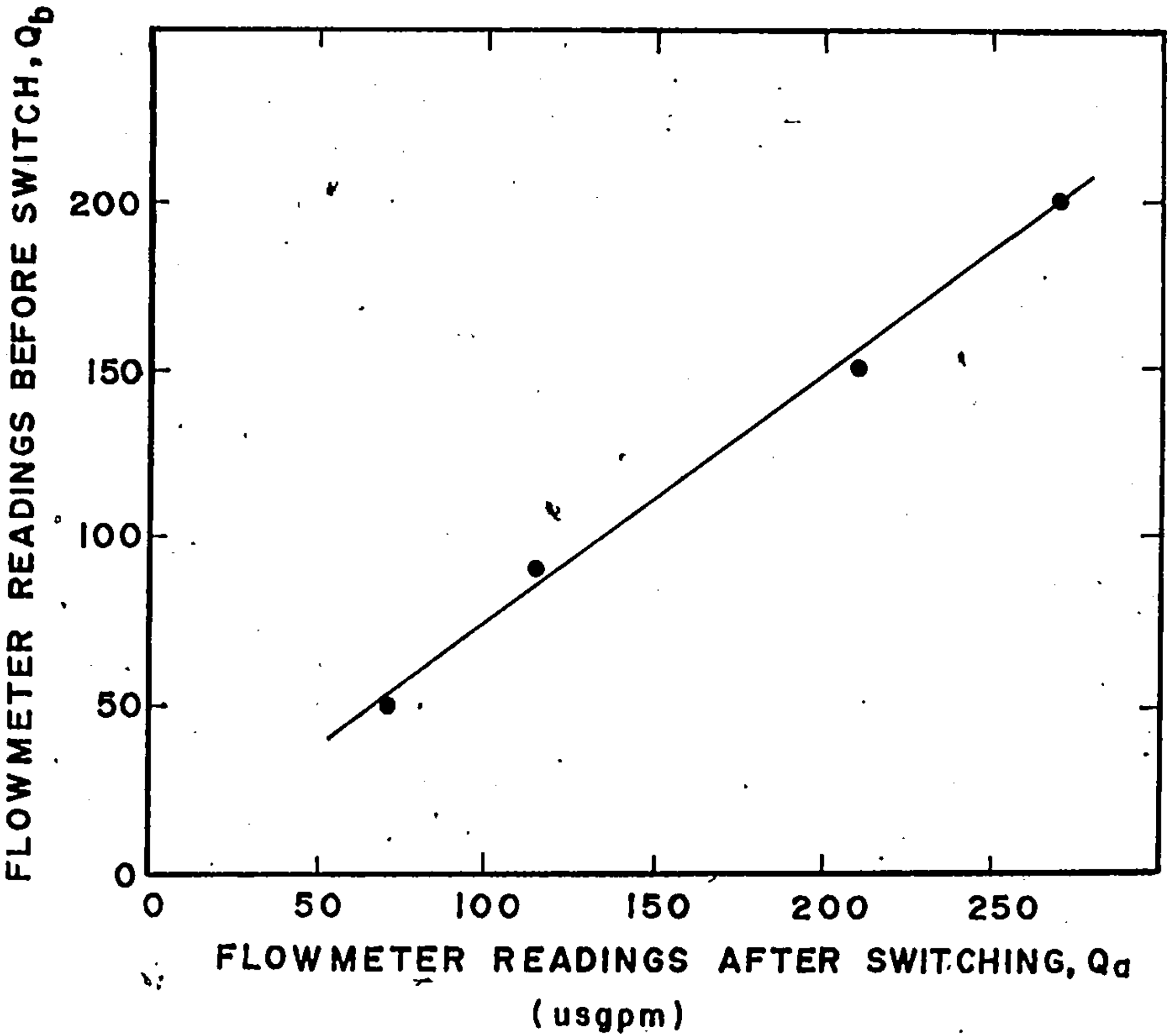

Fig. 4.20 The Effect of Hose Buckling on the Flow Meter Readings

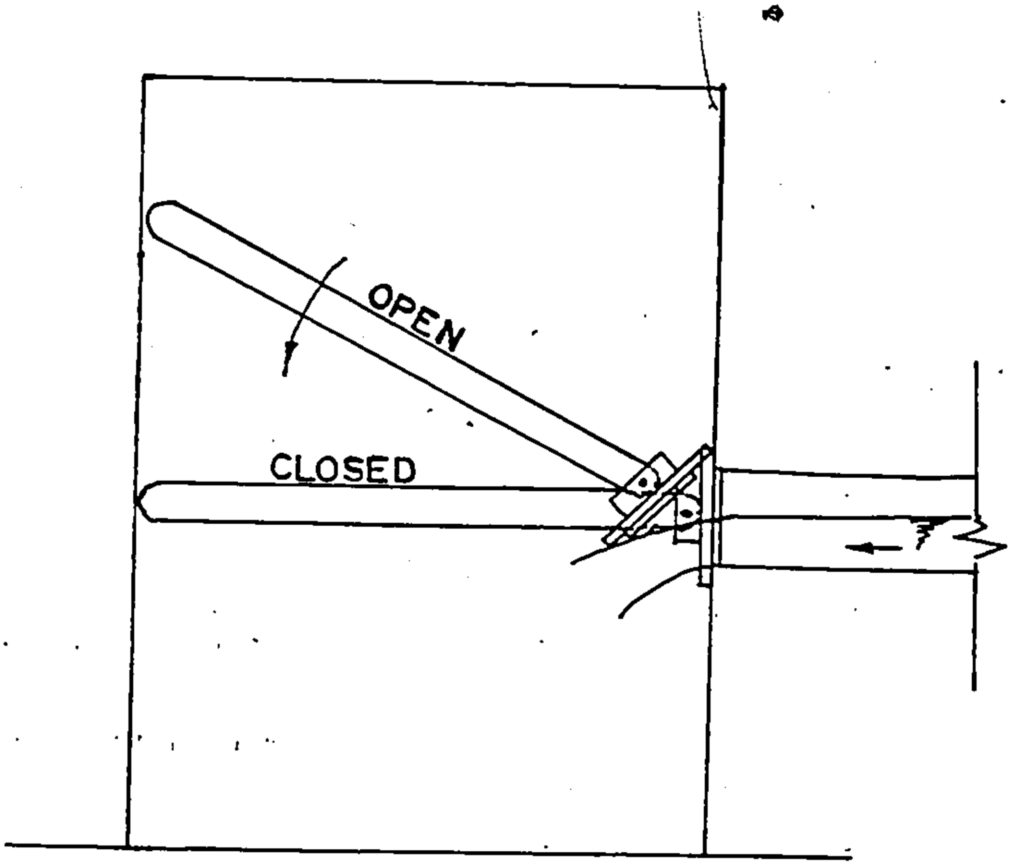

Fig. 4.21 Mechanics of Closing the Downstream End of the Pipe

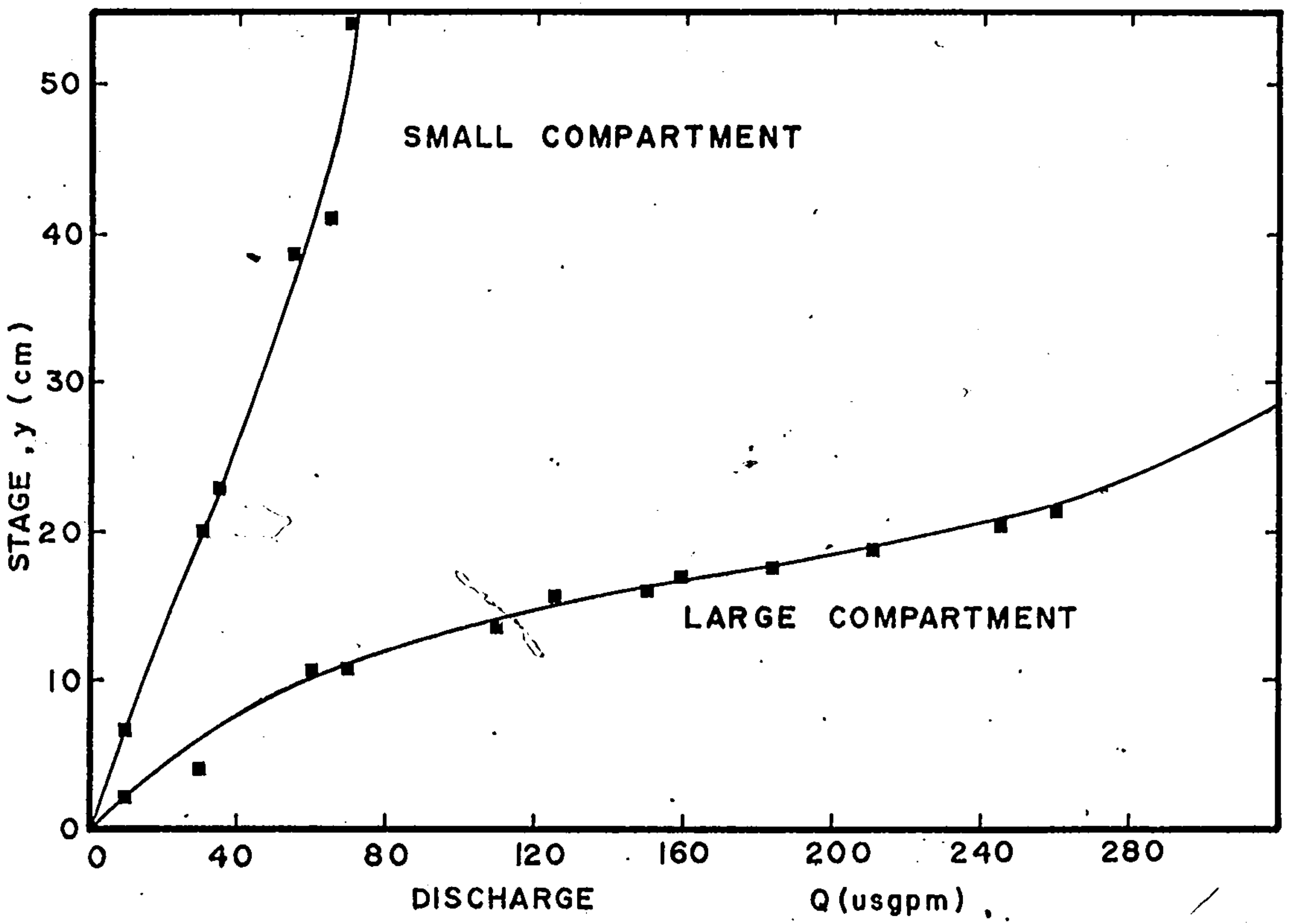

Fig. 4.22 Stage-Discharge Curves for the Small and Big Compartments of the Overhead Tank

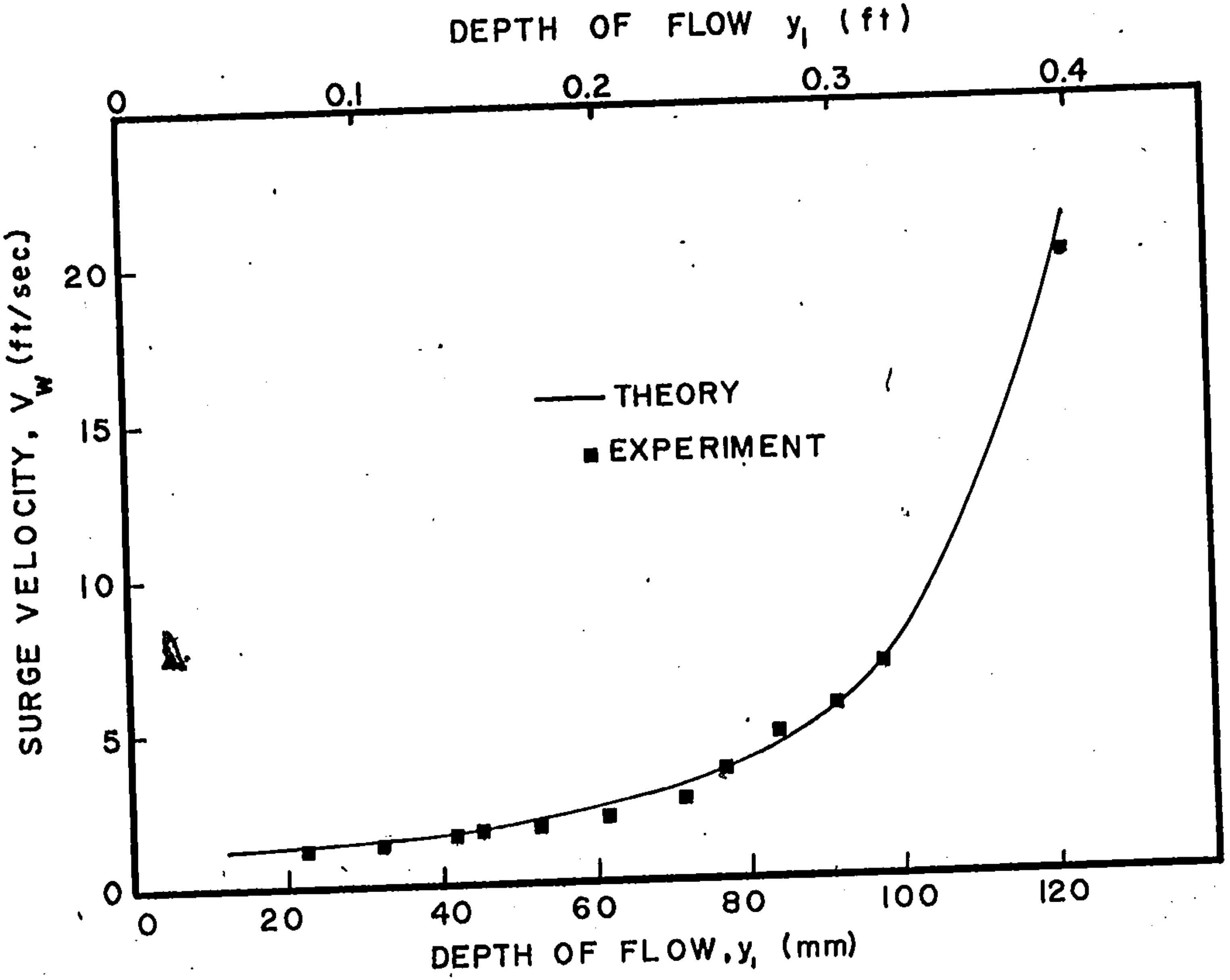

Fig. 4.23 The Theoretical and Experimental Surge Velocity for Different Flow Depths (S_o = .0033)

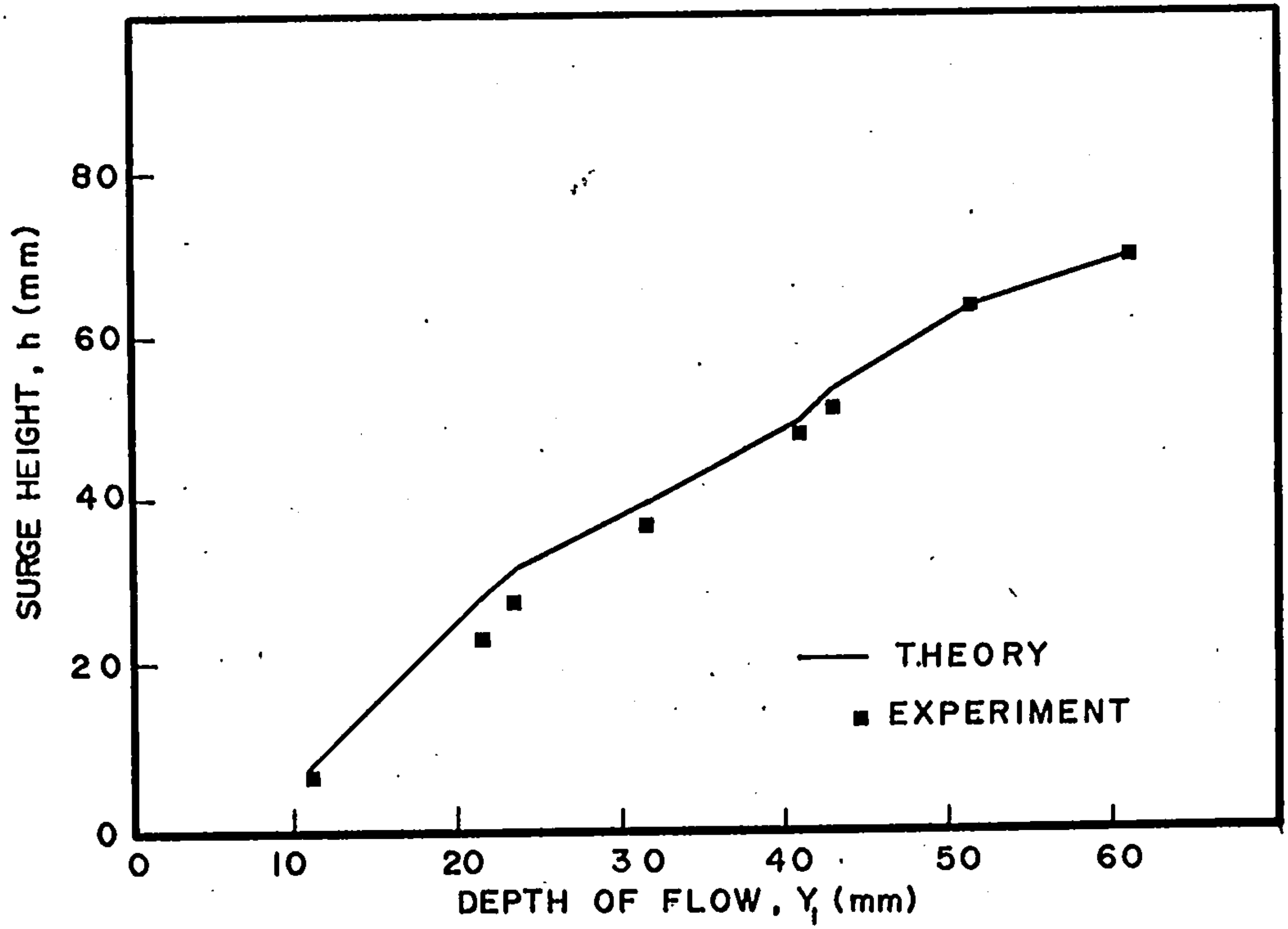

Fig. 4.24 The Theoretical and Experimental Surge Height for Different Flow Depths (S_o = 0.0033)

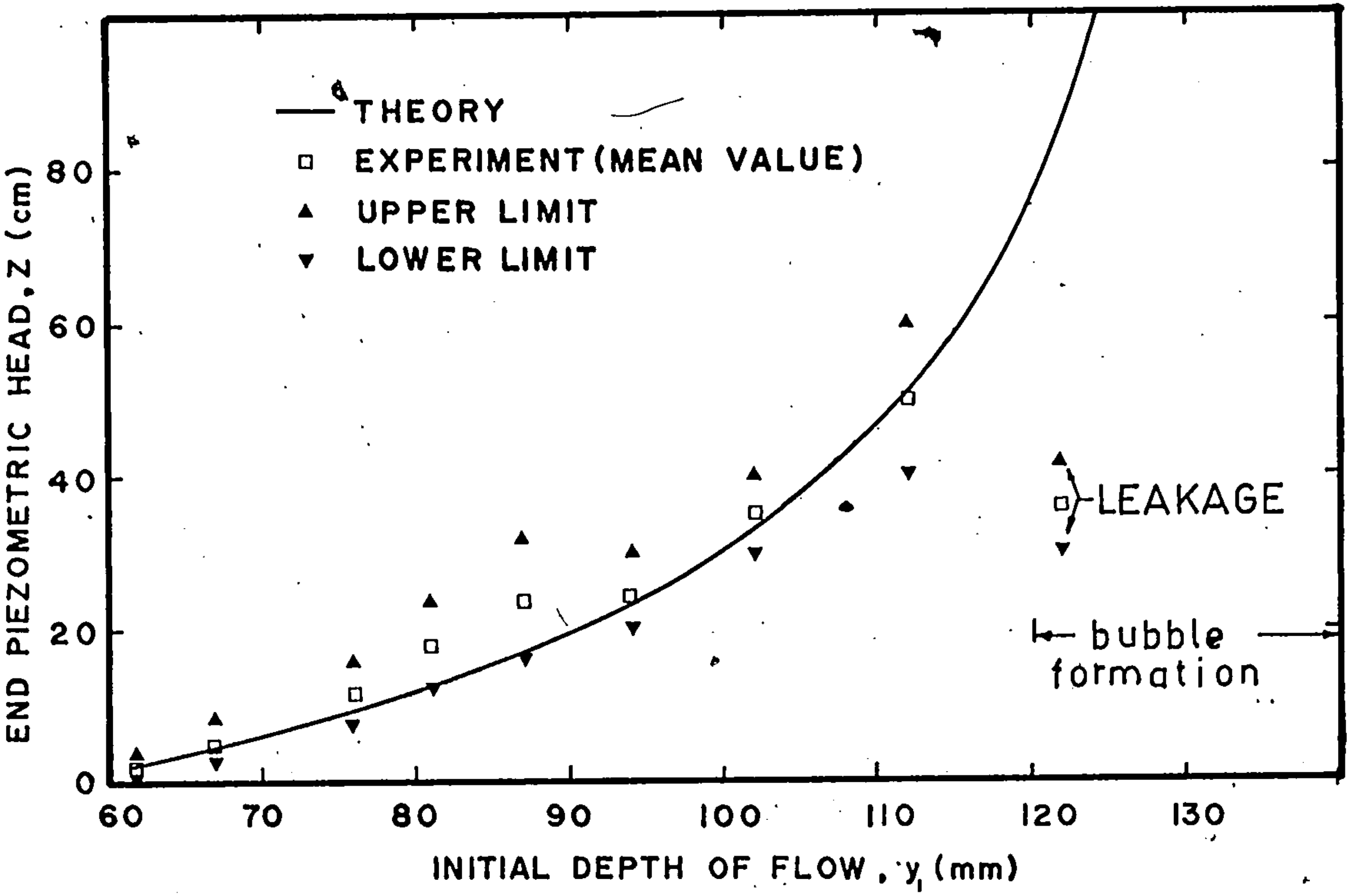

Fig. 4.25 The Theoretical and Experimental Piezometric Head for Different Flow Depths (S_o = 0.0033)

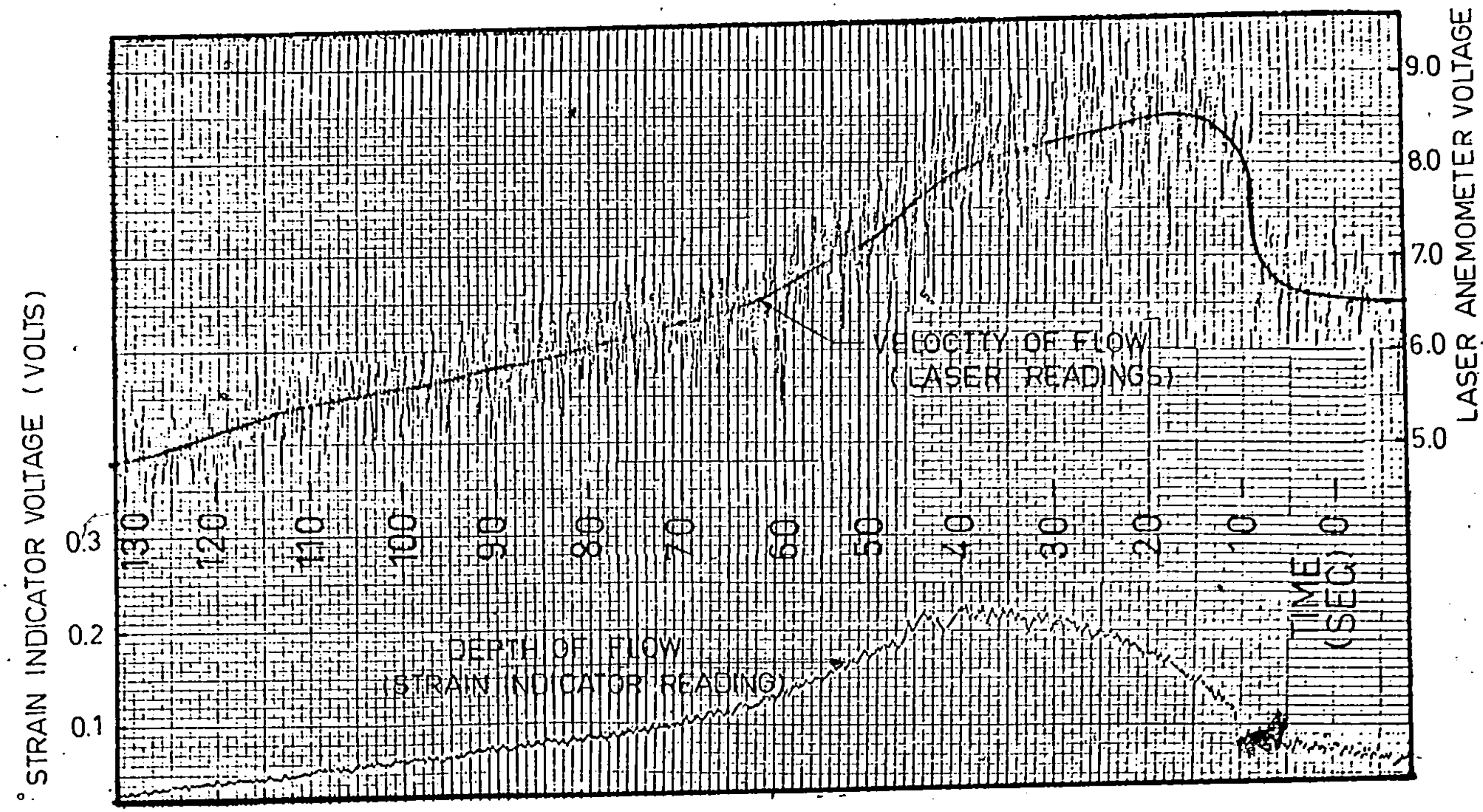

Fig. 4.26 Sample of Experimental Results for an Outlet Hydrograph (S_o = 0.0033)

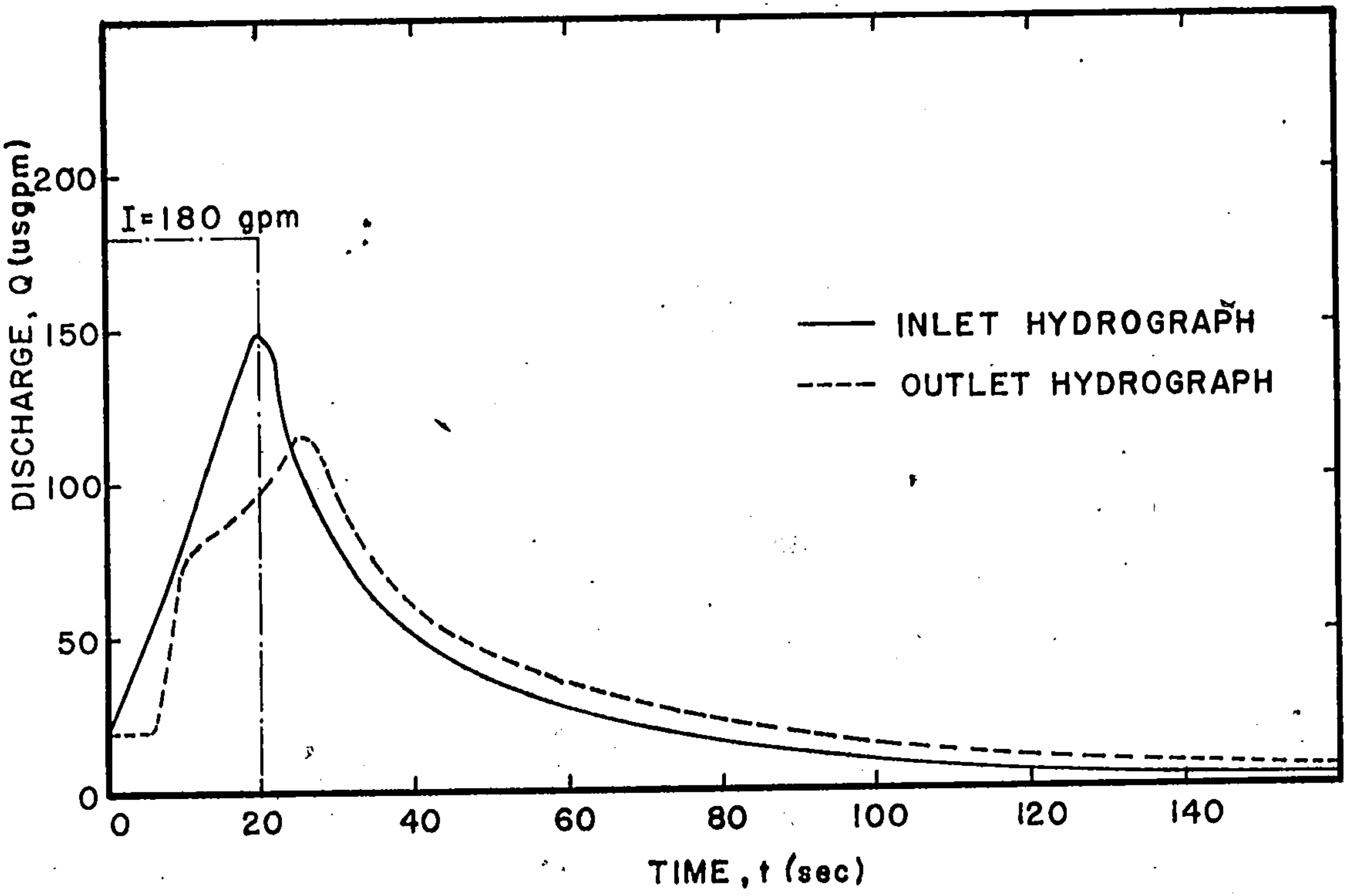

Fig. 4.27 The Inlet and Outlet Hydrographs for Storm Duration t = 20 Second and Critical Slope (S_o = 0.0033)

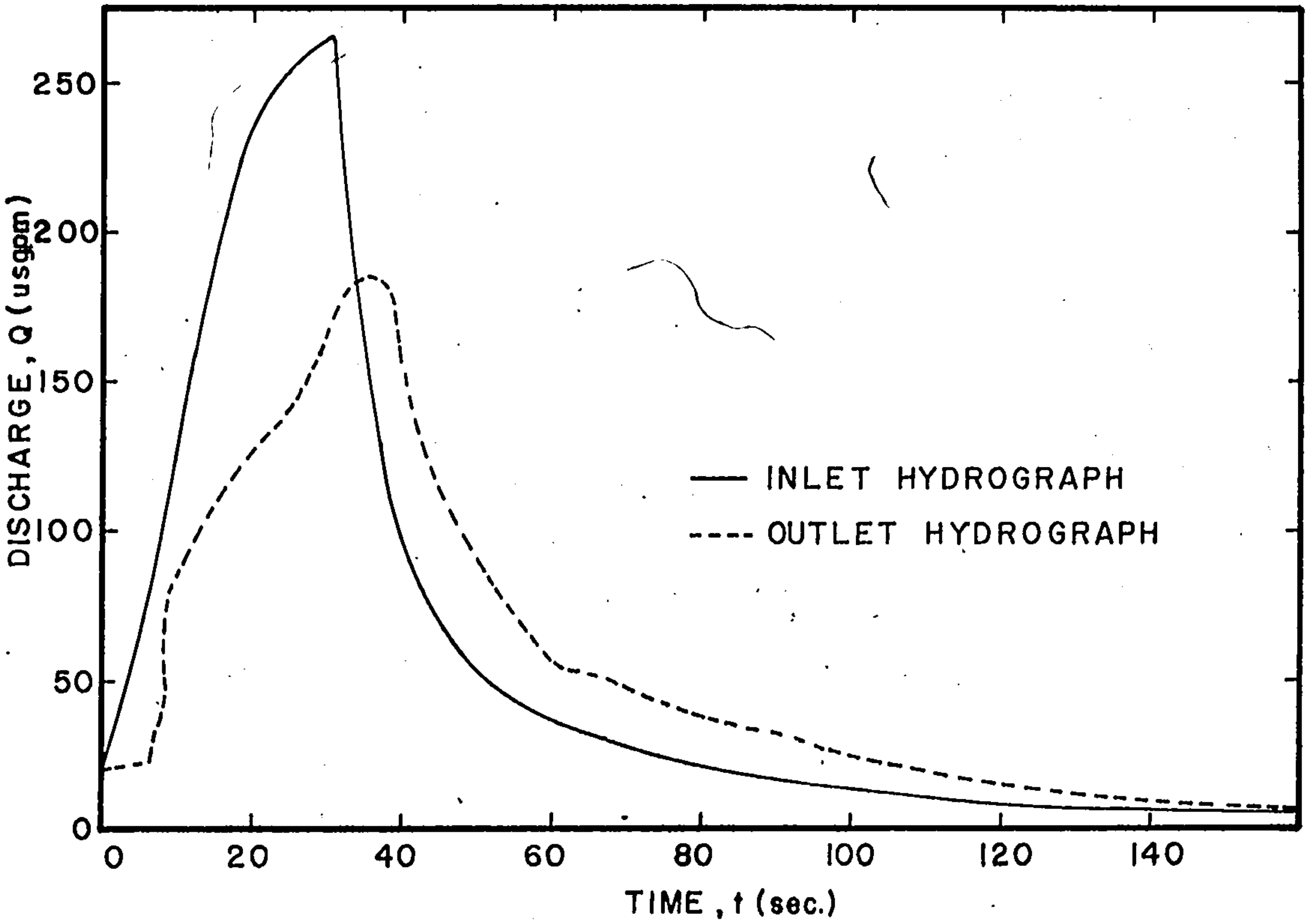

Fig. 4.28 The Inlet and Outlet Hydrographs for Storm Duration t = 30 Second and Critical Slope (S_o = 0.0033)

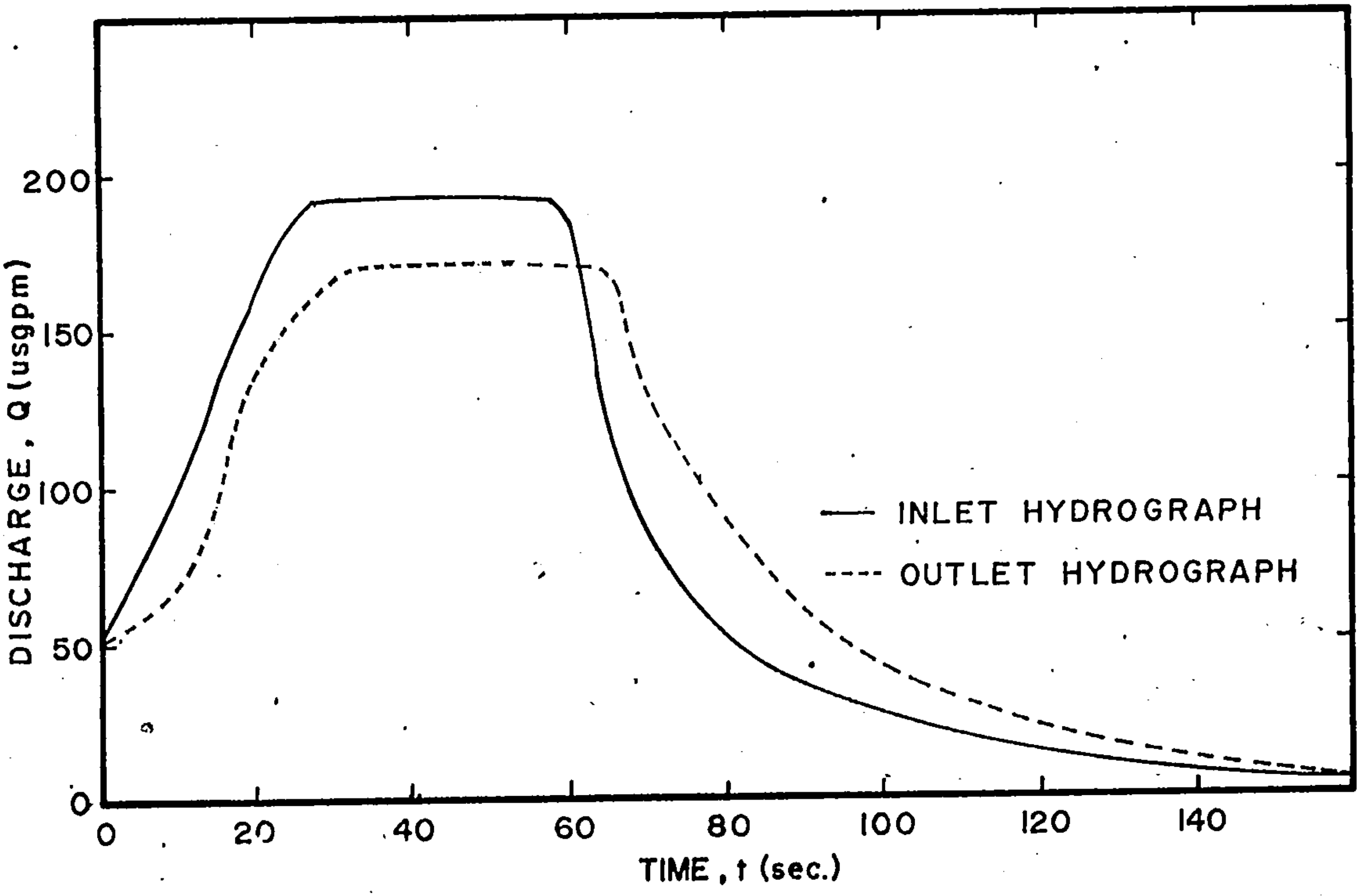

Fig. 4.29 The Inlet and Outlet Hydrographs for Storm Duration t = 60 Second and Critical Slope ($S_o = 0.0033$)

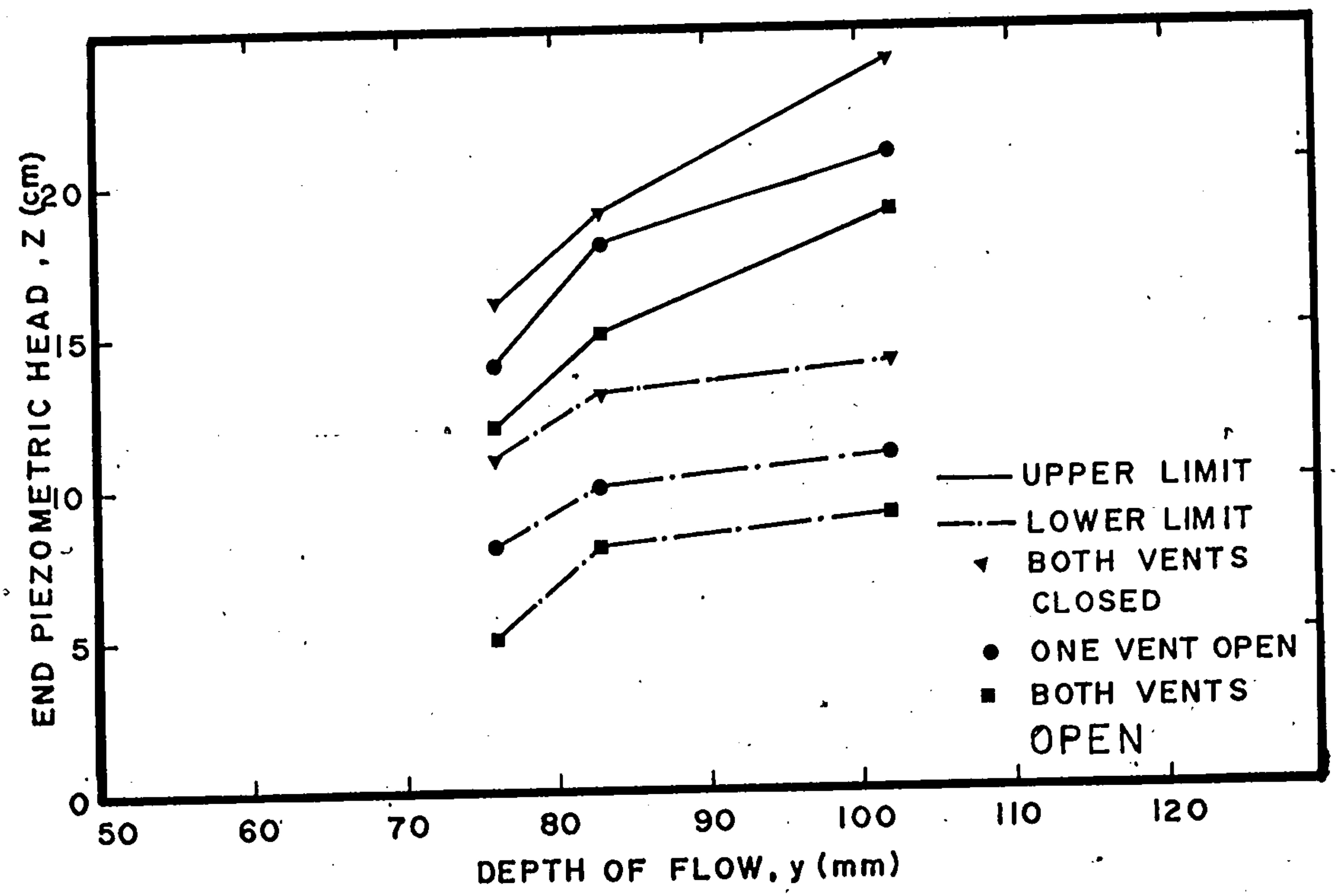

Fig.4.30 Effect of Vents on the Downstream Piezometric Head (Z) (Upper and Lower Readings)

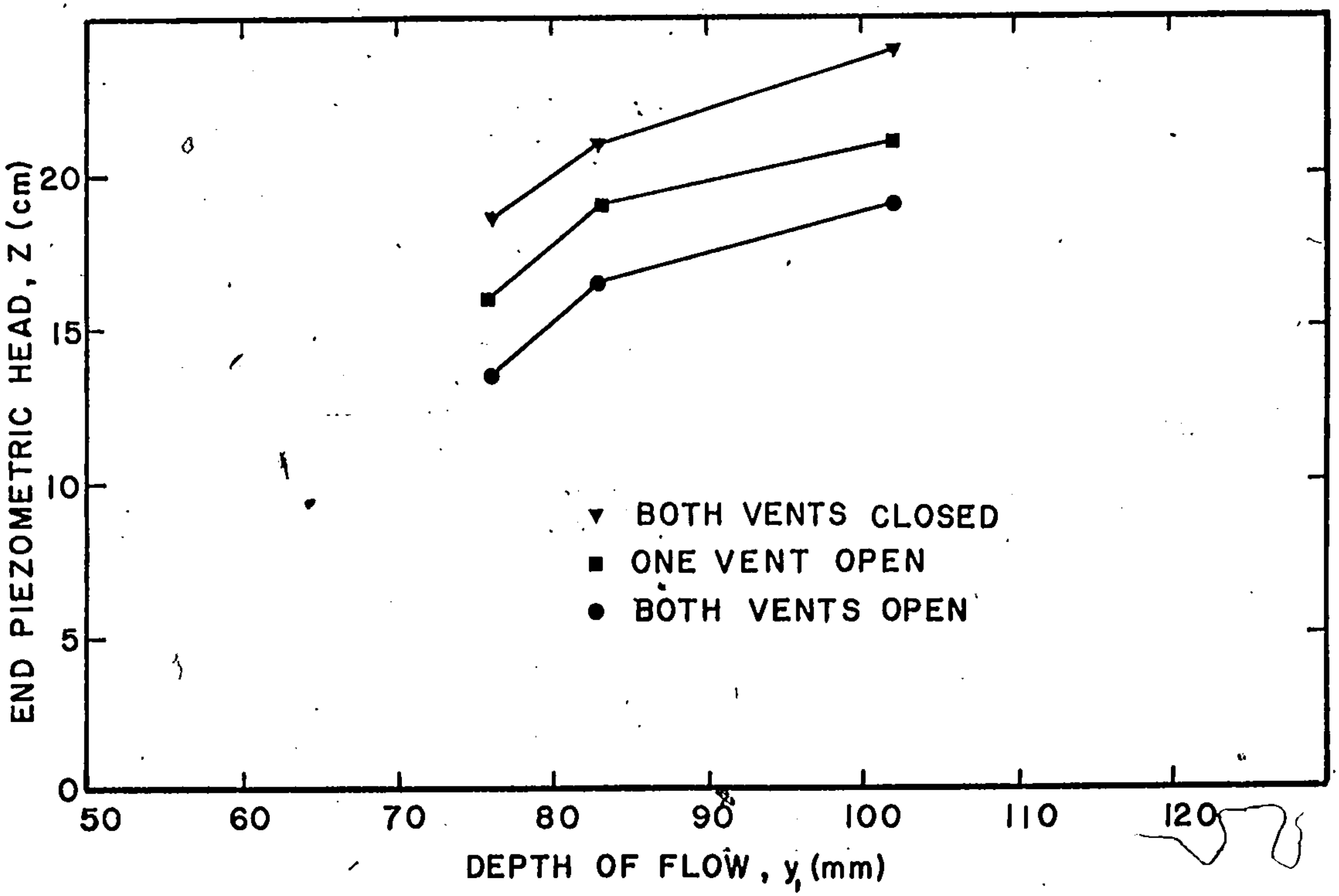

Fig. 4.31 Effect of Air Vents on the Downstream Piezometric Head (Z) (Mean Values)

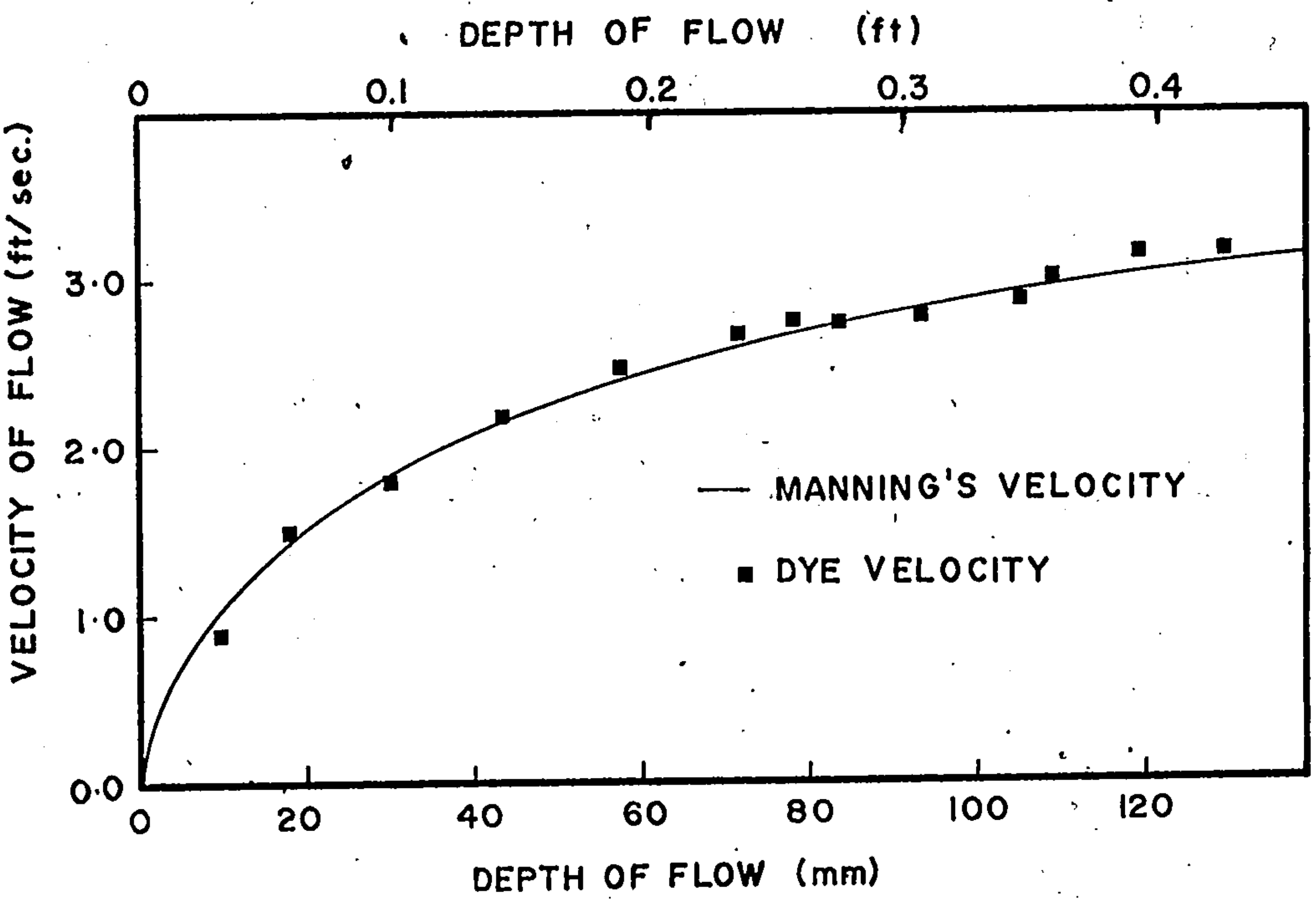

Fig. 4.32 Dye Velocities and Manning's Velocities for Different Flow Depths for Critical Slope ($S_o = 0.0033$)

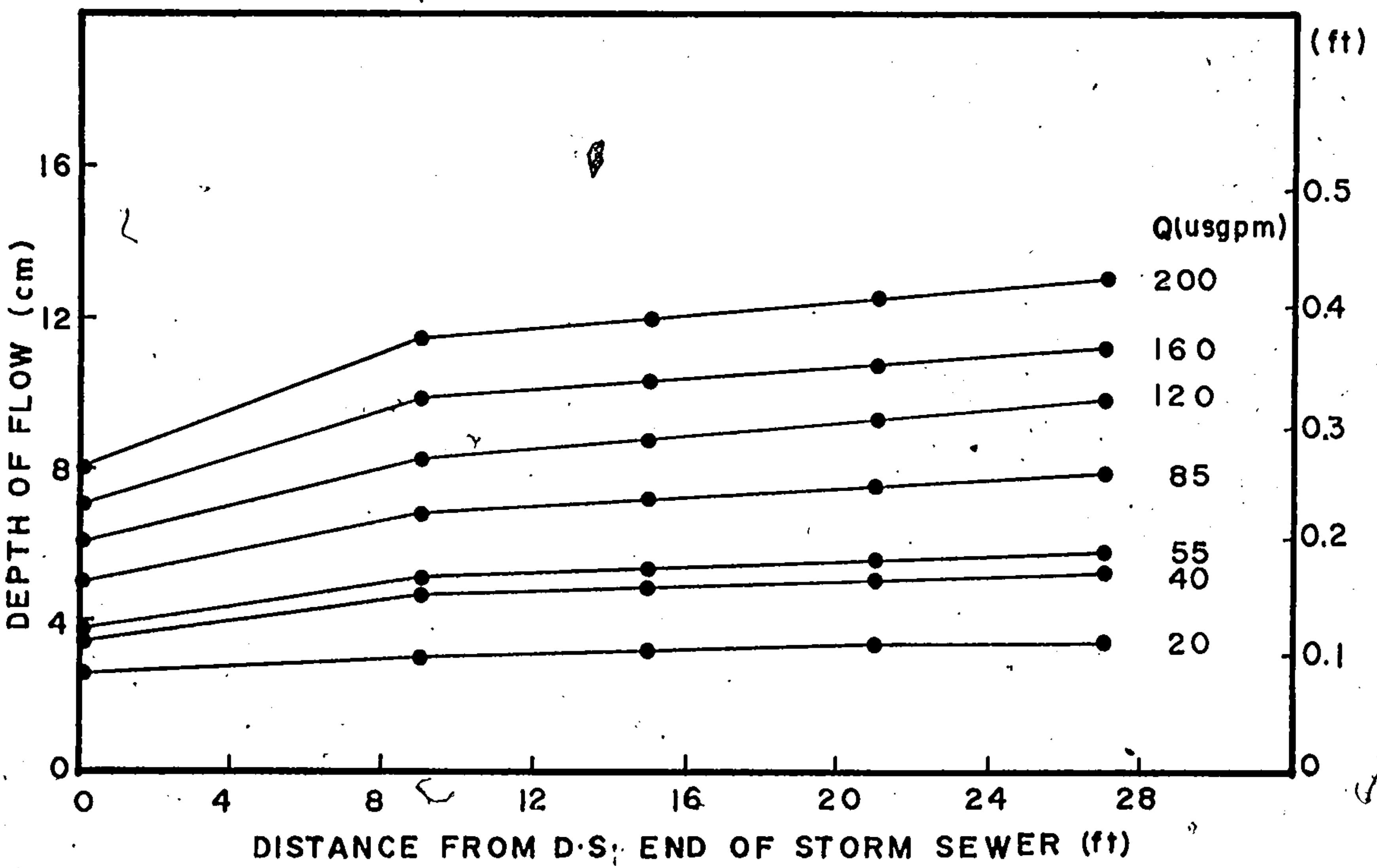

Fig. 4.33 Gradually Varied Flow Profiles for Different Flow Discharges (S_o = 0.00109)

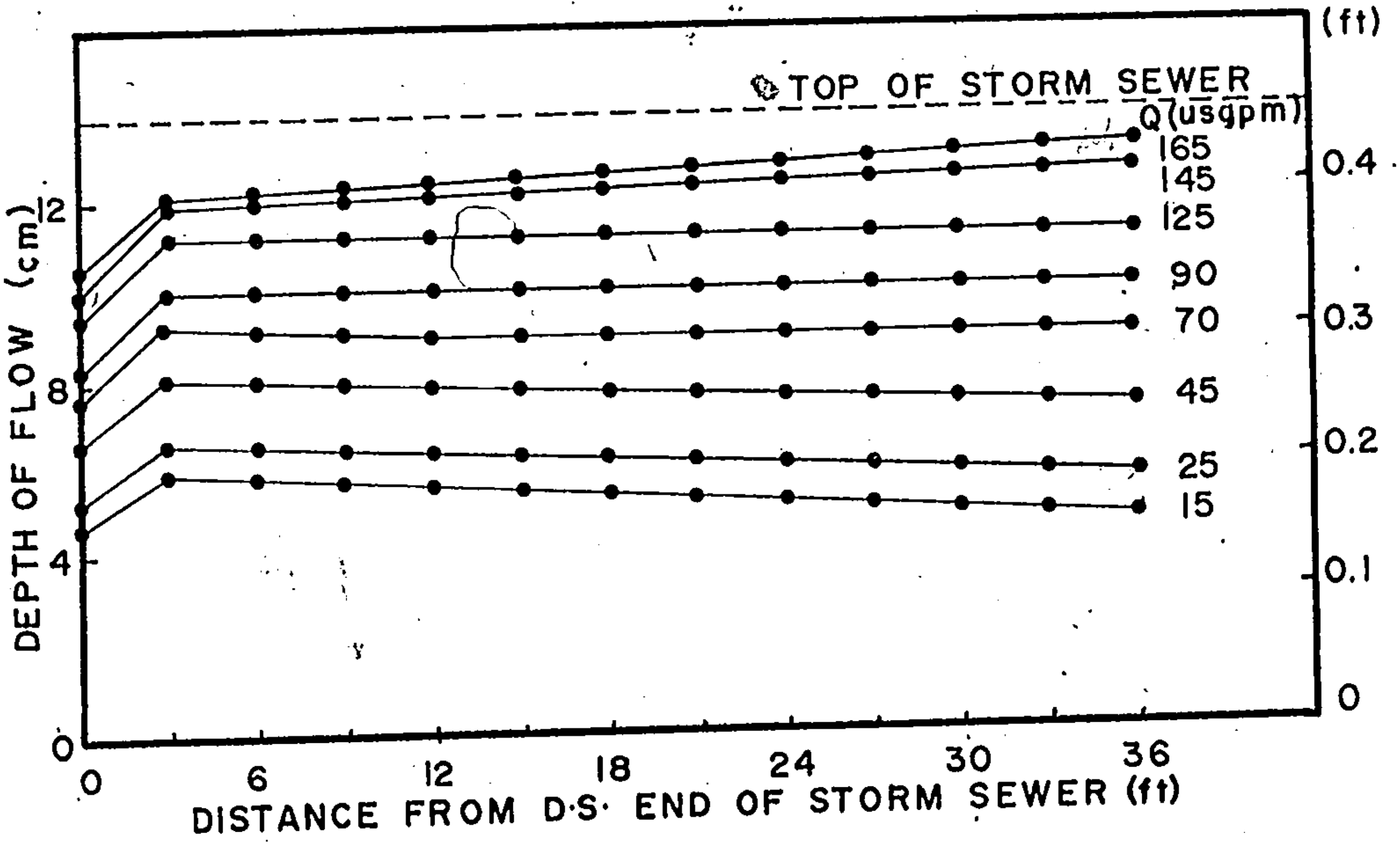

Fig. 4.34 Gradually Varied Flow Profiles for Different Flow Discharges Using and End Sill ($S_o = 0.00109$)

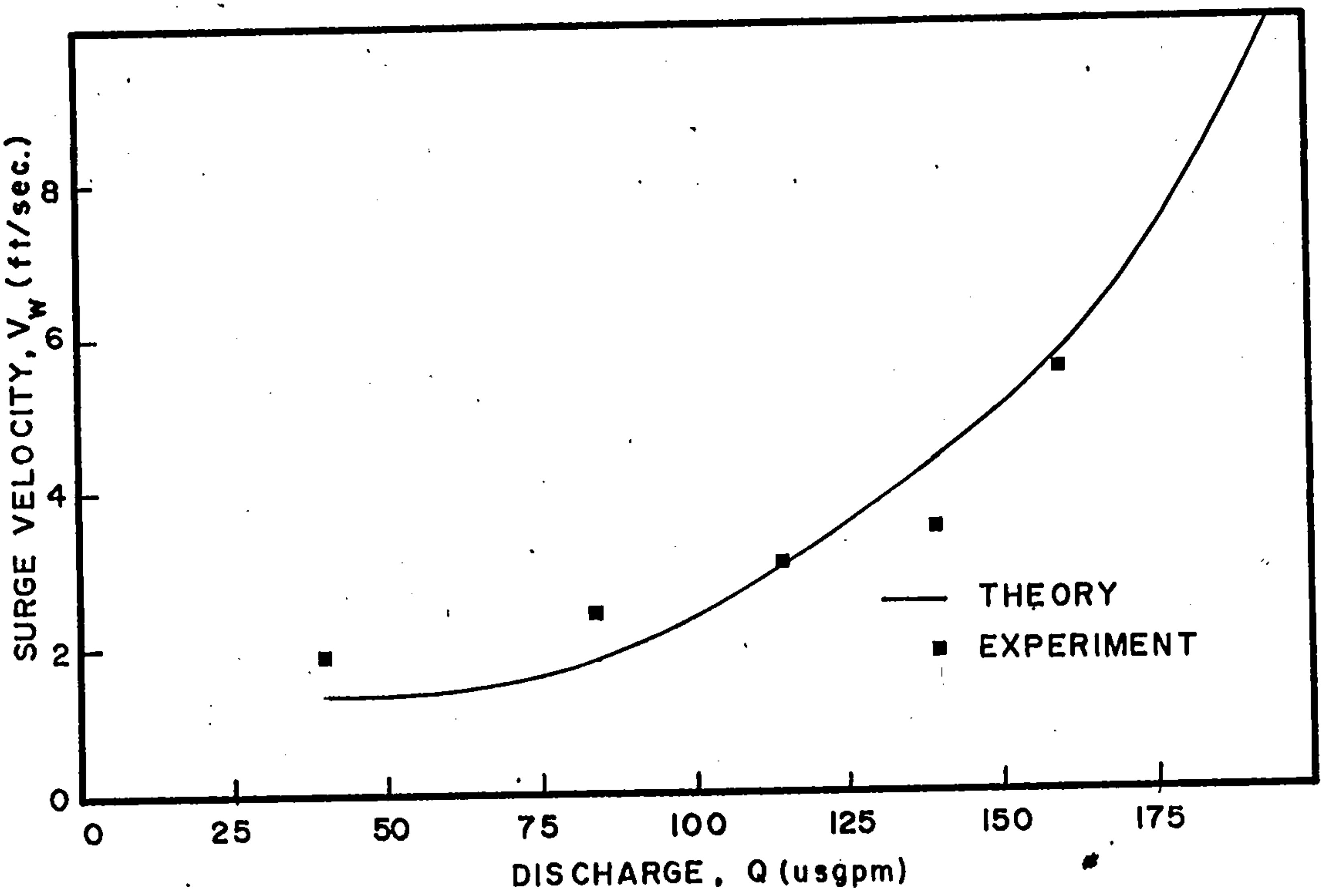

Fig. 4.35 Theoretical and Experimental Surge Velocities for Different Flow Discharges (S_o = 0.00109)

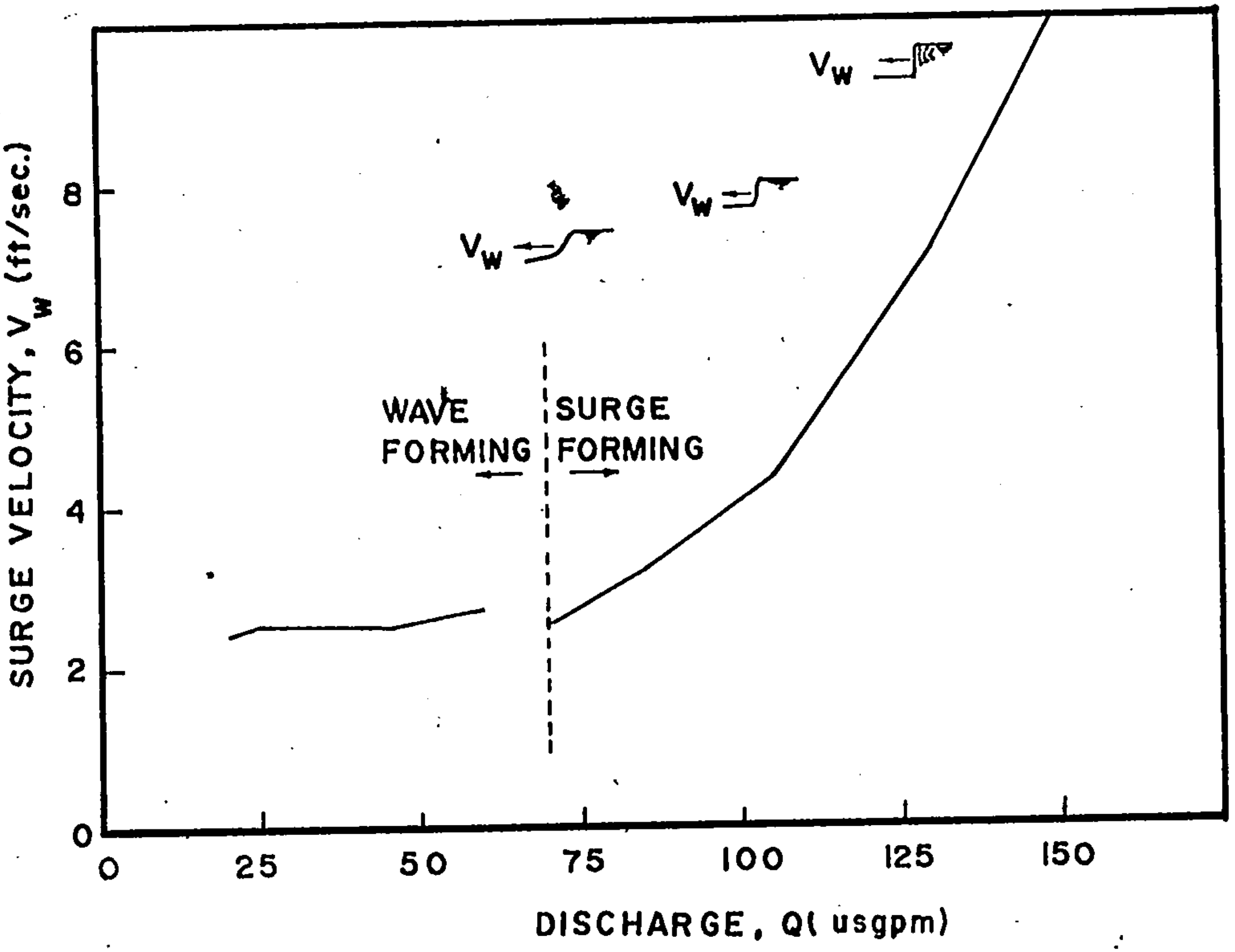

Fig. 4.36 Surge Velocities Using an End Sill at the Downstream End for Different Discharges (S_o = 0.00109)

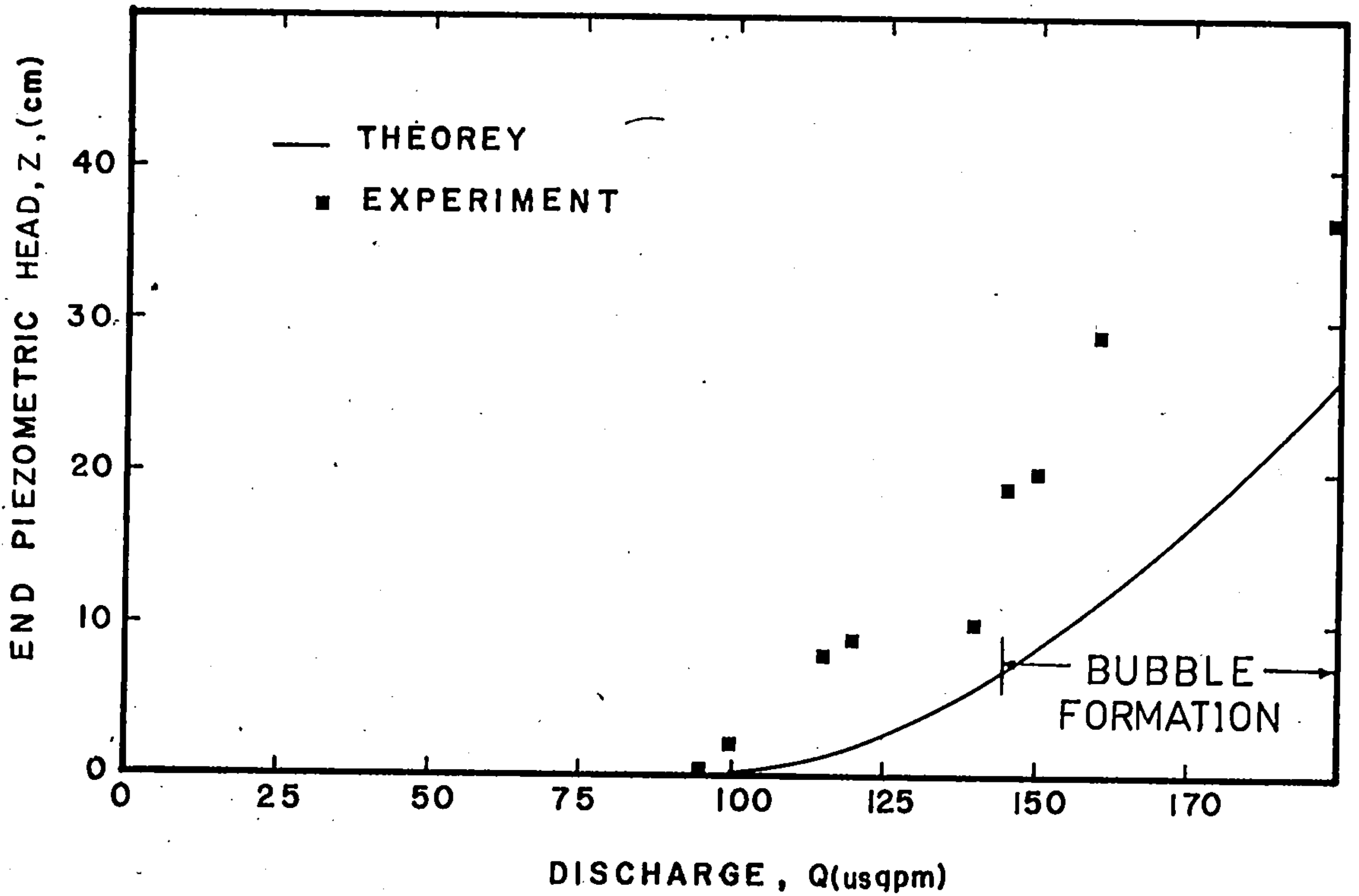

Fig. 4.37 Theoretical and Experimental Curves of the Piezometric Head for Different Discharges (S_o = 0.00109)

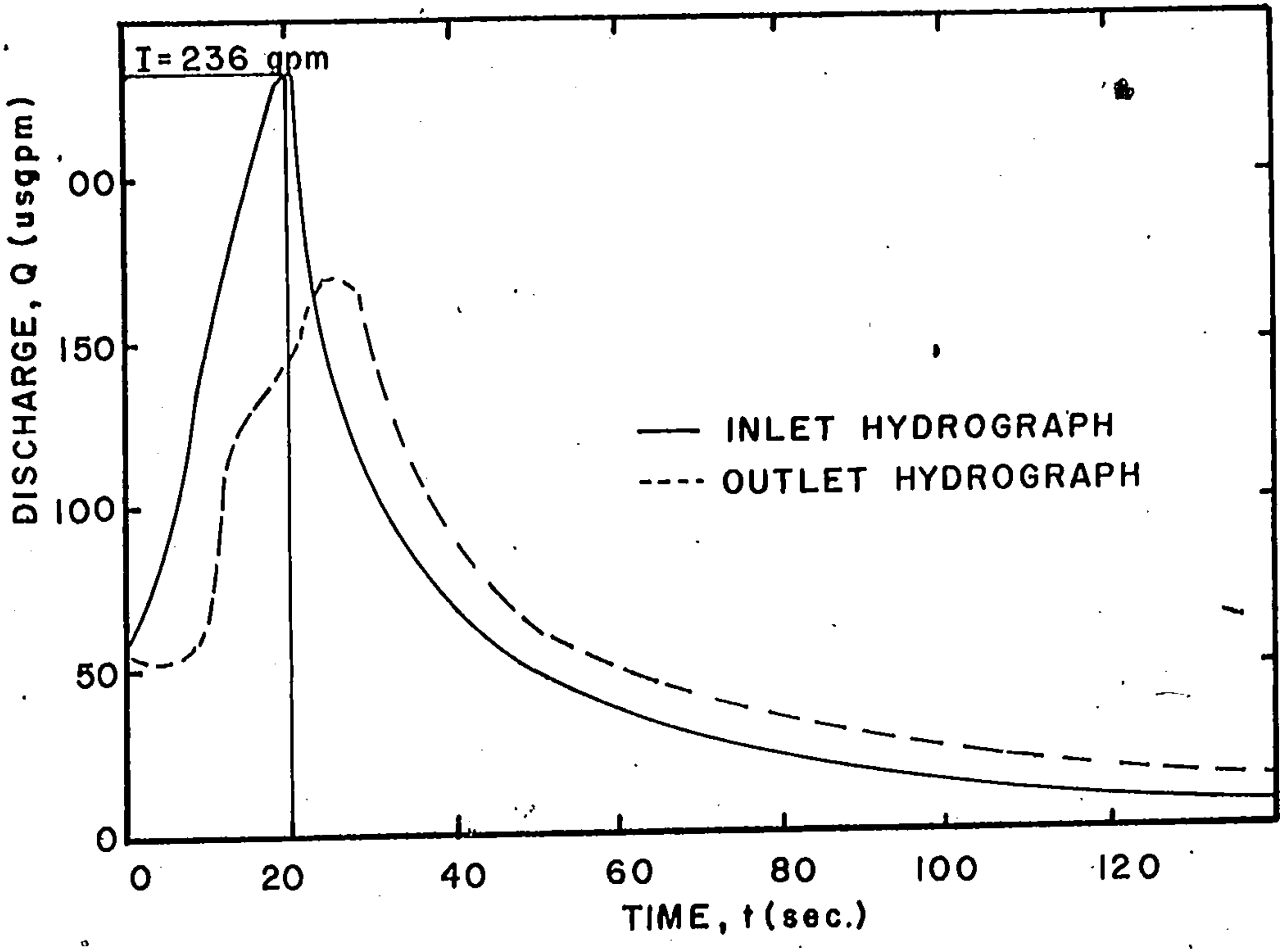

Fig. 4.38 The Inlet and Outlet Hydrographs for Storm Duration t = 20 second and Sub Critical Slope (S_o = 0.00109)

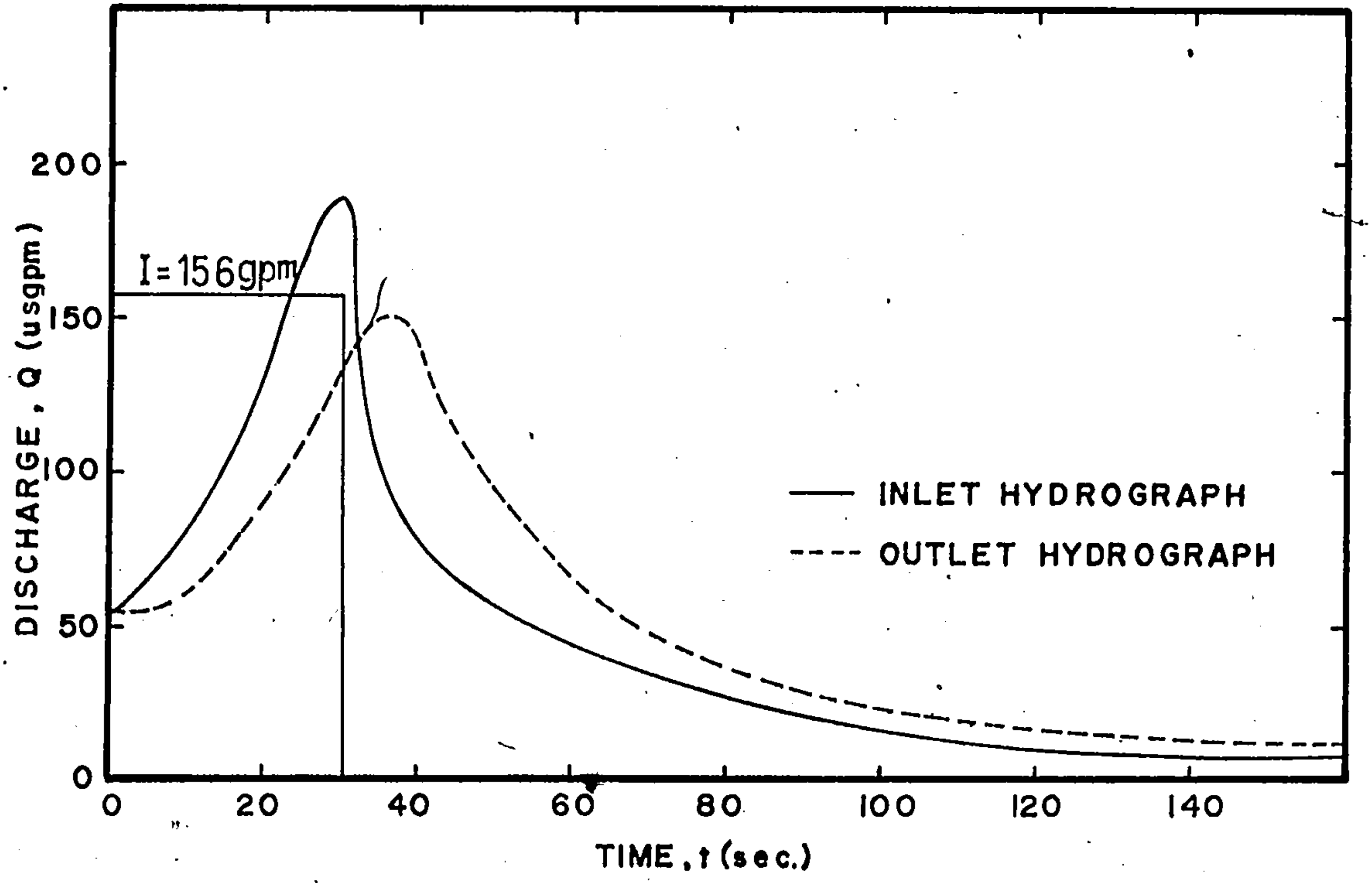

Fig. 4.39 The Inlet and Outlet Hydrographs for Storm Duration t = 30 second and Sub Critical Slope (S_o = 0.00109)

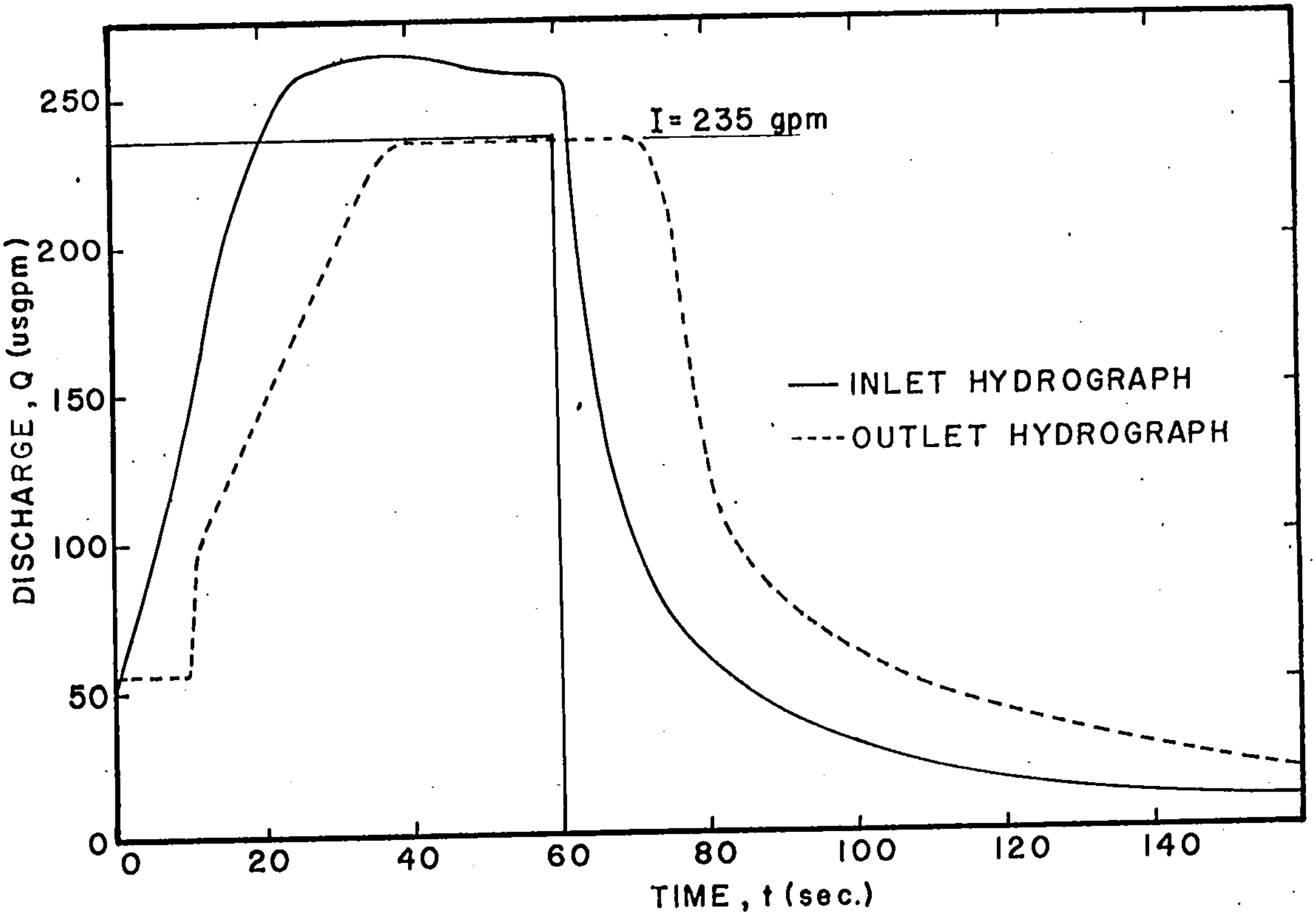

Fig. 4.40 The Inlet and Outlet Hydrographs for Storm Duration t = 60 second and Sub Critical Slope ($S_o = 0.00109$)

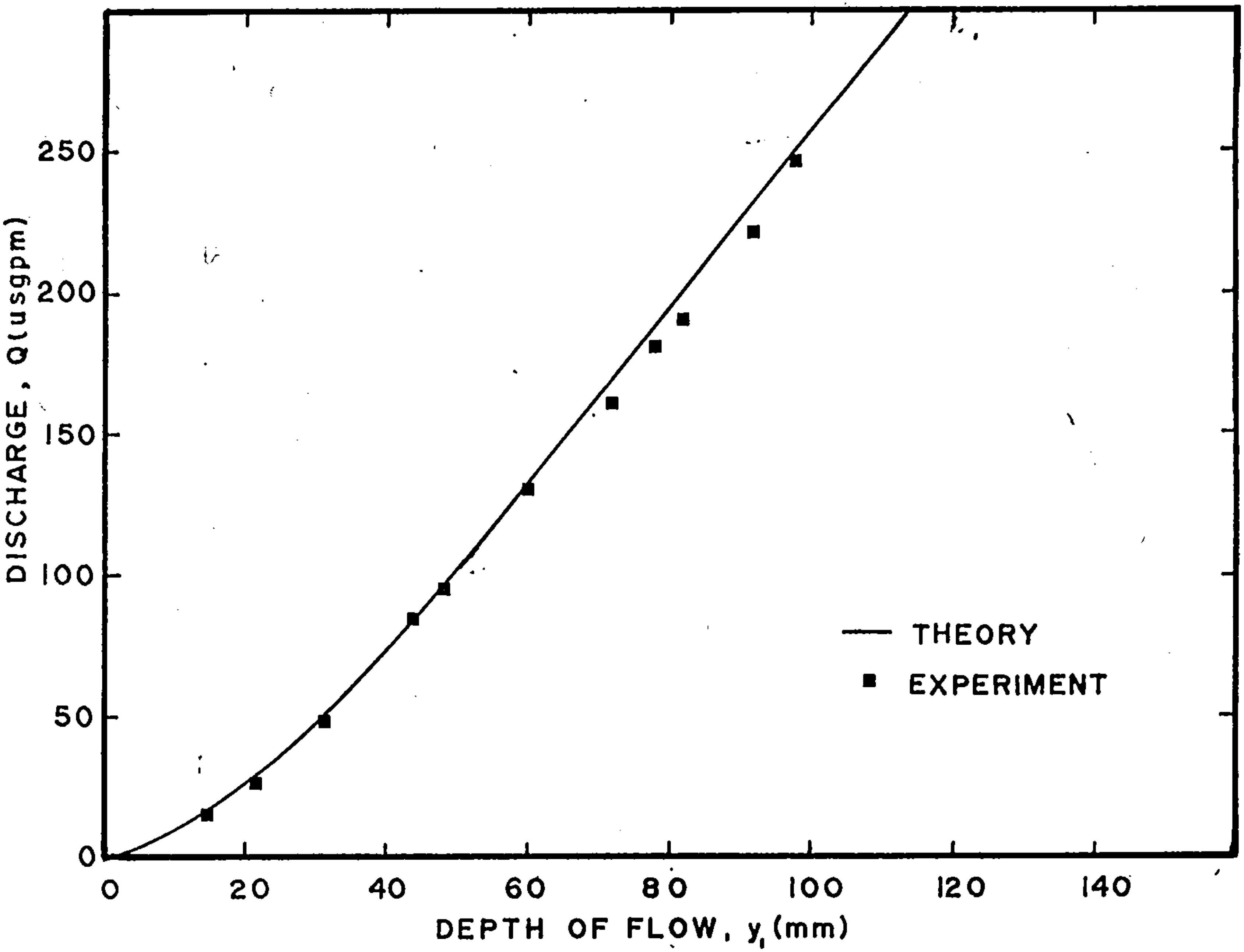

Fig. 4.41 The Theoretical and Experimental Discharges for Supercritical Slope (S_o = 0.0061).

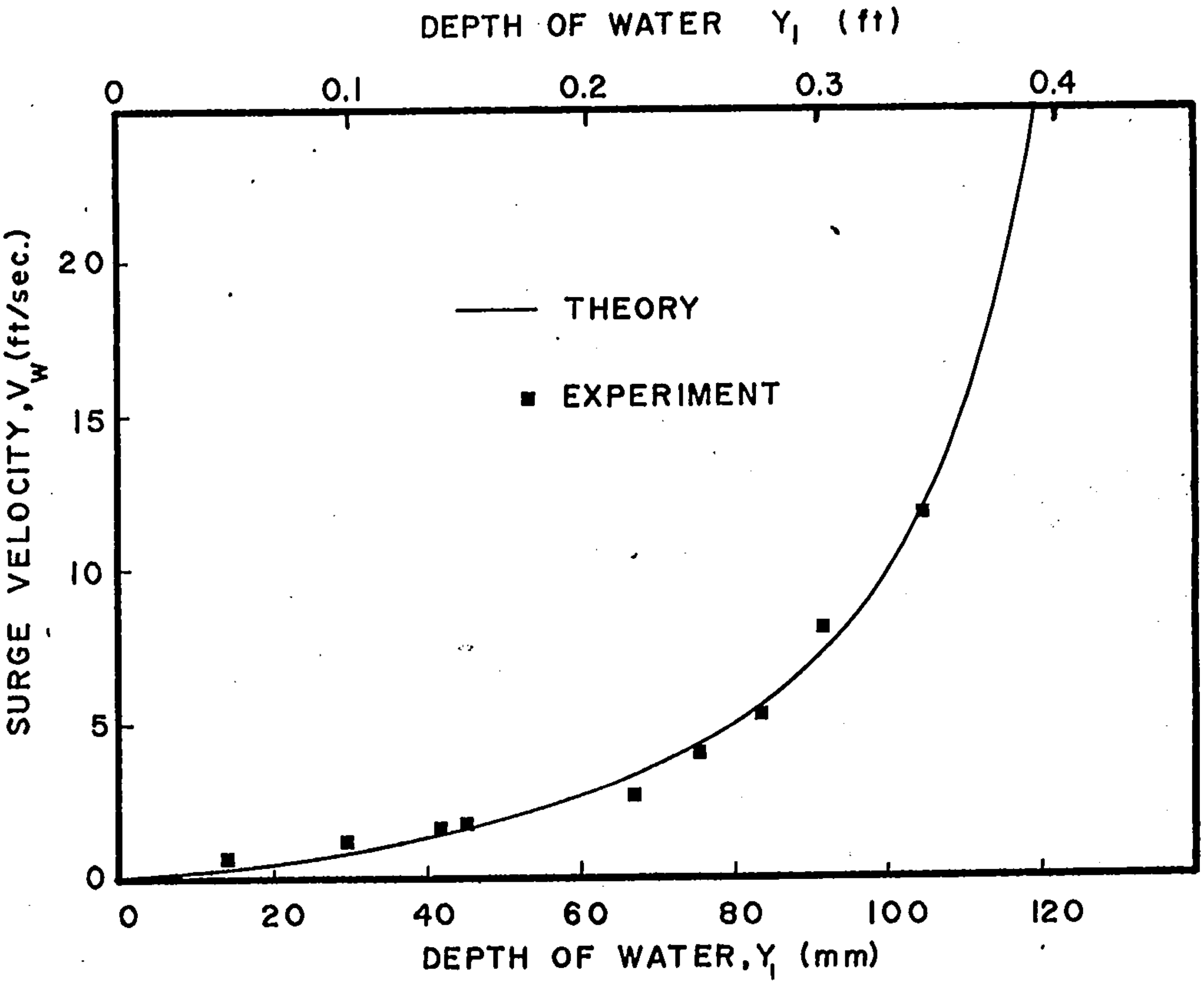

Fig. 4.42 The Theoretical and Experimental Surge Velocities for Different Flow Depths (S_o = 0.0061)

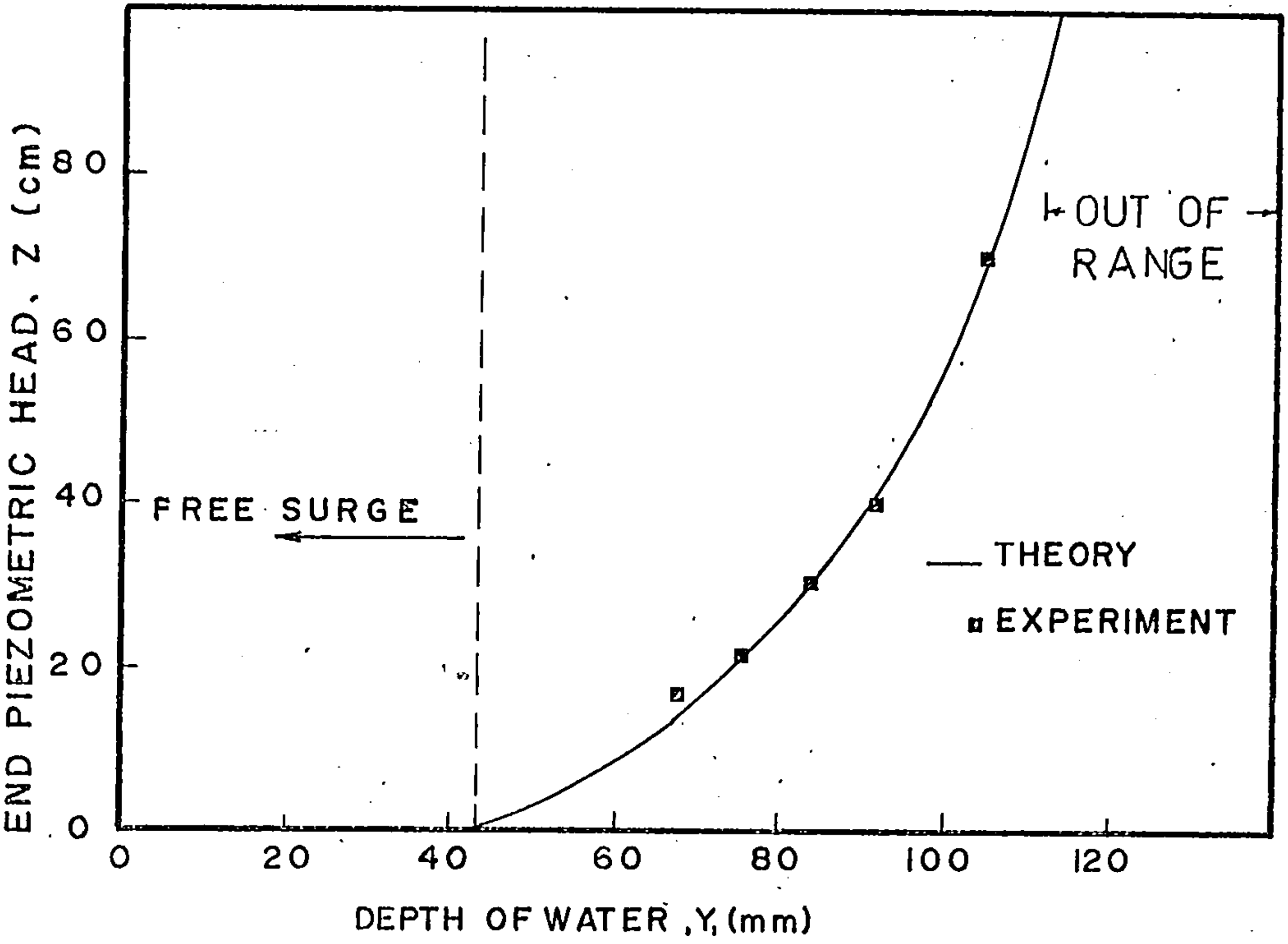

Fig. 4.43 The Theoretical and Experimental Piezometric Head (Z) for Different Flow Depths (S_o = .0061)

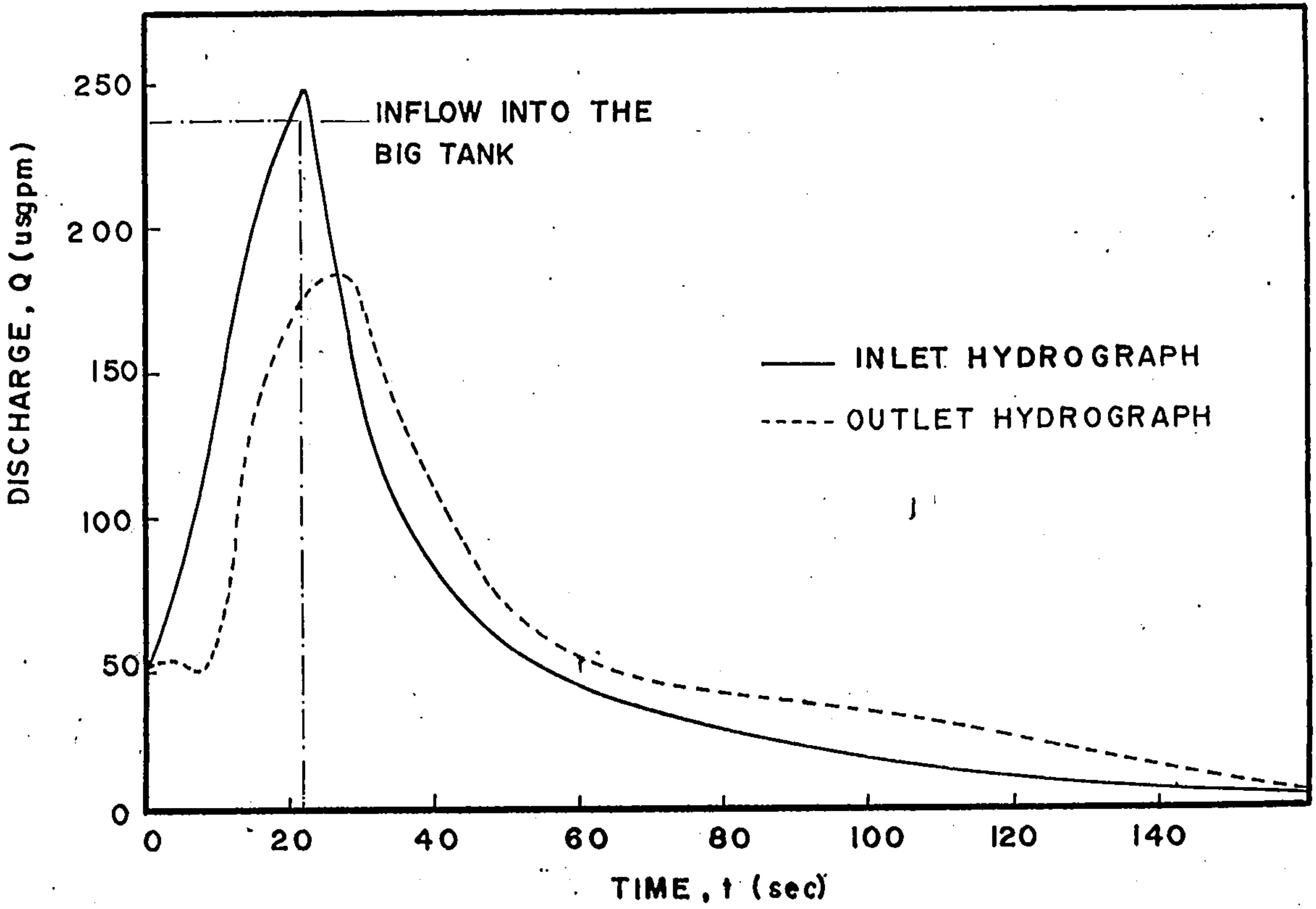

Fig. 4.44 The Inlet and Outlet Hydrographs for Storm Duration t = 22 second and Super Critical Slope (S_o = 0.0061)

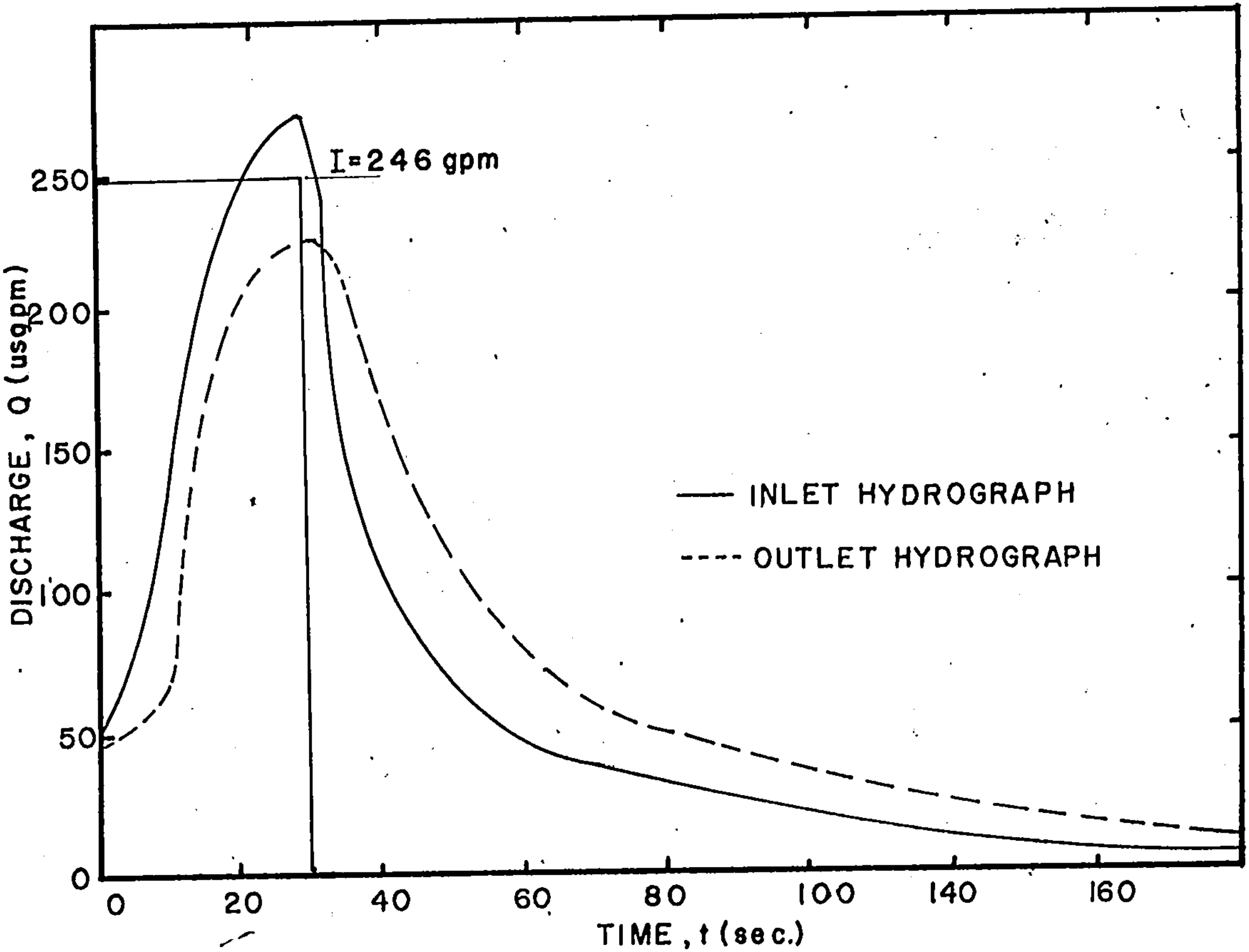

Fig. 4.45 The Inlet and Outlet Hydrographs for Storm Duration t = 30 second and Supercritical Slope (S_o = 0.0061)

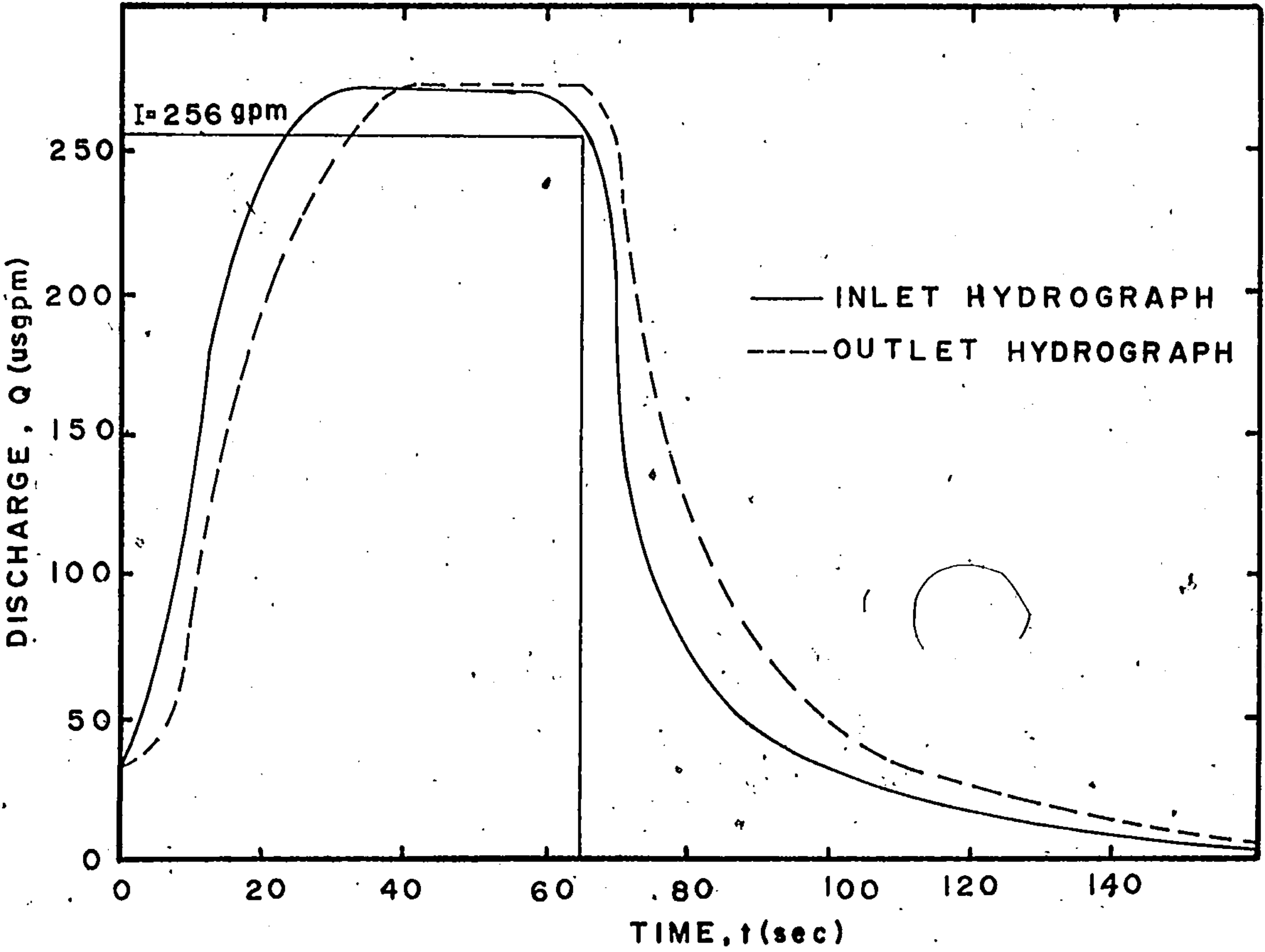

Fig. 4.46 The Inlet and Outlet Hydrographs for Storm Duration t = 65 second and Supercritical Slope (S_o = 0.0061)

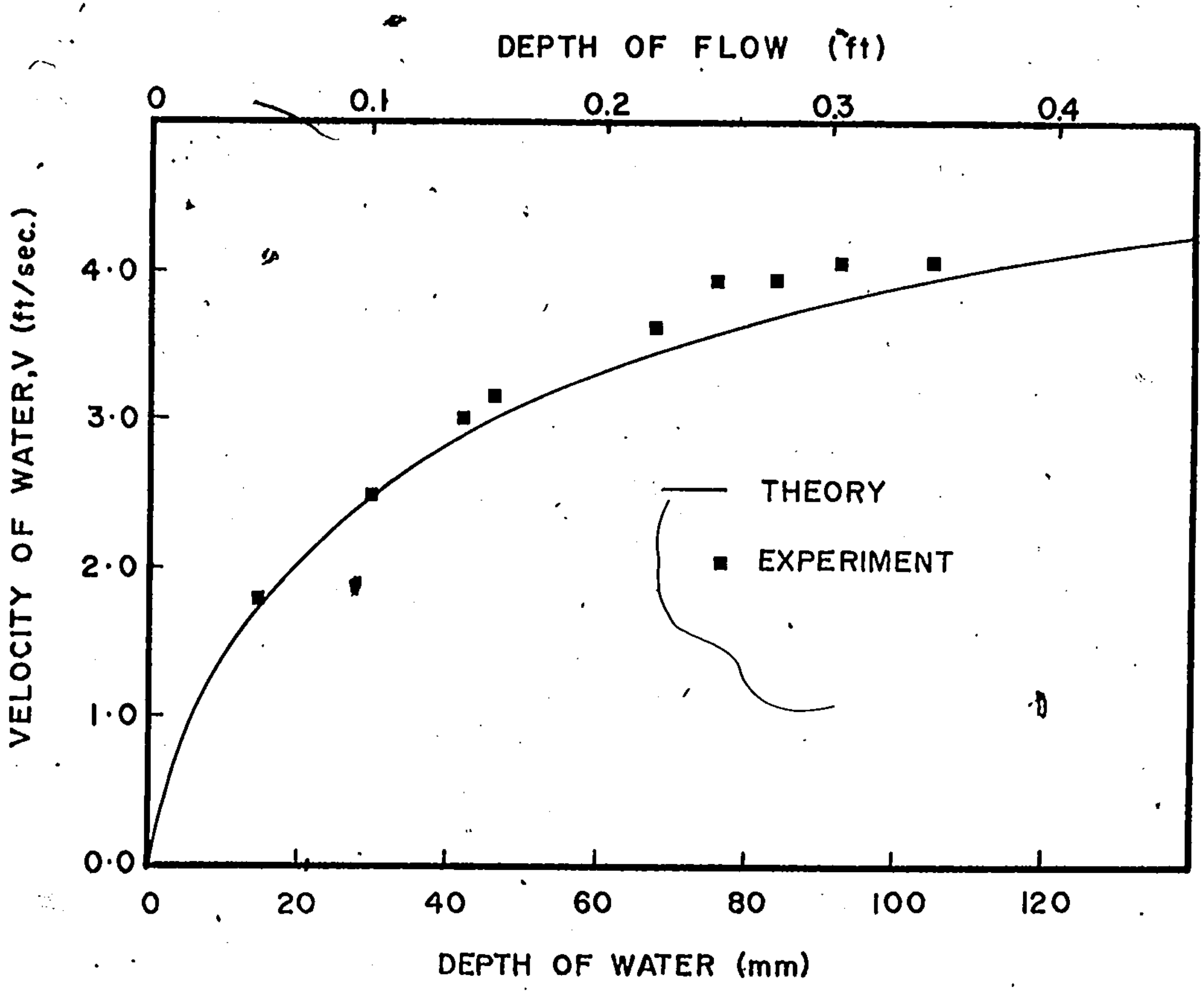

Fig. 4.47 Dye Velocities and Manning's Velocities for Different Flow Depths for Supercritical Slope (S_o = 0.0061)

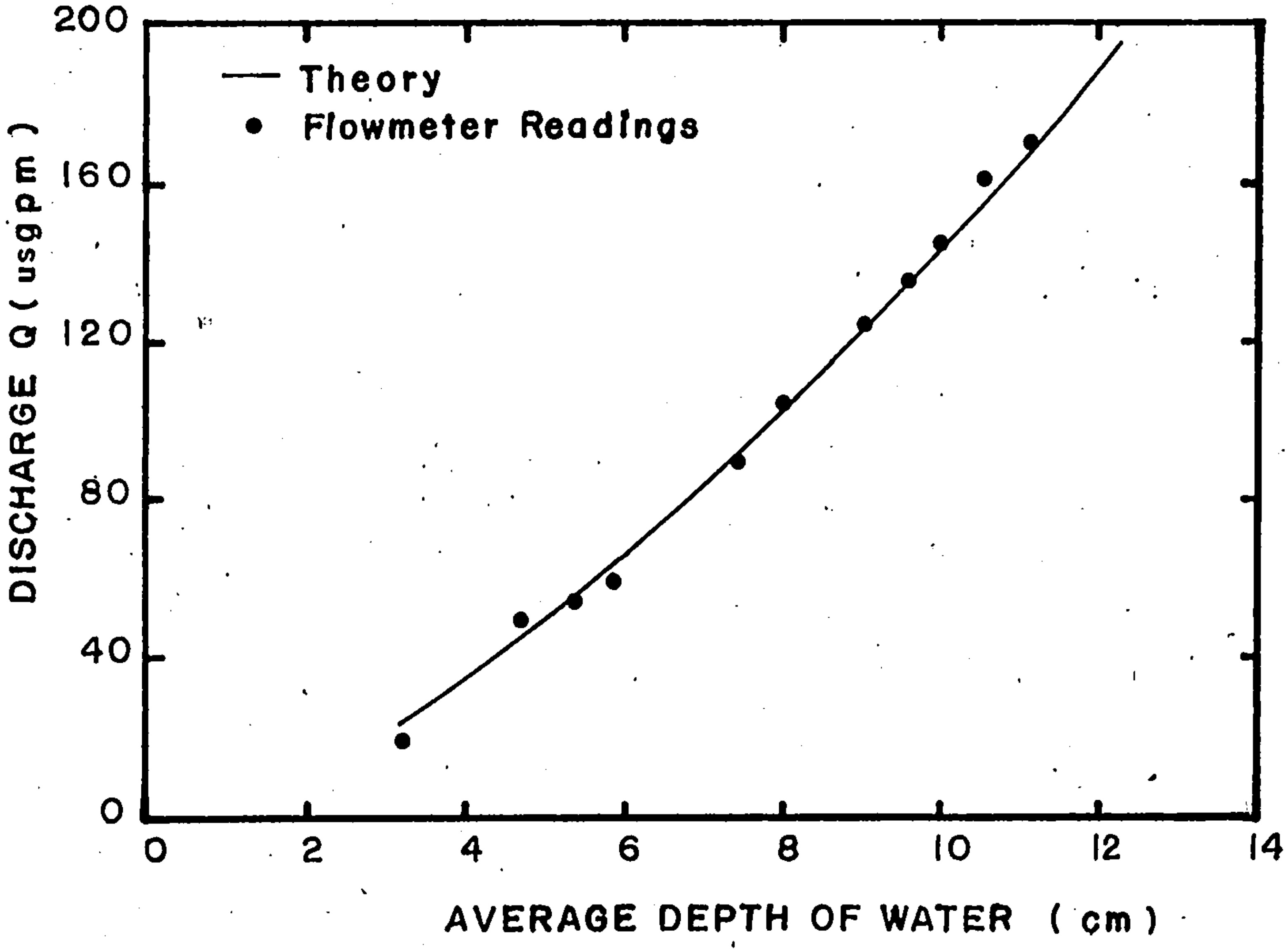

Fig. 5.1 Theoretical Discharges (for $\alpha = 1.2$, and $n = 0.0086$) Compared with the Flow Meter Readings for Subcritical Slope ($S_o = 0.00109$)

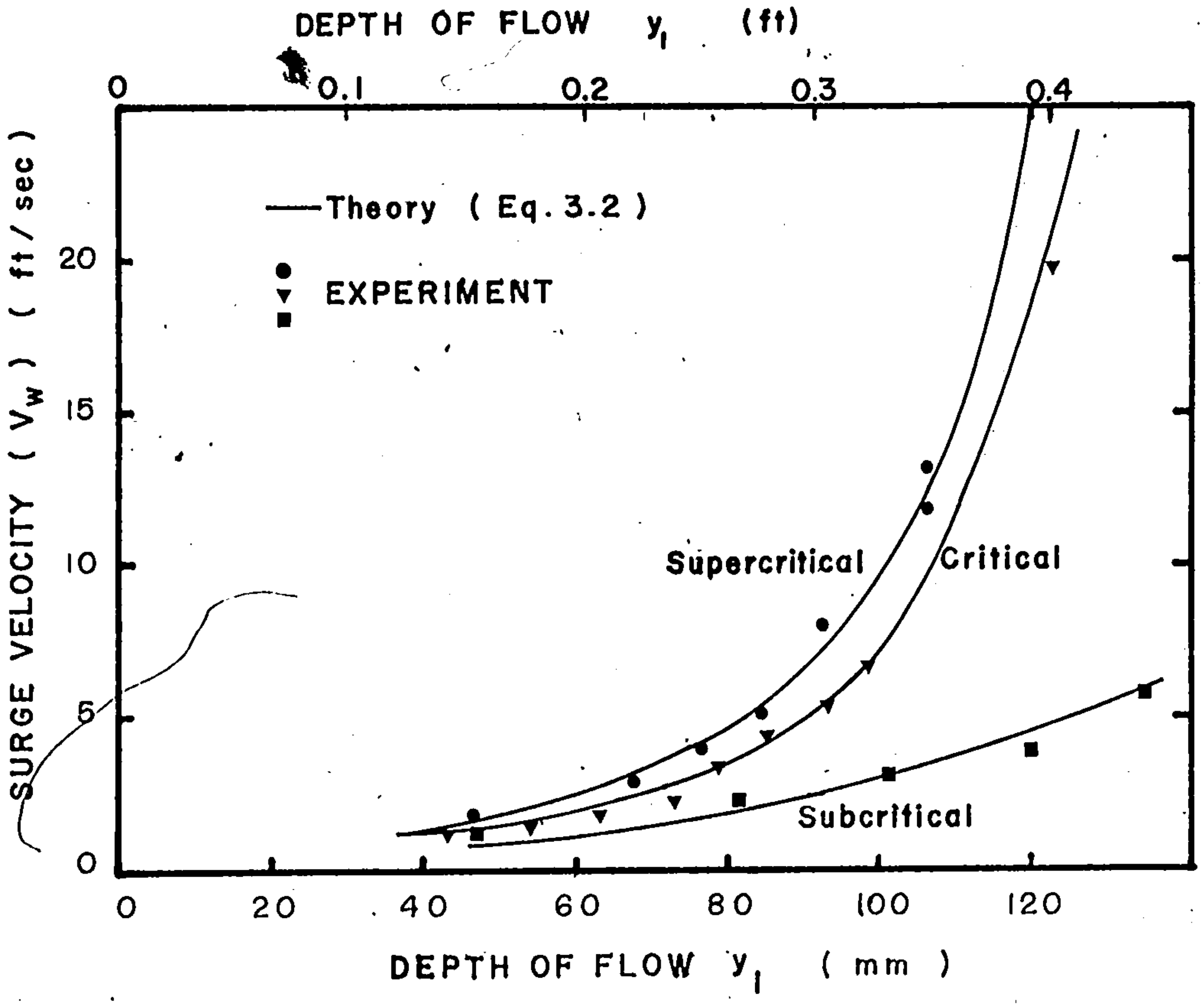

Fig. 5.2 The Effect of Bed Slope (S_o) on Surge Velocities (V_w)

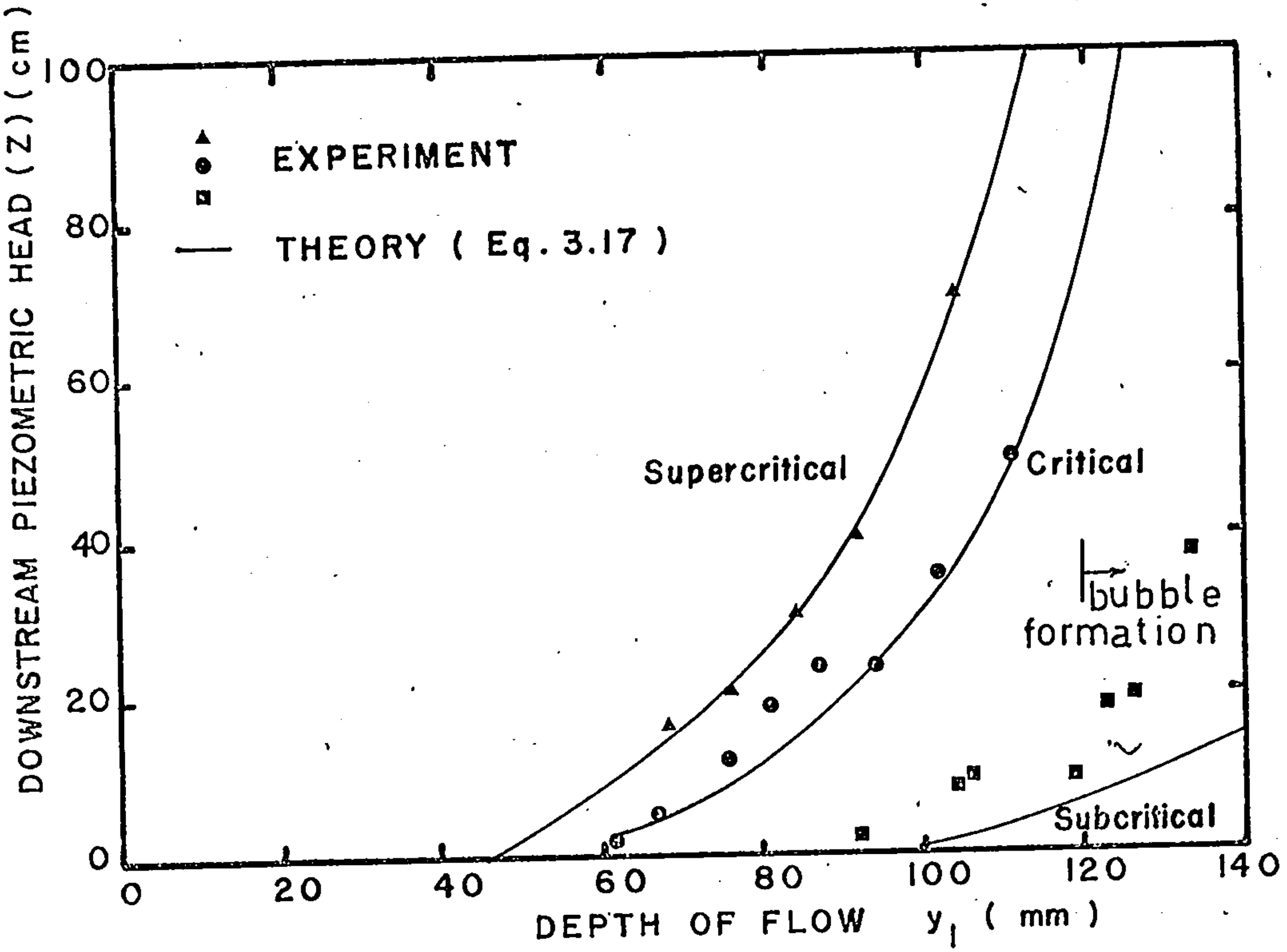

Fig., 5.3 The Effect of Bed Slope (S_o) on the Downstream Piezometric Heads (Z)

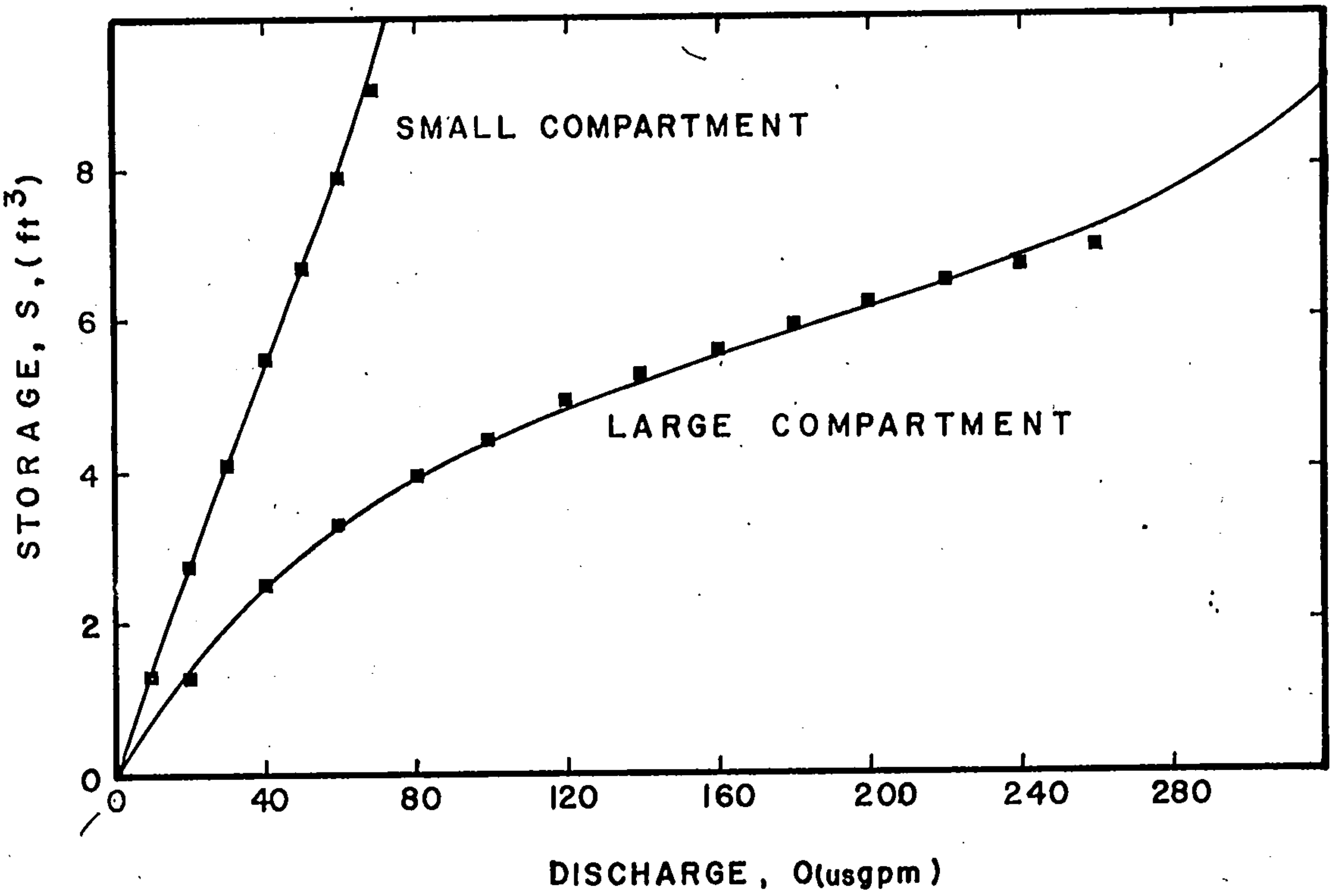

Fig. 5.4 Storage-Discharge Curves for the Two Compartments of the Overhead Tank

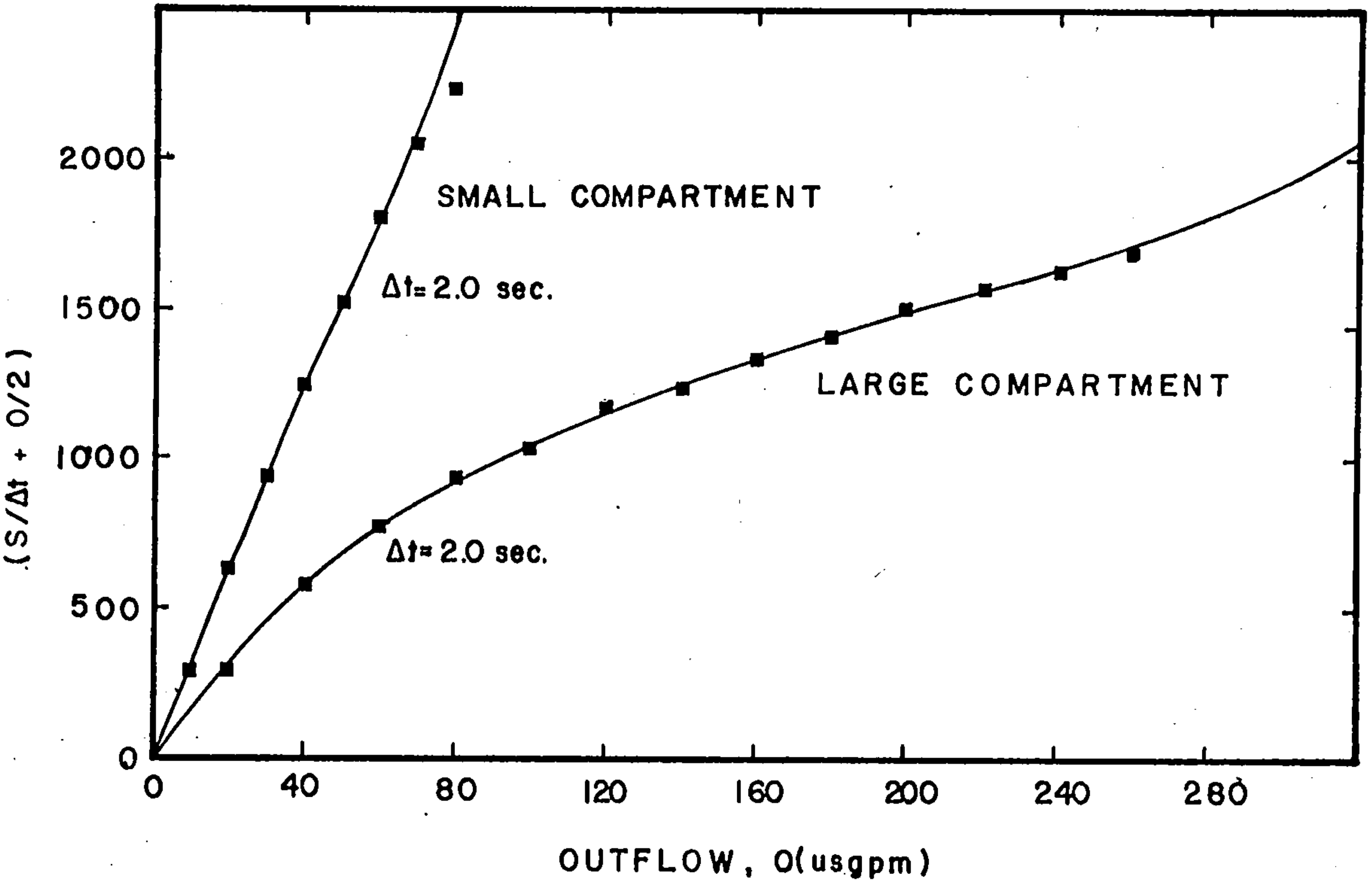

Fig. 5.5 Additional Routing Curves for the Two Compartments of the Overhead Tank (Δt = 2.0 sec.)

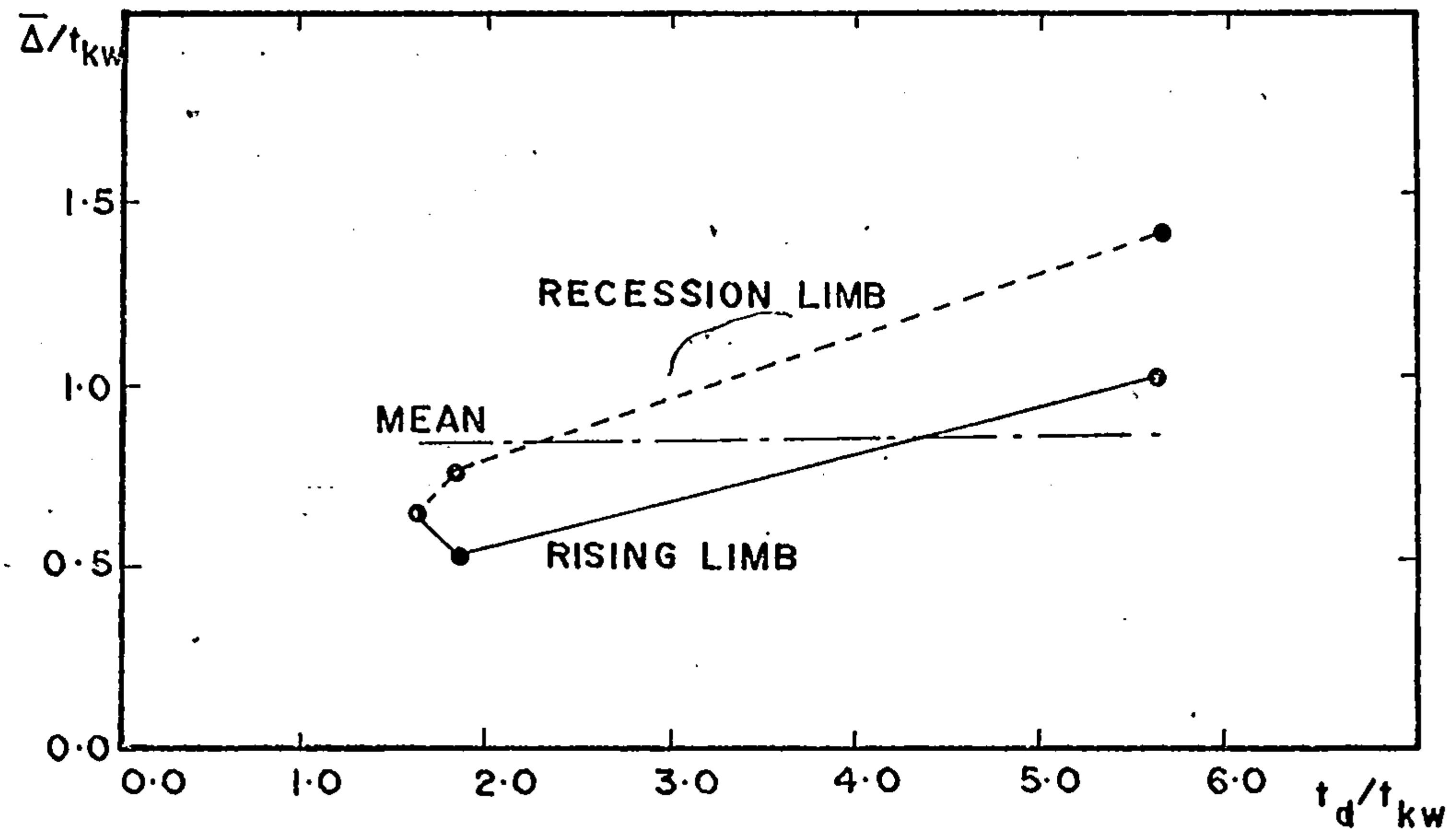

Fig. 5.6 Average Dimensionless Lag Time $(\frac{\overline{\Delta}}{t_{kw}})$ vs Storm Duration $(\frac{t_d}{t_{kw}})$ for Subcritical Slope (S_o = 0.00109)

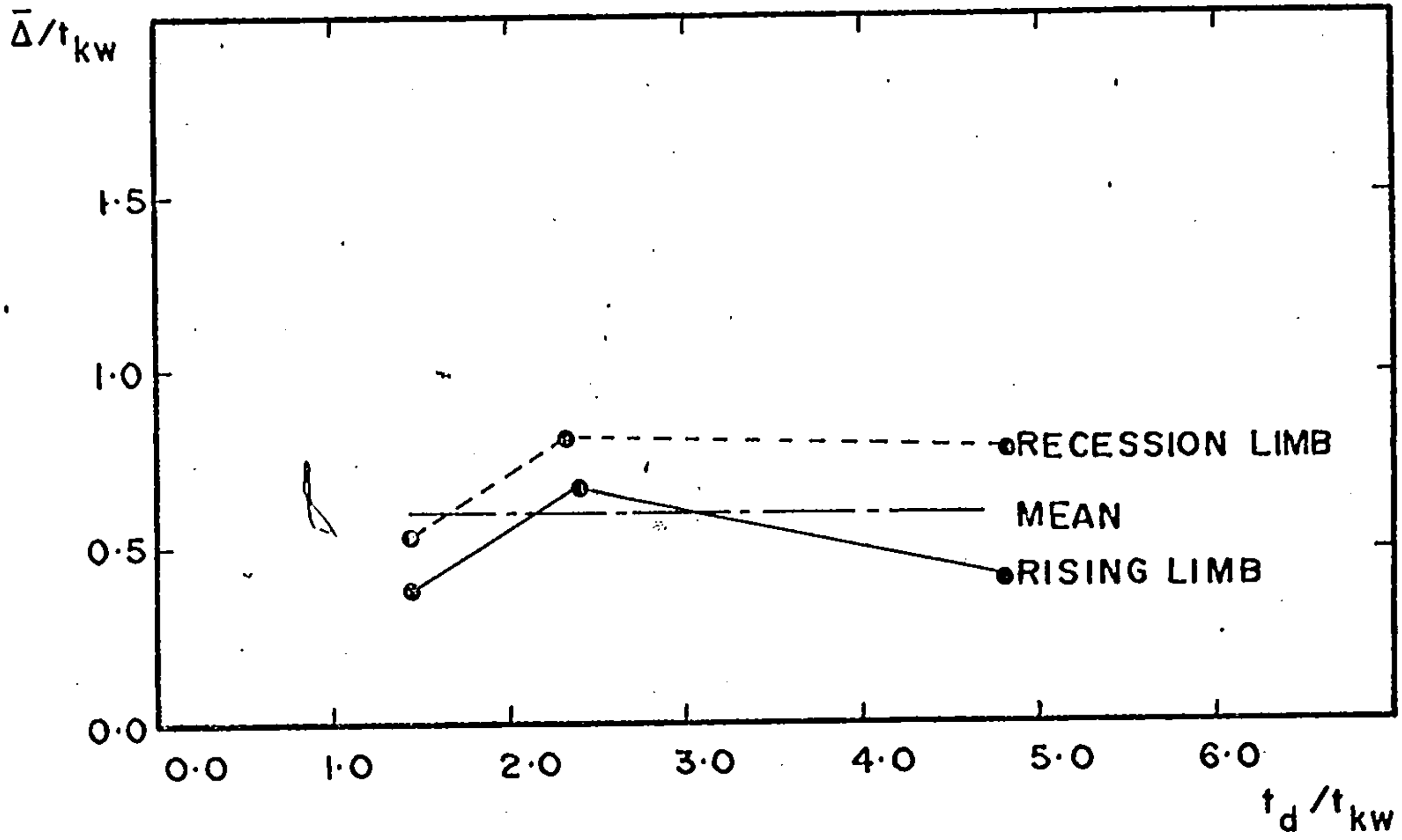

Fig. 5.7 Average Dimensionless Lag Time ($\frac{\bar{\Delta}}{t_{kw}}$) vs Dimensionless Storm Duration (t_d/t_{kw}) For Critical Slope (S_o = 0.0033)

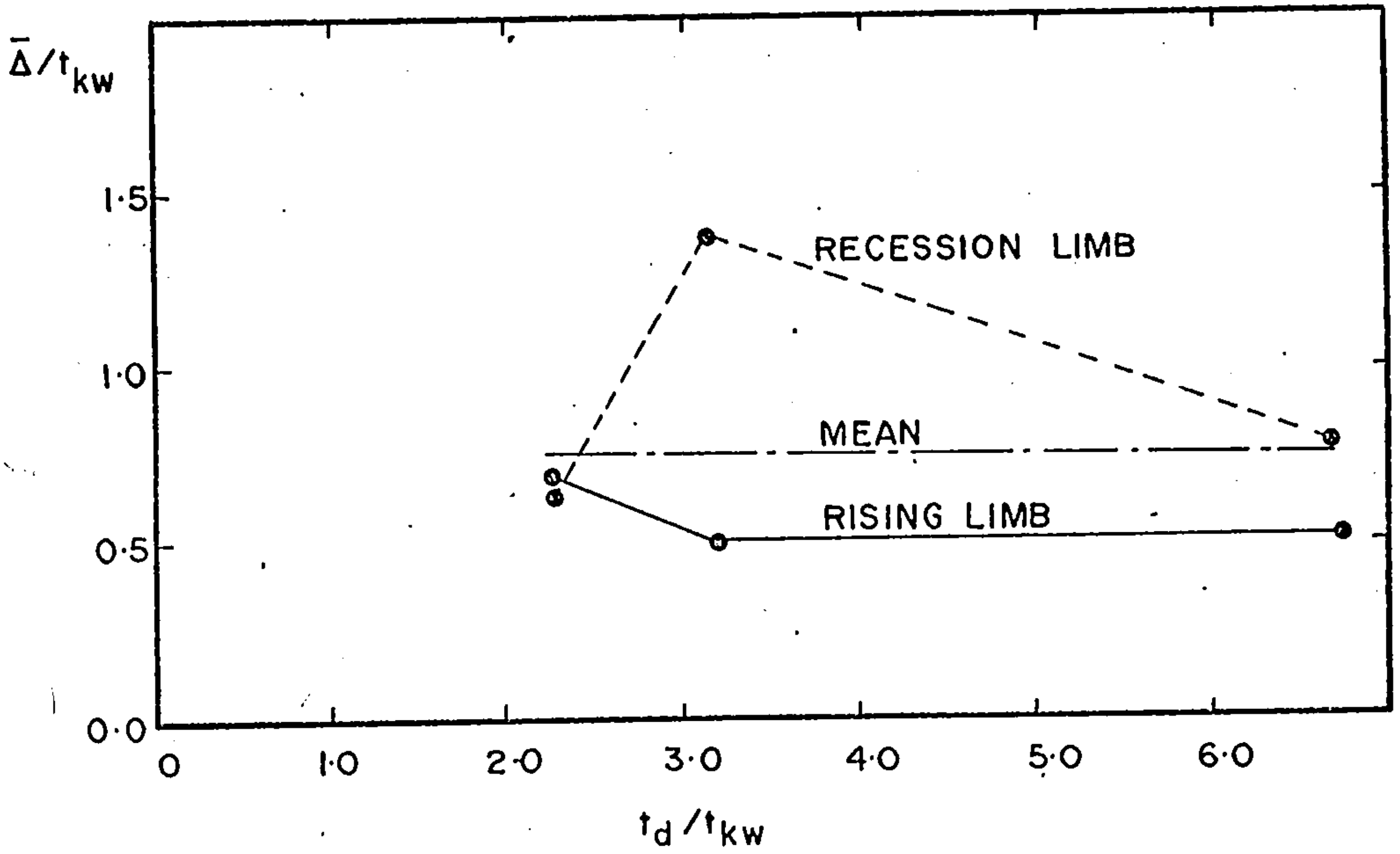

Fig. 5.8 Average Dimensionless Lag Time ($\frac{\bar{\Delta}}{t_{kw}}$) vs Dimensionless Storm Duration (t_d/t_{kw}) for Supercritical Slope (S_o = 0.0061)

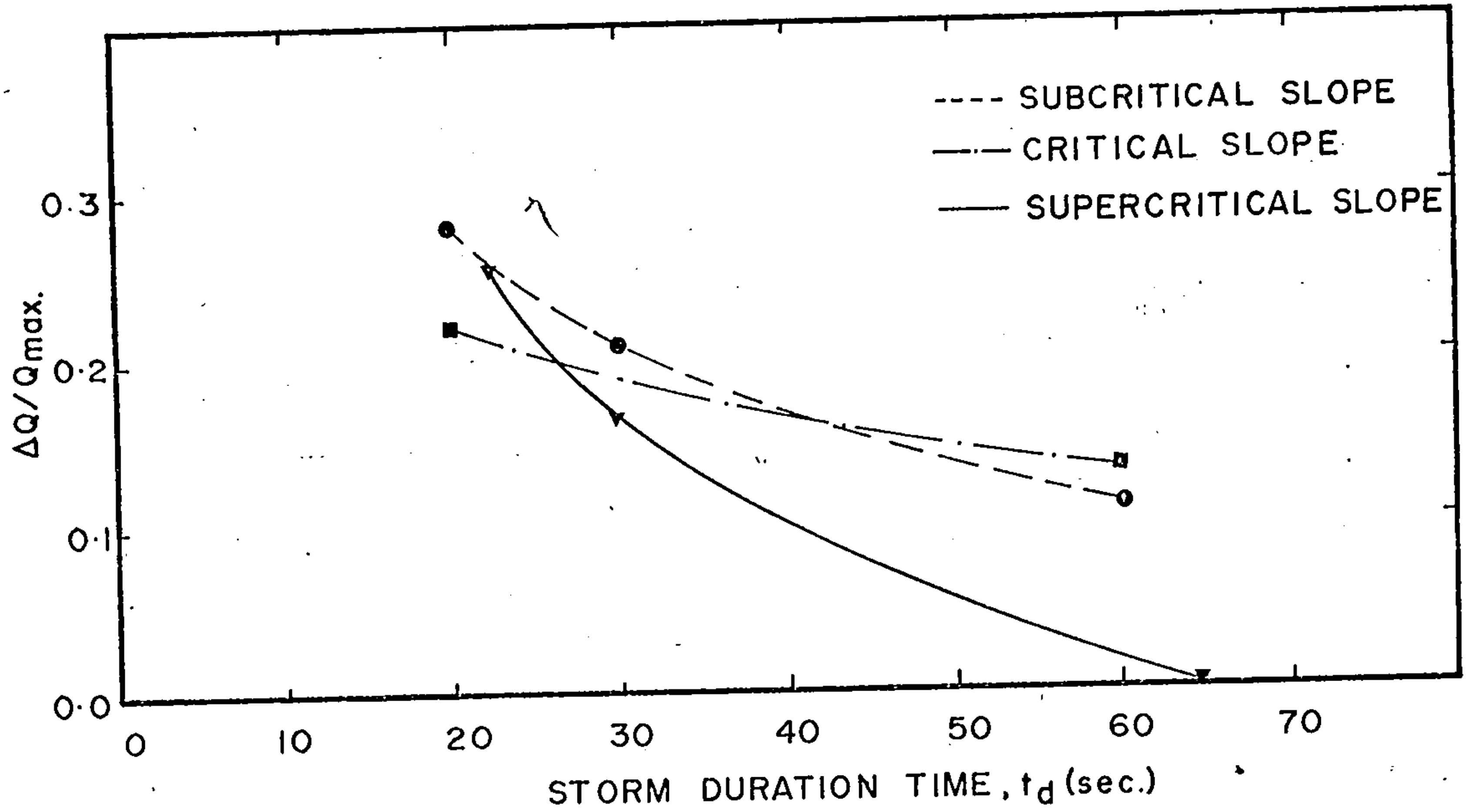

Fig. 5.9 Effect of Storm Duration (t_d) on ($\frac{\Delta Q}{Q_{max}}$) for Different Slopes

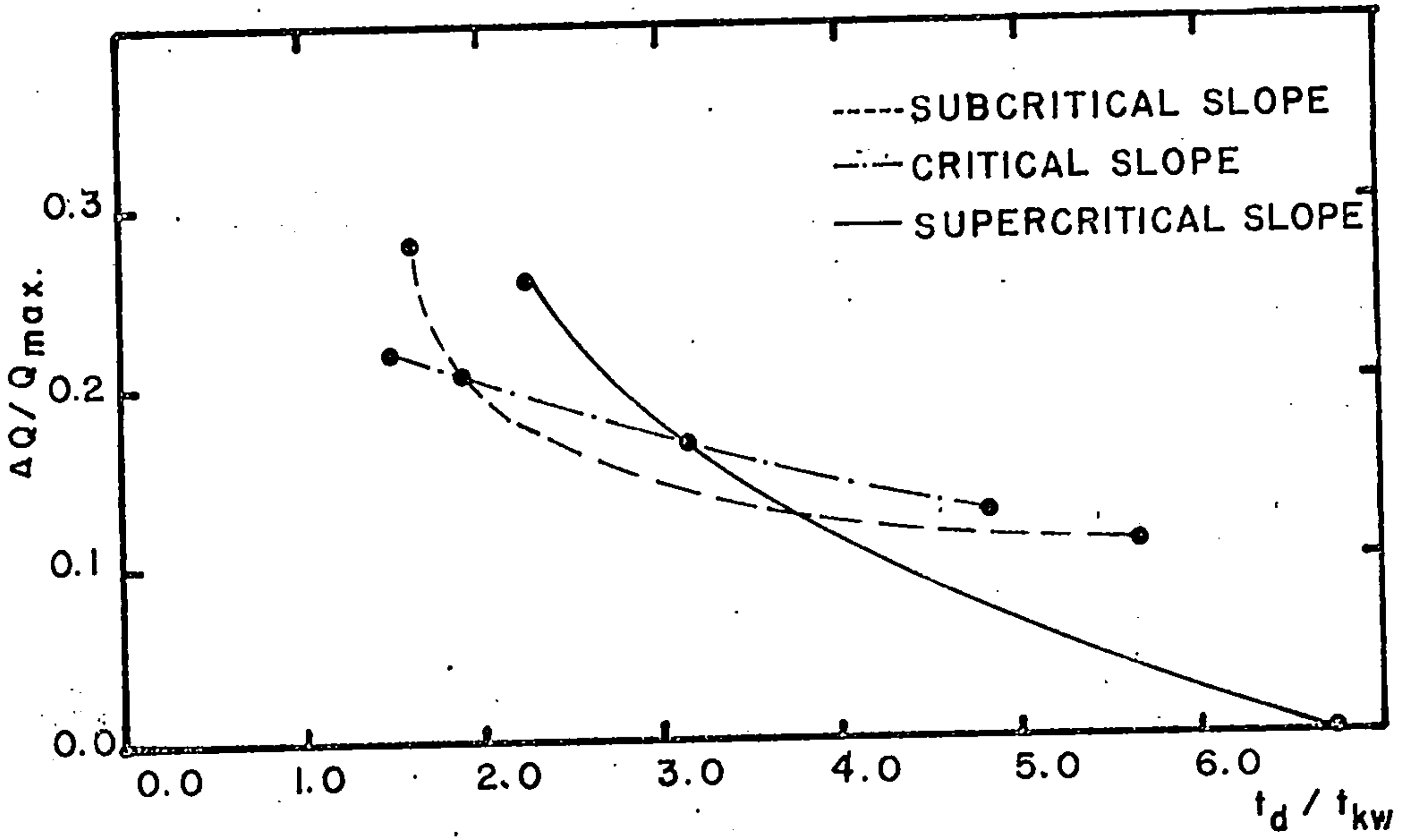

Fig. 5.10 Effect of Dimensionless Storm Duration $(\frac{t_d}{t_{kw}})$ on $(\frac{\Delta Q}{Q_{max}})$ for Different Slopes

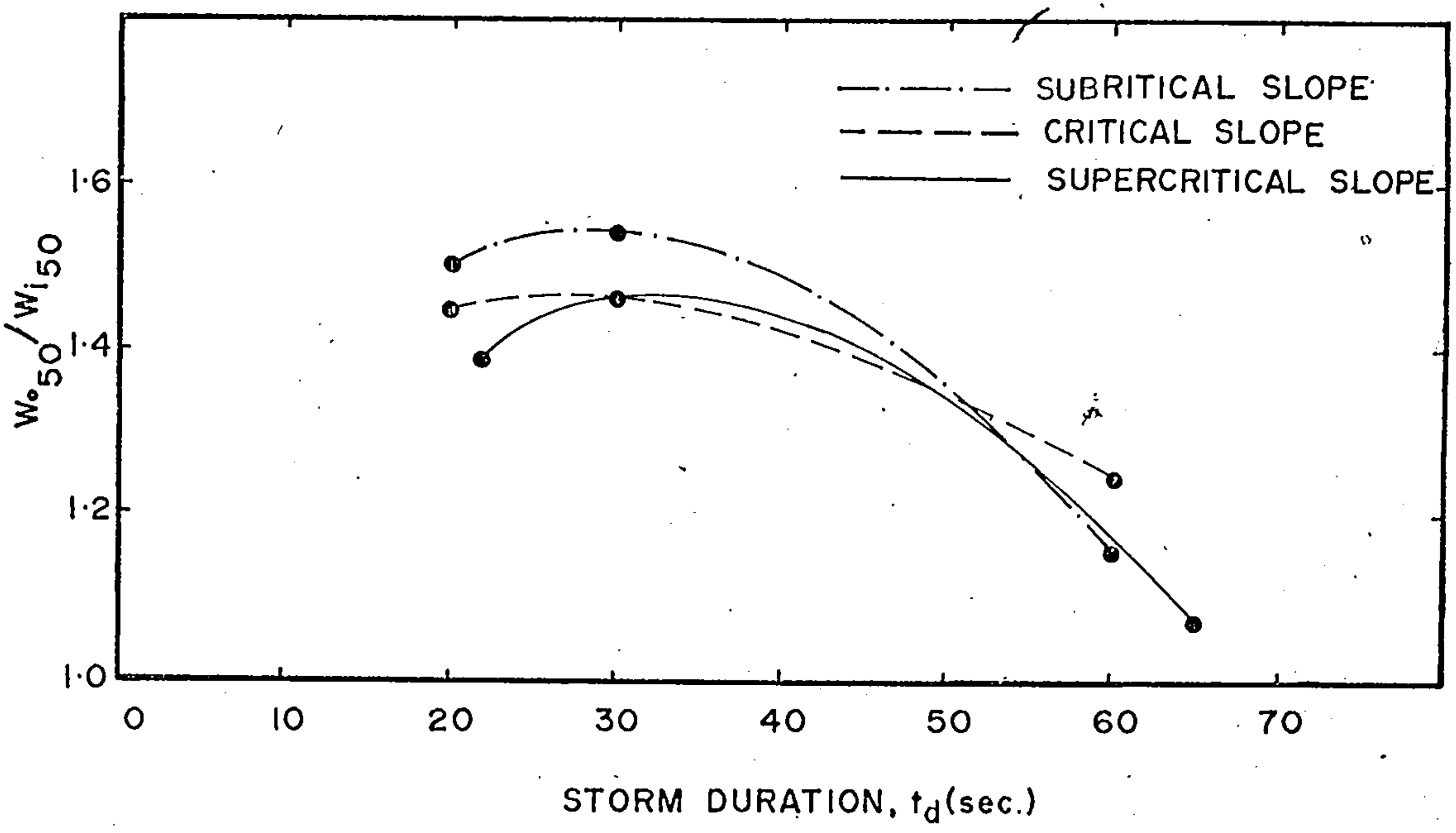

Fig. 5.11 Effect of Storm Duration (t_d) on Dimensionless Hydrograph Width ($W_{o_{50}}/W_{i_{50}}$) for Different Slopes

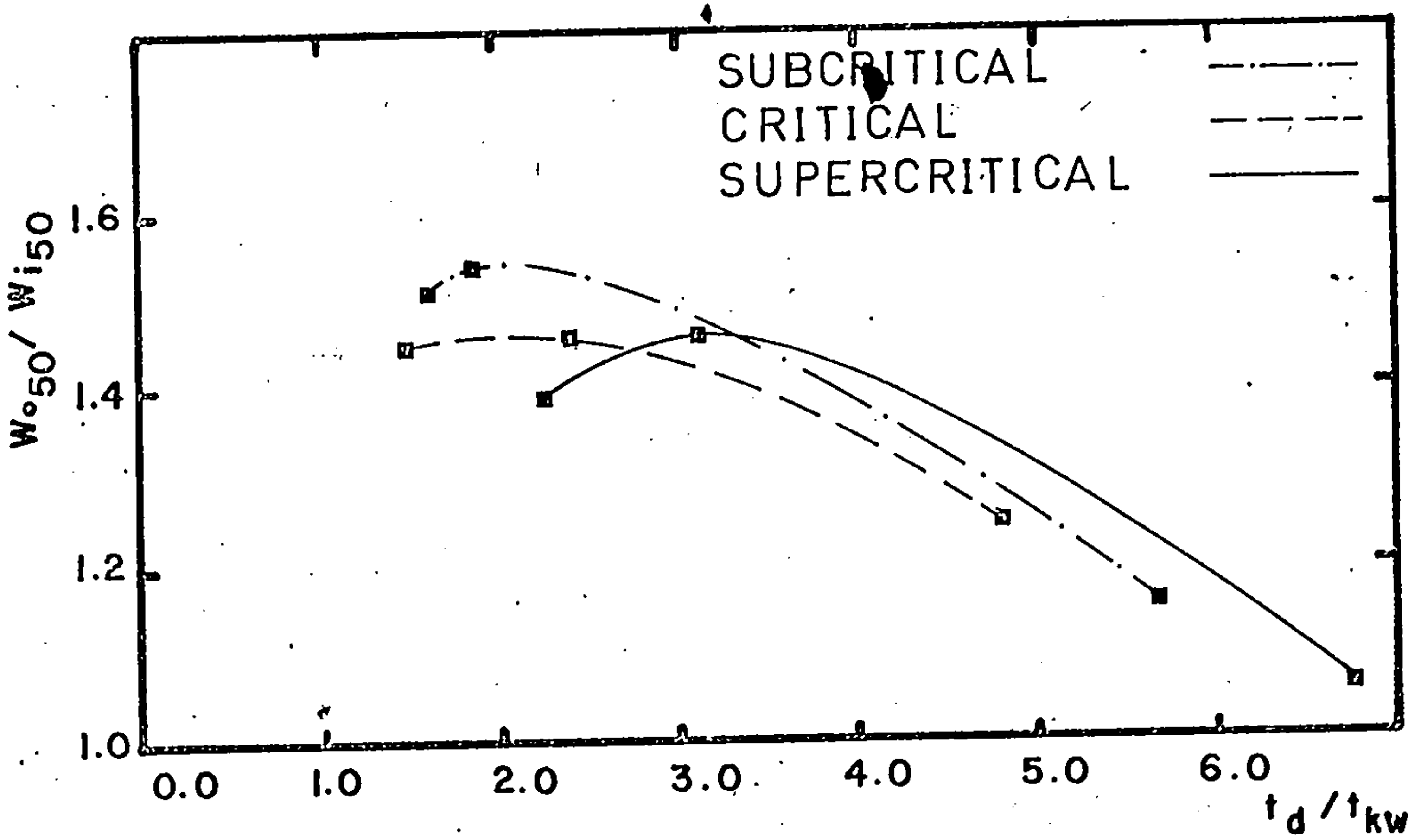

Fig. 5.12 Effect of Dimensionless Storm Duration $(\frac{t_d}{t_{kw}})$ on Dimensionless Hydrograph Width $(W_{o_{50}}/W_{i_{50}})$ for Different Slopes

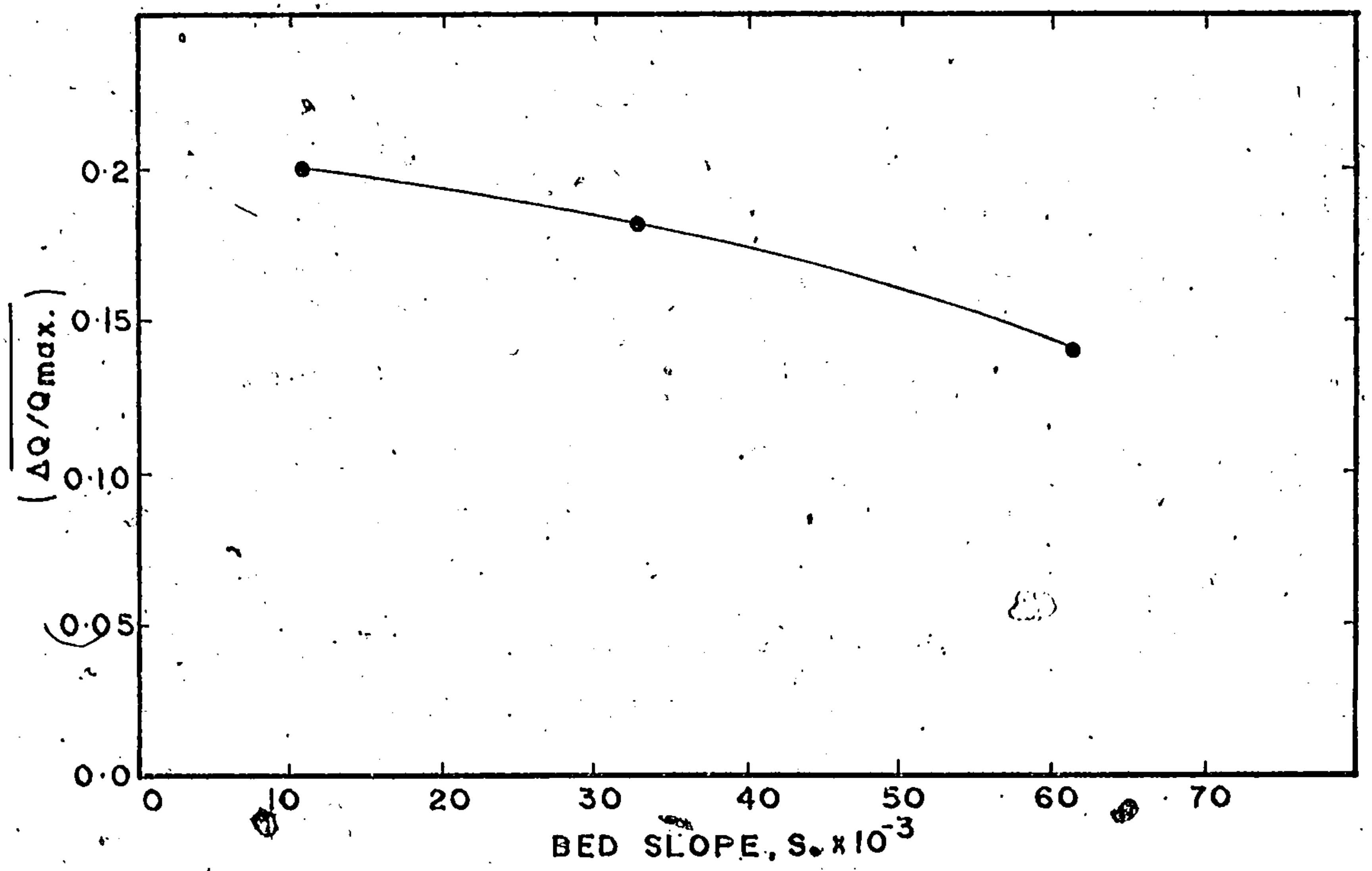

Fig. 5.13 Effect of Bed Slope (S_o) on the Average Difference Between the Inlet and Outlet Hydrograph Peaks

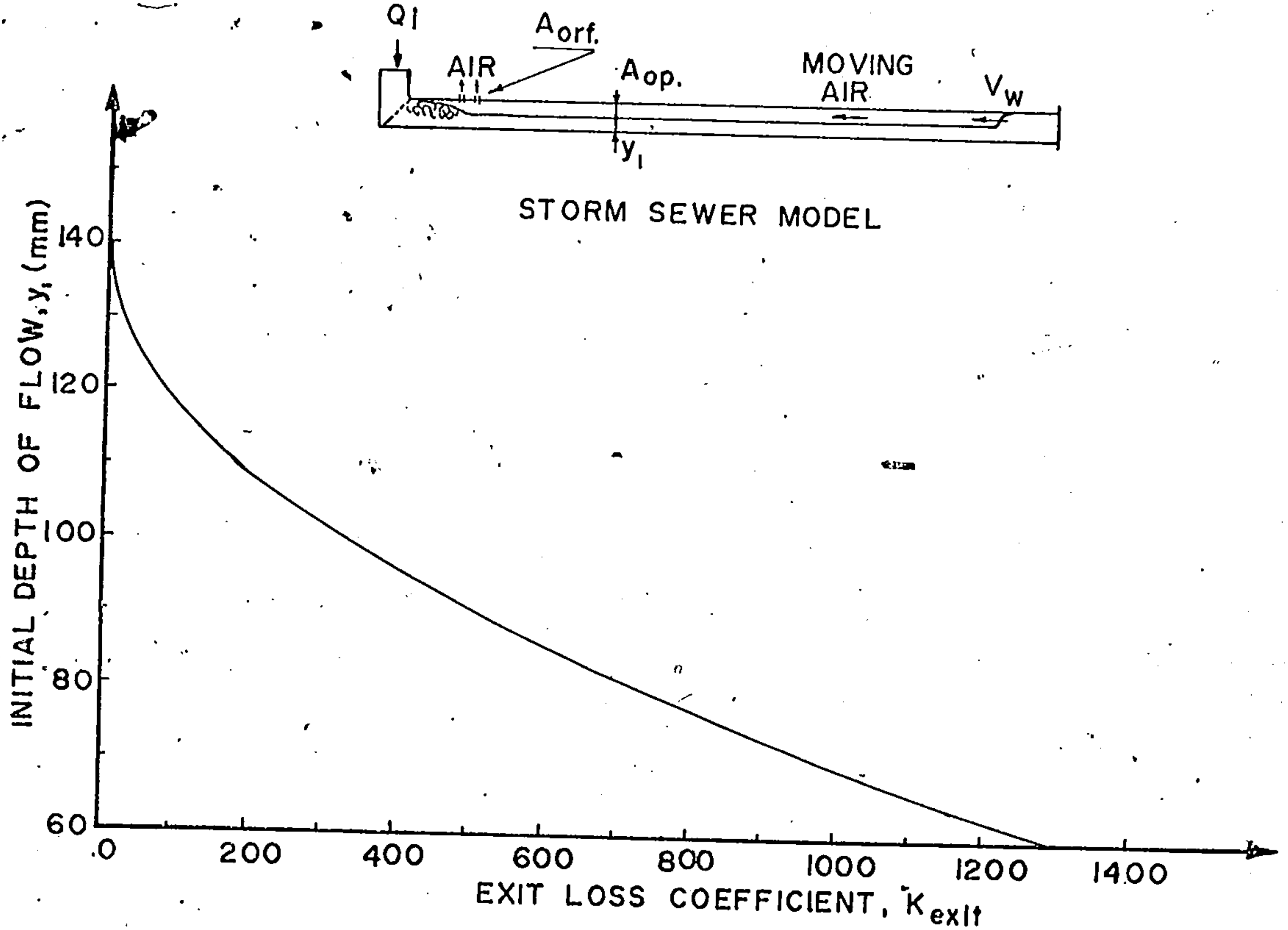

Fig. 5.14 Effect of Initial Depth of Flow (y_1) on the Exit Loss Coefficient (K_{exit})

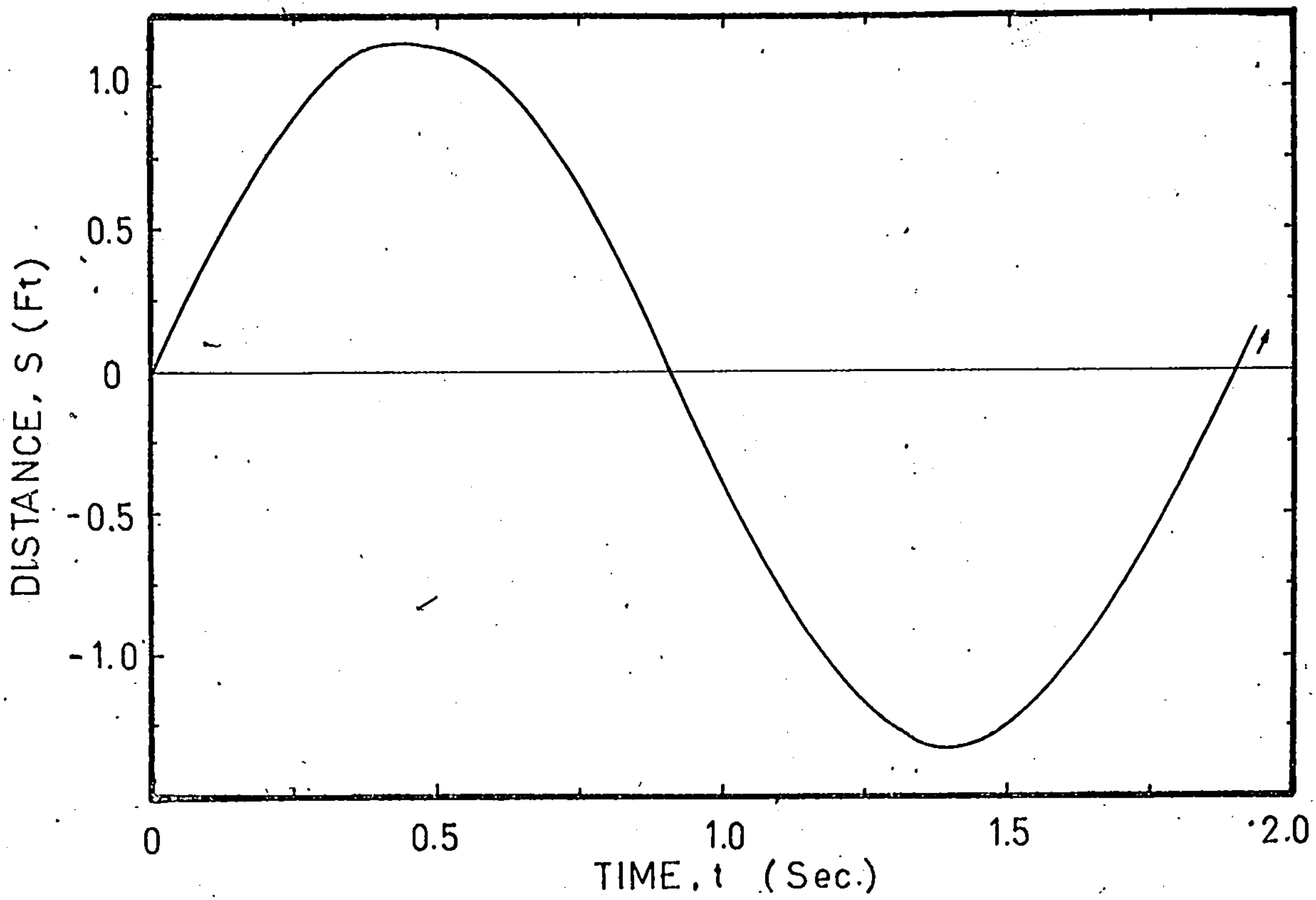

Fig. 5.15 Typical (S-t) Curve for a Bubble According to Equation 3.31 ($S_o = 0$, $\ell_{b_1} = 36'$, $\ell' = 40'$, $(y_1/H) = 0.93$, and $h_2 = 0.29'$)

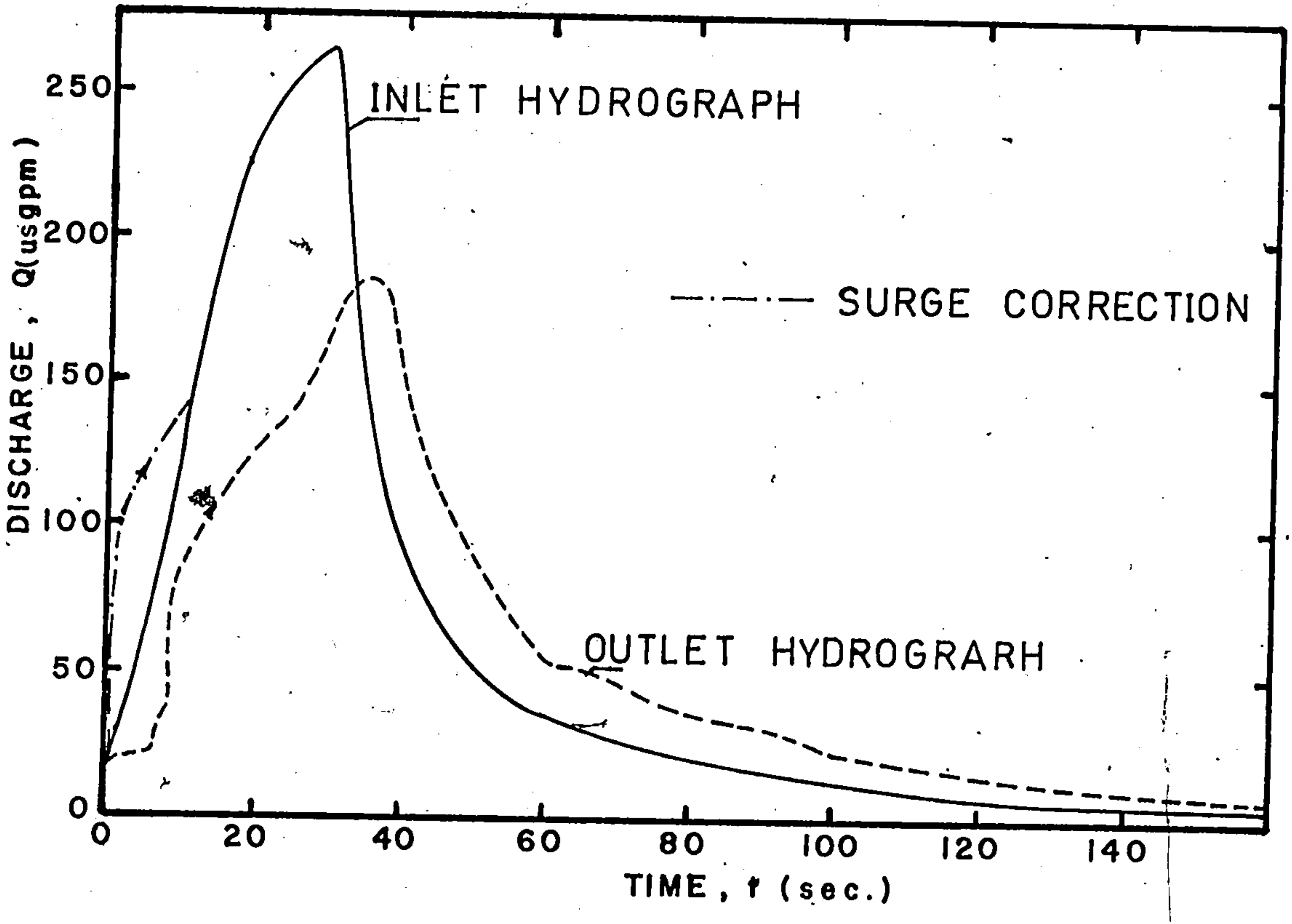

Fig. 5.16 A Possible Correction for the Inlet Hydrograph Due to Surge in Large Compartment of the Overhead Tank

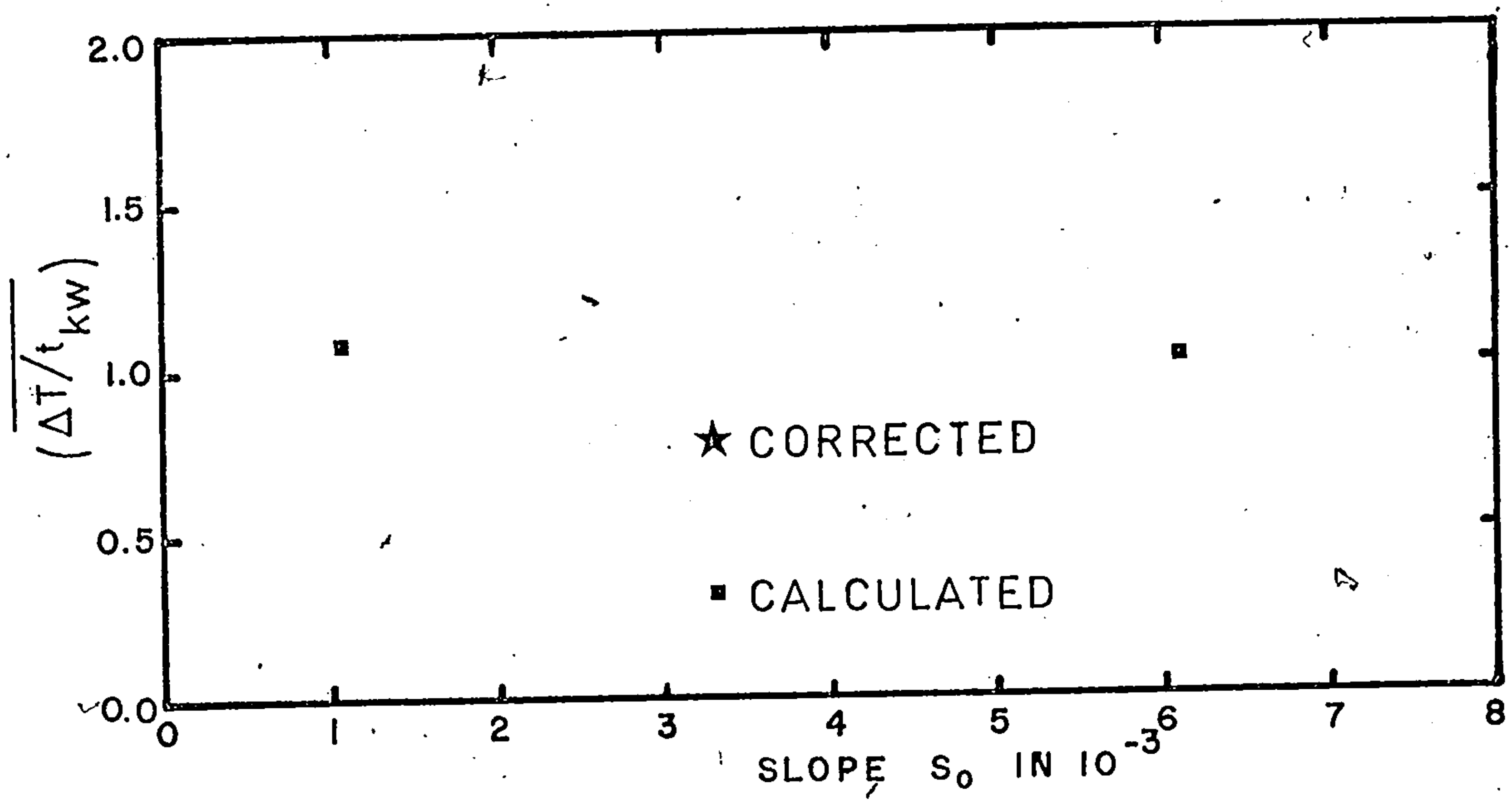

Fig. 5.17 Effect of Bed Slope (S_o) on the Average Dimensionless Lag Time ($\overline{\Delta T/t_{KW}}$) Measured Between the Hydrograph Centroids

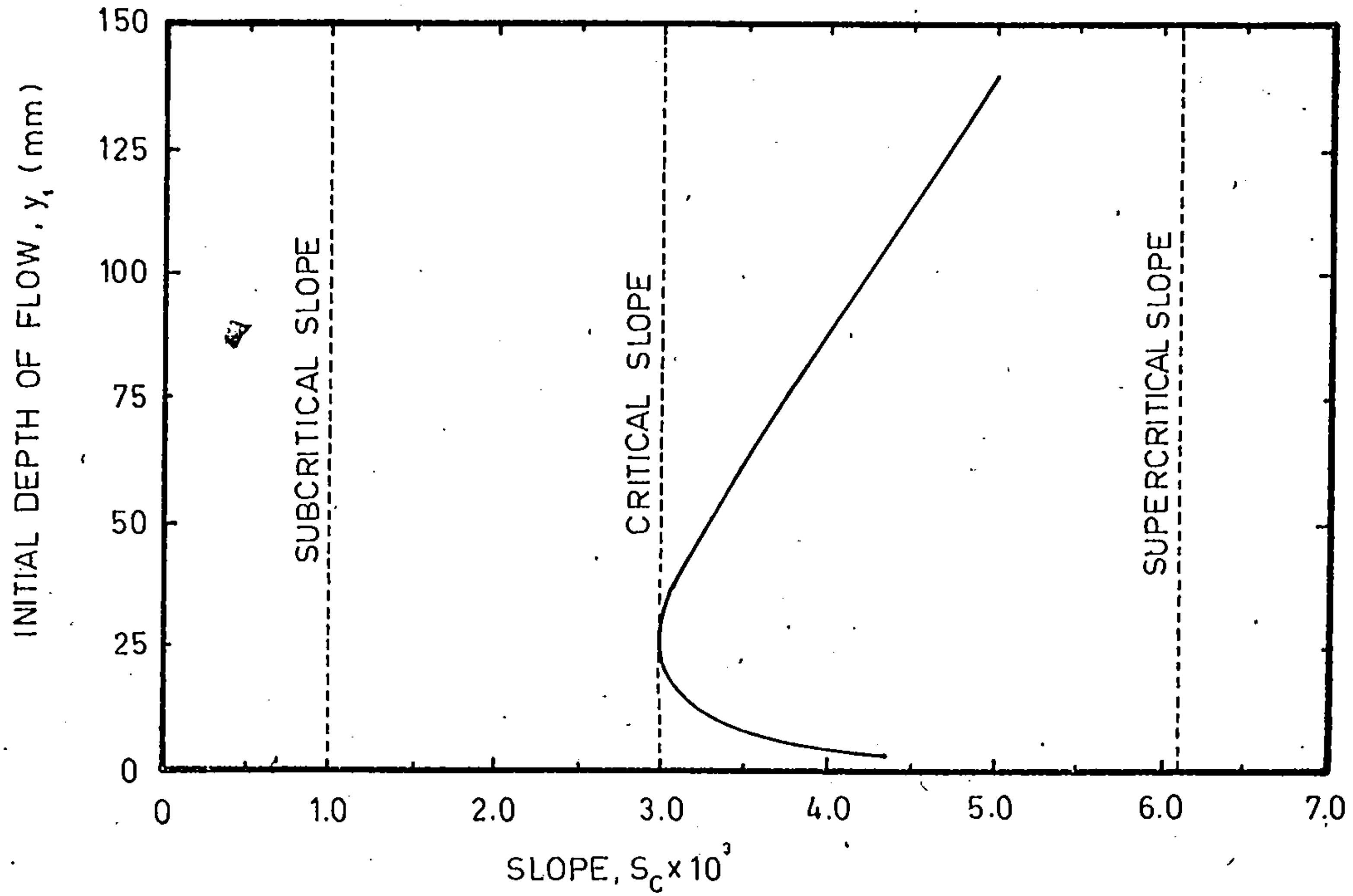

Fig. A.1 The Limit Slope of the Pipe

PHOTOGRAPHS

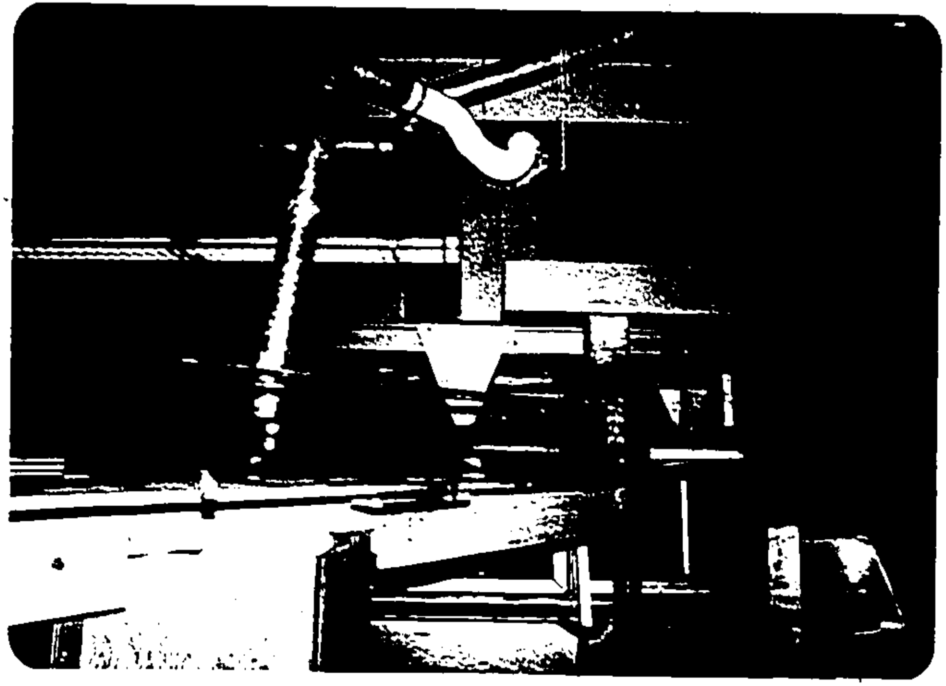

Photo 4.1 Upstream End of the Storm Sewer Model with the Overhead Tank

Photo 4.2

Flow Measurement at the Downstream End of the Pipe

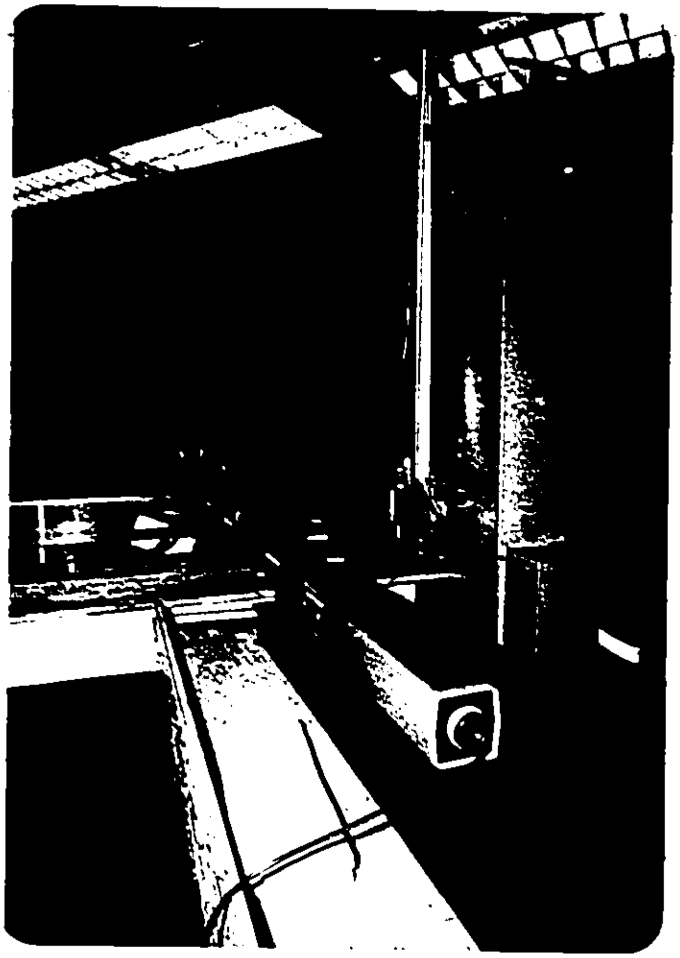

Photo 4.3

Downstream Piezometer Tube and Laser Anemometer Optics

Photo 4.4

Storm Sewer Model Looking Upstream

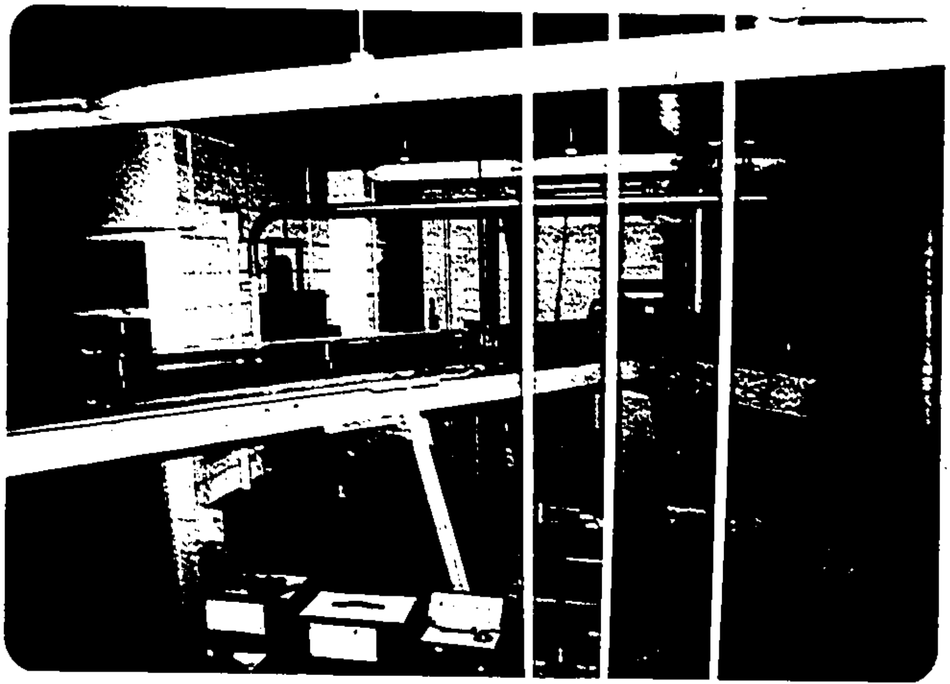

Photo 4.5 Downstream End of the Storm Sewer Model with the Centrifugal Pump

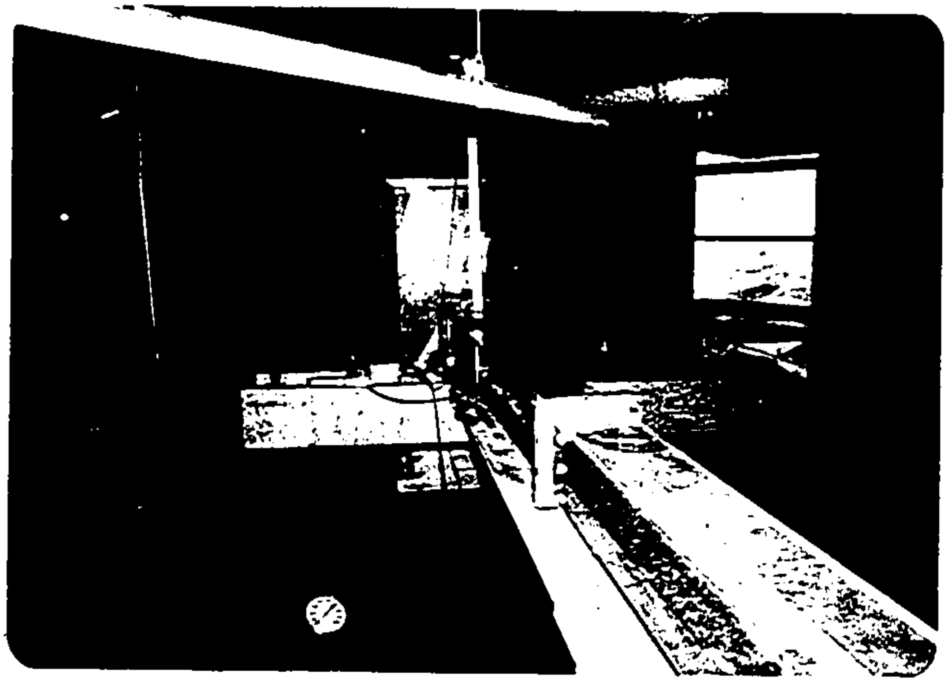

Photo 4.6 Downstream End of the Model with the End Tank

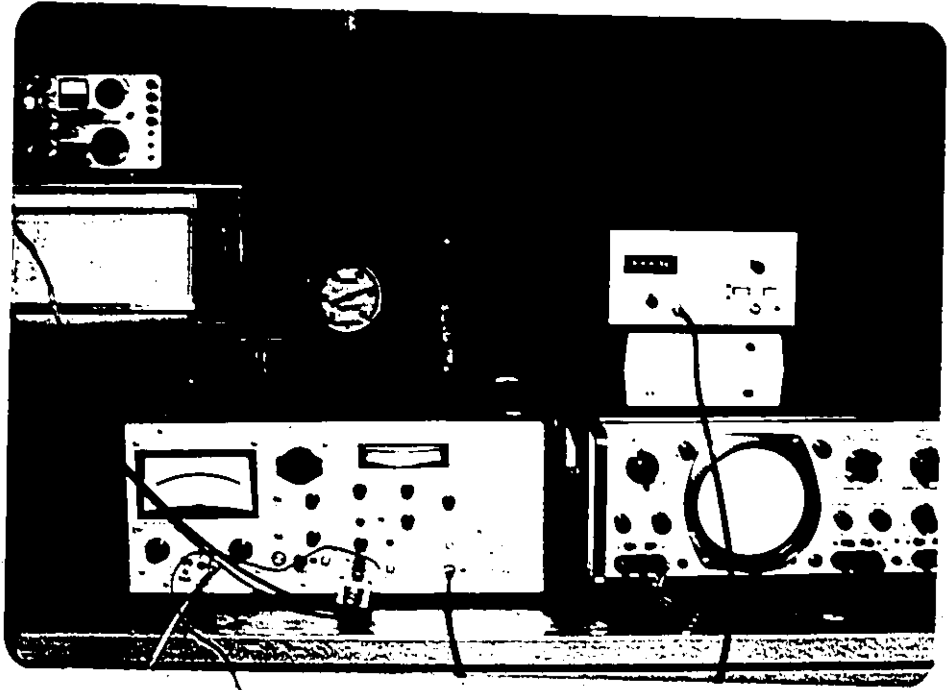

Photo 4.7 Set Up for the Outlet Hydrograph Measurement

Photo 4.8 Test Section for Flow Velocity Measurement Using Laser Anemometer

REFERENCES

1. Baker, O. Oil Gas J., Vol. 53, no. 12, pp. 185-190, 192, 195, July 26, 1954.

2. Blatzer, R.A., and Lai, C. Computer Simulation of Unsteady Flows in Waterways, J. of Hydraulics Division, ASCE, Vol. 94, No. HY4, Proc. Paper 6048, July, 1968, pp. 1081-1117.

3. Chow, V.T. Open-Channel Hydraulics, McGraw-Hill Book Co., New York, 1959.

4. Dorsch Consult. Urban Hydrological Processes Computer Simulation, Munich-Toronto, 1972.

5. Harris, G.S. Real Time Routing of Flood Hydrographs in Storm Sewers, J. of Hydraulics Division, ASCE, Vol. 96, No. HY6, Proc. Paper 7327, June, 1970, pp. 1247-1260.

6. Henderson, F.M. Open Channel Flow, MacMillan, New York, 1966.

7. Isaacson, E., Stoker, J.J., and Troesch, A. Numerical Solution of Flood Prediction and River Regulations Problems, Report III, IMM-MY235, New York University, October, 1956.

8. Metcalf and Eddy, Inc. Wastewater Engineering: Collection, Treatment, and Disposal, New York, McGraw-Hill Book Co., 1972.

9. Morgali, J.R. Hydraulic Behavior of Small Drainage Basins, Stanford University, Technical Report No. 30, October, 1963.

10. Mozayeny, B., and Song, C.S. Propagation of Flood Waves in Open Channels, J. of Hydraulics Division, ASCE, Vol. 95, No. HY3, Proc. Paper 6561, May, 1969, pp. 877-892.

11. Streeter, V.L. and Wylie, E.B. Fluid Mechanics, New York, McGraw-Hill Book Co., 1958.

12. Streeter, V.L. and Wylie, E.B. Hydraulic Transients, New York, McGraw-Hill Book Co., 1967.

13. Strelkoff, T. Numerical Solution of Saint-Venant Equations, J. of Hydraulics Division, ASCE, Vol. 96, No. HY1, Proc. Paper 7043, January, 1970, pp. 223-252.

14. Terzidis, G., and Strelkoff, T. Computation of Open-Channel Surges and Shocks, J. of Hydraulics Division, ASCE, Vol. 96, No. HY12, Proc. Paper 7780, December, 1970, pp. 2581-2610.

15. Thomas, H.A. The Hydraulics of Flood Movements in Rivers, Carnegie Institute of Technology, Engineering Bulletin, 1934.

16. Wallis, G.B. One-dimensional Two-phase Flow, McGraw-Hill Book Co., New York, 1969.

NOMENCLATURE

A	Area of flow; area
A_b	Contact area between the bubble and the water
A_{orf}	Area of air vents
a	Velocity of pressure wave
B	Pipe width; a constant
C	Chezy coefficient
C_{cs}, C_{cs}	Wave velocities in homogeneous and stratified flow
c	Velocity of dynamic wave relative to weighted average velocity, celerity
D	Constant; hydraulic depth
d	Pipe diameter
E	Modulus of elasticity
e	Pipe wall thickness
F	Hydrostatic force
F_r	Froud number
f	Force per unit volume of flow
f	Friction factor
g	Acceleration due to gravity
H	Height of conduit
h	Surge height; height of bubble
h_f	Pressure drop due to friction

I	Inflow
i	Infiltration rate
K	Hydraulic conductivity
K	Bulk modulus of water; bulk modulus of mixture
K_{exit}	Exit coefficient
K_g	Bulk modulus of gas
K_{liq}	Bulk modulus of liquid
i, j, k	Indices
L	Length of pipe
ℓ'	Distance of the bubble from the upstream end of the pipe
N	Number of readings
n	Manning's roughness coefficient
O	Outflow
P	Air pressure
P	Intensity of air pressure
P_{at}	Atmospheric pressure
P_i	Air pressure inside the pipe
P_o	Initial absolute air pressure inside the bubble when the bubble formed
Q	Discharge
Q_n	Normal discharge
Q_o	Steady discharge
q	Discharge per unit width of the channel
Q_i	Initial discharge

R	Hydraulic radius
R_e	Reynolds' number
r	Rainfall intensity
S	Distance travelled by bubble
S_f	Friction slope
S_o	Bottom slope
T	Top width of flow
t	Time
t_d	Storm duration
t_{kw}	Time required for the kinematic wave to reach the test section
U	Wave velocity
u	Velocity component
V	Velocity of flow
V_{kw}	Velocity of kinematic wave
V_o	Weighted average velocity
V_w	Surge velocity
$\forall$	Total volume of liquid
$\forall_g$	Volume of gas
$\forall_{liq}$	Volume of liquid
$\forall_i$	Volume of bubble during the compression
$\forall_o$	Volume of trapped air inside the bubble when the bubble formed
v	Velocity of component

$W_{i_{50}}$	Inlet hydrograph width at 50% of the maximum discharge
$W_{o_{50}}$	Outlet hydrograph width at 50% of the maximum discharge
$\overline{X}$	Time centroid
x	Distance along the pipe
x	As a subscript denotes partial differentiation
$\overline{x}$	Time centroid of strips
y	Depth of flow
y_1	Initial depth of flow
$\overline{y}$	Distance between the pressure center and the water surface
Z	Downstream piezometric head relative to sewer crown
Z	Section factor
α	Void fraction; coriolis coefficient
γ	Unit weight of fluid
Δ	Small change
$\overline{\Delta}$	Average lag time
ΔT	Lag time between the centroids of the inlet and outlet hydrographs
ε	Average difference between theoretical curve and experimental mean curve
ζ	Slope of characteristics curves
θ	Dimensionless parameter

μ	Viscosity
ν	Kinematic viscosity
π	Natural constant
ρ	Density
σ	Standard deviation of the experimental results from the experimental mean curve

VITA AUCTORIS

1949 Born on the 17th of March in Alexandria, Egypt.

1967 Matriculated from Ramleh High School, Alexandria, Egypt.

1972 Graduated with a Bachelor of Science (Honour) in Civil Engineering, Alexandria University, Alexandria, Egypt.

1972 Appointed as an instructor of Civil Engineering at Alexandria University, Alexandria, Egypt.

1975 Registered as a M.A.Sc. candidate in Civil Engineering at the University of Windsor, Windsor, Ontario, Canada.